On the Quantitative Analysis
of Ultrasound Signals
with Applications to Diffuse Liver Disease

Bernard Oosterveld

On the Quantitative Analysis
of Ultrasound Signals
with Applications to Diffuse Liver Disease

Bernard Oosterveld

Over Kwantitatieve Analyse
van Ultrageluidssignalen
met Toepassing op Diffuse Leverziekten

een wetenschappelijke proeve op het gebied van
de geneeskunde en tandheelkunde,
in het bijzonder de geneeskunde

Proefschrift

ter verkrijging van de graad van doctor
aan de Katholieke Universiteit te Nijmegen,
volgens besluit van het college van decanen
in het openbaar te verdedigen op

dinsdag 1 mei 1990
des namiddags te 3.30 uur

door

Bernardus Jacobus Oosterveld

geboren op 9 augustus 1955 te Arnhem

Voorwoord

Op deze plaats wil ik al diegenen bedanken die op enigerlei wijze hebben bijgedragen aan het onderzoek, waarvan dit proefschrift het resultaat is. In het bijzonder wil ik dank zeggen aan:

Prof. EGJ Eijkman voor de moeite, die u, als lid van de STW-gebruikerskommissie en als begeleider van het promotieonderzoek, heeft genomen om u in dit onderzoek te verdiepen.

Prof. GJE Rosenbusch voor uw meedenken en meesturen bij de planning van de klinische studies.

Han Thijssen voor je niet aflatende enthousiasme, je optimisme, en het scheppen van een prettige werkkring.

Leo Romijn, mijn vakbroeder, voor jouw inbreng in de totstandkoming van dit resultaat en de prettige manier waarop we hieraan hebben samengewerkt.

Peter Hartman, voor je voortvarendheid bij het werven van proefpersonen en het selecteren van patienten.

Wim Kruimer, voor het realiseren van de mogelijkheid van het klinisch deel van het onderzoek.

Hans Verhoeven, voor het optimaliseren hiervan.

Rien Cuypers voor je alom ondersteunende aanwezigheid.

Marius Cloostermans en Wim Verhoeven, voor het leggen van een stevige basis (in software en kennis) waarop het goed bouwen was.

Norbert Vasen, Ronald Fabel en Eric Jacobs, voor jullie inbreng in het onderzoek tijdens jullie afstudeerstage en jullie geduld met jullie begeleider.

Bob Wagner (Center for Devices and Radiological Health, Food and Drug Administration), for your inspiring contribution to chapter VI of this thesis.

Michael Insana (University of Kansas), for the discussions we had and your helpful comments to the work of which chapter VII is the result.

Ivan Zuna (DKFZ), fuer deine Anweisungen wie man SAS verwenden kann bei der multivariater statistischer Analyse.

Denise, Christianne en Marijke van de echokamers van de afdeling Radiodiagnostiek, voor jullie geduld met onze apparatuur, waarmee jullie opnamen hebben gemaakt van patienten en proefpersonen.

Contents

I

Introduction

Since the introduction of ultrasound as a means to extract in a noninvasive way information from within the human body, echography has achieved a firm position among the other medical imaging techniques. Especially the real-time technique which enables the display of movement by the tissues (e.g. the heart) has made echography an indispensable diagnostic tool.

Because the nature of the ultrasound radiation is completely different from the other kinds of radiation used in medical imaging, such as e.g. X-ray, the information obtained about the tissues is also of a completely different nature. Ultrasound images display local differences in the acoustical (i.e., mechanical) properties of the tissue, whereas e.g. X-ray images essentially display the absorption of the radiation by the tissue. Therefore, the information obtained from echographic examinations often is complementary to information obtained with other imaging techniques.

An important advantage of ultrasound over the radiation used for the other imaging techniques is that it does not cause any damage to the interrogated tissues if employed at the low intensities that are customary for diagnostic echographic equipment. The reason for this is that ultrasound is a non-ionizing kind of radiation. This property makes echography the ideal diagnostic imaging modality for screening, follow-up examinations, e.g. for the monitoring of treatment, as well as for obstetrical diagnosis.

Apart from the ability of displaying anatomical structures such as the outline of organs and bloodvessels, echographic images also display the soft tissue that constitutes these structures. This property has raised a continuing interest in the exploration of the possibilities of quantitative analysis of images of such tissues. The field of scientific investigations on this topic and, more generally, the study of the interaction of ultrasound with biological tissue is called "Ultrasonic Tissue Characterization". It's goal is to extract information from the echo signals, which is additional to the information depicted in the ultrasound image, in order to find correlations of the quantified parameters with the condition of the tissues.

1 The Sound Field

The most frequently used technique for ultrasonic imaging is the pulse-echo method. A transducer transmits a sound pulse into a medium and then receives the echoes originating at acoustic inhomogeneities in the medium. The transducer is systematically translated in lateral direction (i.e., perpendicular to the soundbeam) and again a pulse is transmitted. The echoes that are received then stem from a part of the medium, that

is increasingly different the more the beam is translated. In the echographic system the so-called "radiofrequency" echo signals are amplified depth dependently to compensate for the attenuation in the medium, after which the envelope is detected. Displaying the envelope signals corresponding to consecutive transducer positions produces a two-dimensional acoustical image of the medium, called the B-mode image.

The transducer consists of a piezo-electric material which is excited in a thickness-mode vibration by an electric impulse, thus generating a sound pulse of short duration. The reverse occurs at reception: if the sound pressure of an echo deforms the piezo-electric material it generates an electric signal. The acoustic transmission pulse has to be of a short duration, or equivalently, the spectrum of the pulse has to be broadband, to obtain a reasonable resolution. The acoustic pulse consists of a high frequency carrier with an envelope which can often be approximated by a Gaussian:

$$p(t) = \frac{1}{\sqrt{2\pi\sigma_t^2}} e^{-(t-t_0)^2/2\sigma_t^2} \cos 2\pi f_c t \tag{1}$$

where σ_t = the standard deviation of the envelope,
$\quad$ t = time
$\quad$ f_c = the central (or carrier) frequency.

The corresponding amplitude spectrum then also has a Gaussian shape

$$P(f) = \frac{1}{\sqrt{2\pi\sigma_f^2}} e^{-(f-f_c)^2/2\sigma_f^2} \tag{2}$$

where σ_f = the standard deviation of the spectrum $(\sigma_f\sigma_t = 1/2\pi)$
$\quad$ f = frequency.

Central frequencies of 2 up to 15 MHz are used in diagnostic ultrasound. Each pulse propagates through the medium following a specific beam pattern, or sound field, the characteristics of which are determined by the waveform of the pulse and the physical dimensions of the transducer. Medical transducers are usually focussed to improve the resolution in the lateral direction. In this study only one kind of transducer was considered, namely the circular single element transducer having a spherically curved surface to focus the sound beam. Figure 1 shows the beam patterns of such a transducer used in continuous wave (CW) and in pulsed transmission modes. The positions of the interference maxima and minima in the CW mode depend on the frequency. In the pulsed mode the CW beam patterns corresponding to the frequencies present in the spectrum of the pulse are superimposed, whereby the interference maxima and minima are smoothed. The beam patterns of figure 1 were numerically calculated using the computer simulation program by Verhoef [1].

2 Interaction of Ultrasound with Tissue

When biological tissue is insonated, echoes are caused by interfaces between parts of the tissue with different acoustical properties. If these interfaces are large compared to the wavelength of the ultrasound specular reflection and refraction, obeying Snell's laws, will occur. Such large interfaces are formed, for example, by the organ boundaries
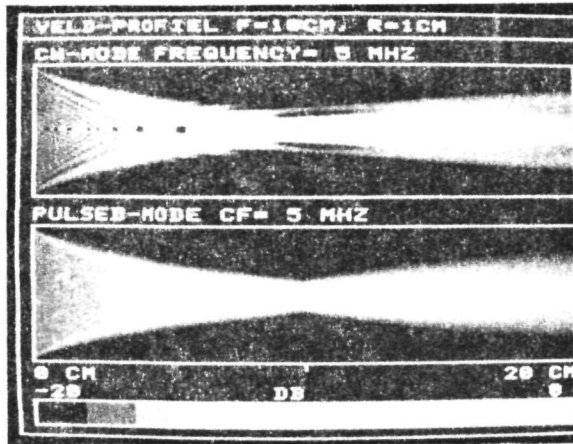
Figure 1: *a) The sound field of a circular single-element focussed transducer used in CW mode. b) The sound field of the same transducer in pulsed mode.*

and the larger bloodvessel walls. The echoes from these boundaries are usually strong because the differences in acoustical properties are large, and because the interface acts as a mirror reflecting a large fraction of the acoustic energy back to the transducer (if incidence was at a right angle). Reflection and refraction are (almost) frequency independent mechanisms.

If the size of the insonated structures is smaller than the wavelength, scattering will occur. Such small acoustical inhomogeneities are, for example, formed by the microvasculature and the collagen meshwork within the organs. At high frequencies also scattering at a cellular level may be present. The echoes caused by scattering are usually relatively weak because the local differences in acoustical properties forming the inhomogeneities are small. Furthermore, scattering is omnidirectional, so only a small portion of the energy is backscattered and received by the transducer. The frequency dependence of the scattering intensity can be modelled by a f^n behaviour, where the power n may vary from 0, for scatterers with sizes of the order of a wavelength, to 4, for scatterers much smaller than the wavelength.

If ultrasound propagates through a medium the pressure amplitude decreases with increasing penetration depth. This attenuation is caused by absorption, scattering, reflection, refraction and diffraction. In a medium consisting of only small inhomogeneities reflection and refraction are absent and the scattering contributes only a few percent to the attenuation at frequencies of 5 MHz or less [2]. Absorption mechanisms that are known are viscosity, heat conduction and several kinds of relaxation mechanisms [3]. The decrease in amplitude is exponential with the distance z traveled through the medium: $E(z)(:) \exp[-\alpha(f)z]$. The attenuation coefficient $\alpha(f)$ is frequency dependent: at high frequencies the attenuation is stronger than at low frequencies. The model generally used for the frequency dependence of the attenuation coefficient in soft biological tissues is a linear relationship: $\alpha(f) = \beta f$, which is only adequate if the echo signals are relatively narrowband.
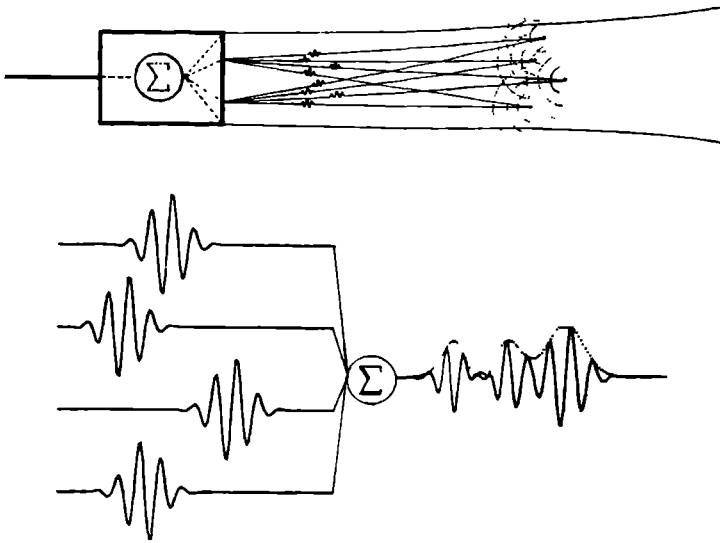
Figure 2: *a) Transducer insonating a tissue containing four point scatterers.*
b) Summation of the echoes at a single point of the transducer.

The velocity of sound propagation, the attenuation coefficient and the scattering parameters are examples of physical parameters which are dependent on the type of tissue. If the acoustical properties of a tissue change due to a disease then the value of these parameters may also change. Measurement of these parameters from the pulse-echo signals, caused by reflection and backscattering may therefore be useful. In addition, changes in the condition of the tissue may be revealed by the texture with which the tissue is displayed in the B-mode image. Application of texture analysis methods may therefore also yield useful parameters to detect or to differentiate diseased conditions.

3   The Echo Signal (Acoustic Speckle)

The physical phenomena underlying the interactions of ultrasound with tissue, can be described by modelling the tissue as a homogeneous medium, with or without attenuation, and with a constant sound velocity. The scattering inhomogeneities are modelled as randomly distributed discrete scatterers, which according to Huygens' principle act as secondary sources, producing spherical wavefronts. Examples of organs that are well described by this model are the liver, the spleen, and the thyroid.

The generation of echo signals is further explained using figure 2. This figure shows how a transducer transmits a pulse and four point scatterers are irradiated. The pulse reaches the scatterers at different times depending on the distance traveled from the transducer. The scatterers, acting as secondary sources, produce spherical wavefronts. The echoes from the scatterers arrive at the transducer face where linear summation of the pressure waves occurs and, therefore, interference takes place at every point of

the surface (Fig. 2b). The transducer is a phase sensitive receiver, therefore the contributions of all points of the surface are summated to produce the resultant rf echo signal. If the differences in arrival times of the echoes are smaller than the duration of the pulse, it is not possible to distinguish the contributions of the individual scatterers. So the exact number and the relative positions of the scatterers cannot be extracted from the echosignal, nor from its amplitude demodulated form, the envelope. In reality many more scatterers than depicted in figure 2 will simultaneously contribute to the echo signal. The volume in which these scatterers are contained is called the isochronous volume. Now the pulse propagates through the tissue, so the position of the isochronous volume changes with time. As time passes, different collections of scatterers at increasing distances from the transducer contribute to the echo-signal. If the scatterers are randomly positioned, the echo signal will be stochastic. The texture with which tissues, consisting of a random collection of scatterers, are displayed in B-mode images has been shown to be analogous to laser speckle [4,5]. In general, speckle will always occur if monochromatic radiation is used and a phase sensitive receiver is employed. Although the transmitted pulses are of short duration the ultrasound radiation has still a relatively short bandwidth. The echographic texture is, therefore, often refered to as acoustic speckle. The first and second order statistical characterization of laser speckle [6] was successfully applied to acoustic speckle [4,5,7].

Since most homogeneous tissues are well described by the model mentioned above the echo signals from such tissues have a random character. Analysis of these tissues must, therefore, be performed using statistical methods. To obtain accurate and stable estimates of the parameters a region of the tissue of sufficient size is needed from which independent samples can be taken and averaged. Therefore, any analysis of the signals will only yield global measures describing the tissue. A decrease in the size of the region, for example to produce so-called parametric images of the tissue, will also decrease the accuracy with which the parameters can be estimated. If parametric images are to be produced a compromise has to be found between the resolution of the image and the accuracy of the estimated parameter.

Recently an extended model was proposed for the tissue that constitutes the liver. The liver cells are organized in lobules, cylinder-like structures which are closely packed. The collagen rich triangular cylinders between the lobules (portal triads, triads of Kiernan) constitute a, more or less regular, hexagonal structure from which a coherent backscattering may be obtained. Within the lobules the liver cells, cappilaries and interstitial spaces form a random collection of scatterers, from which a random backscattering is obtained. Also in muscles a regular structure is present formed by the collagenous sheaths that surround the muscle fibers. A method was proposed [8] to estimate quantitatively the ratio of the echo intensities caused by random and coherent backscattering and the average distance between the structured scatterers.

4 The Diffraction Effect

As the pulse propagates through the tissue, not only the position but also the size and shape of the isochronous volume changes with time. This is caused by the depth dependence of the sound field (cf. Fig. 1), due to the focussing and the edge diffraction due to the limited size of the aperture. For this reason the properties of the echo signal depend

strongly on the distance of the transducer to the scatterers. This depth dependence is called the "diffraction effect". In order to obtain reliable and reproducable estimates of the attenuation coefficient, the scattering properties and the texture parameters a correction has to be applied to reduce, or even remove, this depth dependence.

5   On This Thesis

In chapter II the texture of B-mode images of tissues consisting of randomly distributed discrete scatterers is investigated, using realistic computer simulations and tissue mimicking phantoms. The depth dependent influences of the diffraction and of the attenuation on the texture are quantified using first and second order statistical analysis methods. Also the influence of tissue itself on the texture was investigated. The conclusion is drawn that if the number density of the scatterers is large only the average amplitude is sensitive to the properties of the tissue. The histogram of the amplitudes can then be described by a Rayleigh probability density function, i.e., "fully-developed speckle" occurs. If the number of scatterers is relatively low (sub-Rayleigh) then also the second order texture parameters depend on the tissue.

In chapters III, IV and V an alternative way of processing the radiofrequency echo signals is explored. Conventionally only the envelope information of the echo signals is used for imaging and the phase information is discarded. Using the derivative of the instantaneous phase, the instantaneous frequency can be calculated, and this may be used to produce a new kind of images, which are called "FM images". Since the rf signals are not frequency modulated we prefer the term "Phase Derivative (PD) images". The phase derivative is unstable, therefore, some stabilization method must be employed. In chapter III PD images are produced using several stabilization techniques, yielding images which are typical for the technique used. The influence of the strength of the stabilization on the images is investigated and an optimal stabilization is choosen for each technique. In chapter IV computer simulated PD images are used to explore the diffraction effects on the PD texture. Also the question to which extent the tissue itself has influence on the PD texture is investigated. In chapter V a theoretical description of the statistical properties of the texture of PD images is given. The influence of stabilization and the further processing of the phase derivative to produce the PD images are taken into account.

Chapter VI is devoted to the detection of focal lesions. A systematic study is presented of several kinds of gray level coding of the echo amplitude. The influence of the coding on first and second order statistics and on lesion detectability is investigated by using simulated and measured echograms obtained from homogeneously scattering media and from a scattering phantom containing contrasting lesions.

Chapter VII is a report on a clinical study on tissue characterization. Rf data of the human liver were acquired *in vivo* by using a custom-designed data-acquisition system that is connected to a mechanical sector scanner. A method is proposed to compensate for the diffraction effects and for the influence of attenuation to obtain depth independent estimates of the parameters. Several methods to estimate the attenuation coefficient are compared. The potential of using the attenuation coefficient and parameters obtained by analyzing the texture of the corrected B-mode images to discriminate between normal and diffusely diseased tissues is explored.

References

[1] Verhoef, W.A., Cloostermans, M.J.T.M., and Thijssen, J.M., The impulse response of a focussed source with an arbitrary axisymmetric surface velocity distribution, *J. Acoust. Soc. Am. 75*, 1716-1721 (1984).

[2] Nicholas, D., Evaluation of backscattering coefficients for excised human tissues: results, interpretation and associated measurements, *Ultrasound in Med. and Biol. 8*, 17-28 (1982).

[3] Jongen, H.A.H., Thijssen, J.M., Van den Aarssen, M., and Verhoef, W.A., A general model for the absorption of ultrasound by biological tissues and experimental verification, *J. Acoust. Soc. Am. 79*, 535-540 (1986).

[4] Burckhardt, C.B., Speckle in ultrasound B-mode scans, *IEEE Trans. Son. Ultrason. SU-25*, 1-6 (1978).

[5] Abbott, J.G., and Thurstone, F.L., Acoustic speckle: theory and experimental analysis, *Ultrasonic Imaging 1*, 303-324 (1979).

[6] Goodman, J.W., Statistical Properties of Laser Speckle, in *Laser Speckle and Related Phenomena*, J.C. Dainty, ed., pp. 9-75 (Springer Verlag, Berlin, 1975).

[7] Wagner, R.F., Smith, S.W., Sandrik, J.M., and Lopez, H., Statistics of speckle in ultrasound B-scans, *IEEE Trans. Son. Ultrason. SU-30*, 156-163 (1983).

[8] Wagner, R.F., Insana, M.F., and Brown, D.G., Unified approach to the detection and classification of speckle texture in diagnostic ultrasound, *Opt. Eng. 25*, 738-742 (1986).

II

Texture of B-mode Echograms: 3-D Simulations and Experiments of the Effects of Diffraction and Scatterer Density

B.J.Oosterveld   J.M.Thijssen   W.A. Verhoef

B-mode echograms were simulated by employing the impulse response method in transmission and reception using a discrete scatterer tissue model, with and without attenuation. The analytic signal approach was used for demodulation of the rf A-mode lines. The simulations were performed in 3-D space and compared to B-mode echograms obtained from experiments with scattering tissue phantoms. The average echo amplitude appeared to increase towards the focus and to decrease beyond it. In the focal zone, the average amplitude increased proportionally to the square root of the scatterer density. The signal-to-noise ratio (SNR) was found to be independent of depth, i.e., 1.91 as predicted for a Rayleigh distribution of gray levels, although a minimum was found in the focal zone at relatively low scatterer densities. The SNR continuously increased with increasing scatterer density and reached the limit of 1.91 at relatively high densities ($> 10^4$ cm^{-3}). The lateral full width at half maximum (FWHM) of the two dimensional autocovariance function of the speckle increased continuously from the transducer face to far beyond the focus and decreased thereafter due to the diffraction effect. The lateral FWHM decreased proportionally to the logarithm of the scatterer density at low densities and reached a limit at high densities. Introduction of attenuation in the simulated tissue resulted in a much more pronounced depth dependence of the texture. The axial FWHM was independent of the distance to the transducer to a first approximation and decreased slightly with increasing scatterer density until a limit was reached at densities larger than 10^3 cm^{-3}. This limit was in agreement with theory. The experiments confirmed the simulations and it can be concluded that the presented results are of great importance to the understanding of B-mode echograms and to the potential use of the analysis of B-mode texture for tissue characterization.

Key words: Acoustic speckle; attenuation; B-mode echogram; B-scan; diffraction; random scatter; texture.

1 Introduction

Since the advent of gray scale echography [1], it has become evident that texture of B-mode echograms obtained from parenchymatous organs (e.g., liver, kidney, pancreas, thyroid) may reveal the pathological state of these organs. Additionally focal lesions can often be detected due to local changes of the texture compared to the surrounding healthy tissue. The textural parameters are qualitatively expressed by terms like:

hyper-, or hypoechoic, coarse, or fine granular and regular, or irregular. These terms refer to the subjective evaluation of the first order and second order statistical characteristics of the texture. Apart from the question whether or not the textural changes reflect histological changes, or alternatively more macroscopic tissue alterations, it would be highly significant to investigate to what extent echographic images can reveal anatomic alterations of the tissue, or the reverse, to what extent the texture is determined by the physical properties of the employed radiation, i.e., the physics of the production of ultrasound and of the registration of echograms. The latter question has met increasing interest during the last years.

Burckhardt [2] and Abbott and Thurstone [3] considered the analogy of B-mode texture to laser speckle and derived the first order statistics (Rayleigh probability distribution) from the theory existing to describe the latter phenomenon [4]. These authors arrived at the conclusion that the first order statistics are independent of the aperture of the echographic system (i.e., the transducer). It can be deduced from their work that the actual distribution of the point-like scattering sites within a tissue does not influence the first order statistics (average echo level and signal-to-noise ratio) as long as the number of scatterers within the effective beam diameter is very large and the scatterers are randomly distributed in three dimensional space.

Bamber and Dickinson [5] investigated the texture produced by an inhomogeneous continuum model. This work was extended later on to the investigation of the second order statistics [6], but it was still confined to a two dimensional description of both the sound field and the tissue.

Flax et al. [7] made an analysis of B-mode texture generation also based on a two dimensional description and they compared second order statistics of the rf images to those of video (i.e., demodulated) images. They arrived at the description of the first order statistics in terms of the number of point scatterers inside the beam area, the scattering strength and the spectrum of the transmitted ultrasound pulse. The average echo amplitude level appeared to be proportional to the square root of the number of scatterers. The average spacing of amplitude maxima in the axial direction was shown to be inversely proportional to the bandwidth of the transducer. The lateral width, as described by the autocorrelation function of the video echogram, decreased with increasing number of scatterers to a lower limit equal to the autocorrelation of the rf point response. The latter result thus makes clear that not only the average echo amplitude but also the fineness of the (lateral) texture depends on the density of the scattering sites. A further result was that the lateral texture continuously increased with penetration depth.

Smith et al. [8] used tissue phantoms containing various densities and sizes of discrete scatterers to measure B-mode echograms. These authors employed a Fraunhofer directivity function in a narrow band description of the sound field and compared the experimentally derived lateral autocorrelation function of the texture to the theoretical predictions. The results showed a reasonable correspondence apart from a large deviation for small distances to the transducer face. However, a continuous increase of the lateral size of the texture was apparent. A systematic dependence of texture size on the number, or size, of the scatterers was not observed. Wagner et al. [9] gave a theoretical description of the axial and lateral autocovariance functions of the texture in the focal zone of a transducer. The derived dimensions of the so-called speckle cell

(as opposed to resolution cell, or two dimensional point spread function) showed a very simple relationship to the aperture size, the center frequency and the bandwidth of the transducer. The model predictions corresponded well with the results obtained from a tissue phantom both for the first order and the second order statistics.

Foster et al. [10] performed a more realistic simulation by employing the impulse response method [11] to calculate numerically the B-mode images from a three dimensional tissue model. They considered the first and second order statistics of the B-mode echograms in the focal zone of three different kinds of transducers and found an excellent correspondence between the results of the simulations and of experiments with a tissue phantom.

Recently, Smith and Wagner [12] recalibrated their speckle size values published before [9] to the more convenient full width at half maximum (FWHM) dimensions as employed by Foster et al. [10] and they found a close correspondence between the simulations and measurements by the latter authors and the predictions derived from their theory [9].

It may be concluded from literature that for a large scatterer density the texture of B-mode echograms is mainly determined by the physical properties of the transducer employed: the lateral speckle size by the diameter, the focal length, and the central frequency, the axial size by the bandwidth. The involvement of attenuation, which is frequency dependent, has not been investigated so far, and it must be remarked that the evidence discussed was obtained from B-mode images based on a linear amplification of the echo amplitudes. This condition is not met in commercial equipment, in which log compression and various kinds of postprocessing is contained.

In this paper, a realistic three dimensional simulation of a transducer with a weighting of the surface velocity [13] is employed to estimate the B-mode echogram from a 3-D discrete scatterer tissue model. The first and second order statistics of the texture are investigated systematically and quantitatively as a function of the distance to the transducer and of the scatterer density. The influence of a linear-with-frequency attenuation on the second order texture parameters has been explored. The results of the simulations have been compared to measurements made with gelatine-carbon powder phantoms and to *in vitro* obtained data from human liver. Furthermore, a comparison has been made with predictions based on the theoretical model of Wagner et al. [9] in the focal zone of the transducer. Thus a full picture is presented of the diffraction effects on the texture of B-mode echograms, which completes the analysis of diffraction effects in the estimation of attenuation and sound velocity presented by the authors elsewhere [14].

2   Theory

2.1   The pulsed sound field of a circular transducer (Fig. 1)

The sound pressure in an observation point P in front of the circular transducer is obtained from the velocity potential $\Phi(\vec{r}, t)$ by

$$p(\vec{r}, t) = \rho \frac{\partial}{\partial t} \Phi(\vec{r}, t), \tag{1}$$
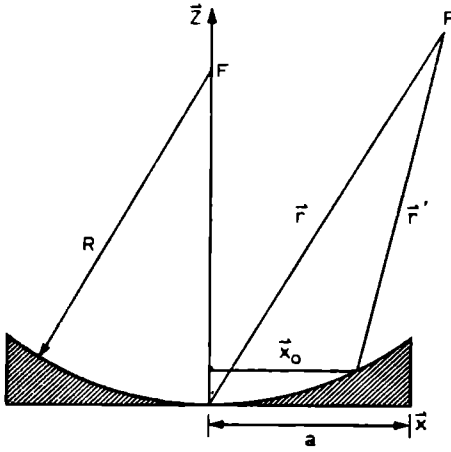
Figure 1: *Geometry of the focussed transducer and definition of the symbols*

whereas $\Phi(\vec{r}, t)$ can be obtained from the Rayleigh surface integral

$$\Phi(\vec{r}, t) = \iint\limits_{S} \frac{v_n(\vec{x}_0, t - r'/c)}{2\pi r'} dS, \tag{2}$$

with $\vec{r}$ = location vector of observation point P
v_n = normal surface velocity
t = time
$\vec{x}_0$ = location of surface element of transducer
r' = distance of P to surface element dS.

Equation (2) can be written as a convolution product

$$\Phi(\vec{r}, t) = v(t) * h(\vec{r}, t), \tag{3}$$

where $*$ denotes a convolution and $v(t)$ = time function of transducer pulse and

$$h(\vec{r}, t) = \iint\limits_{S} \frac{f(\vec{x}_0)\delta(t - r'/c)}{2\pi r'} dS, \tag{4}$$

with $f(x)$ = weighting function of surface velocity
$\delta(.)$ = Dirac function.

Combining equations (1) and (3), it follows that

$$p(\vec{r}, t) = \rho \frac{\partial v(t)}{\partial t} * h(\vec{r}, t). \tag{5}$$

Hence, the sound field can be calculated by estimating first $h(\vec{r}, t)$ and subsequently multiplying the result by the first derivative of the time function $v(t)$ and by the density of the medium ρ. The calculation can be generalized to curved transducers with an arbitrary axisymmetric velocity weighting function [13]. The reverse problem of reception of a spherical wave from a point scatterer can be described by the same set of equations. It is then possible to calculate the impulse response of the transducer and again of the rf waveform. If the electro-acoustical and the reverse impulse responses of

the piezomaterial are normalized the rf output voltage of the transducer resulting from a cloud of point scatterers can be given as (when assuming the Born approximation to be applicable, and only first order scattering to be present)

$$e(t) = \sum_{j=1}^{N} \rho \frac{\partial v(t)}{\partial t} * h_t(\vec{r}_j, t) * f_{sc}(\vec{r}_j, t) * h_r(\vec{r}_j, t), \tag{6}$$

with $\vec{r}_j$ = location of j-th scatterer

$f_{sc}(\vec{r}_j, t)$ = scatterer impulse response

$h_r(\vec{r}_j, t)$ and $h_t(\vec{r}_j, t)$ = transducer impulse response at reception and transmission, respectively.

Assuming isotropic scattering and taking $f_{sc}(\vec{r}_j, t) = 1$, equation (6) reduces to

$$e(t) = \rho \frac{\partial v(t)}{\partial t} * \sum_{j=1}^{N} \{h_t(\vec{r}_j, t) * h_r(\vec{r}_j, t)\}, \tag{7}$$

In practice, the term $\rho \partial v(t)/\partial t$ in equations (6) and (7) has to be estimated by measuring the echo waveform obtained from a small target at focus. For this condition, h_t and h_r are δ-functions of time. Taking the Fourier transforms of equation (7) yields

$$E(\omega) = \rho i \omega V(\omega) \sum_{j=1}^{N} \{H_t(\vec{r}_j, \omega) H_r(\vec{r}_j, \omega)\}. \tag{8}$$

The attenuation in tissues is generally described by

$$A(r_j, \omega) = \exp(-2\mu r_j \omega / 2\pi), \tag{9}$$

with μ the attenuation coefficient (Np/cm.MHz). Hence, in an attenuating medium the resulting spectrum will be

$$E_a(\omega) = \rho i \omega V(\omega) \sum_{j=1}^{N} H_t(\vec{r}_j, \omega) H_r(\vec{r}_j, \omega) A(r_j, \omega). \tag{10}$$

Calculation of the rf output by taking the inverse of equation (10) would result in rather time consuming calculations if large scatterer densities are considered. In the presented simulations a different approach is taken based on the observation that for a Gaussian envelope of $v(t)$ the linear-with-frequency attenuation results in a downward shift of the center frequency which is proportional to the travelled distance. This frequency shift was accomplished in the time domain on the waveform $v(t)$ at an average distance z_k of the simulated B-mode slices of 0.5 cm depth zone, i.e.,

$$v(z_k, t) = \frac{1}{\sqrt{2\pi}\sigma_t} \exp\left\{\frac{-(t-t_k)^2}{2\sigma_t^2}\right\} \sin\left\{(\omega_c - \frac{\mu z_k}{2\pi\sigma_t^2})t\right\}. \tag{11}$$

2.2 Statistics of B-mode echograms

2.2.1 First order statistics

Many rf traces were generated in the simulation program by translating the cloud with respect to the transducer in the lateral direction. Then the analytic signal was calculated

by taking the Hilbert transform of $e(t)$. Finally, the demodulation was accomplished by a calculation of the modulus of the analytic signal. When it is assumed that $e(t)$ is a random phasor, due to the large number of scatterers in a 3-D volume contributing to it at every moment after transmission, then it can be shown, that the probability density function of the amplitude after demodulation is [2,3]

$$p(A) = \frac{A}{\sigma^2} \exp\left\{-\frac{A^2}{2\sigma^2}\right\} \quad (A > 0), \tag{12}$$

with σ^2 the signal power. This probability distribution function is known as the Rayleigh distribution function and it can be shown that

$$
\begin{aligned}
\mu_A^2 &= \sigma^2 \pi/2 \\
\sigma_A^2 &= \sigma^2(2 - \pi/2)
\end{aligned}
\tag{13}
$$

in which μ_A = mean amplitude
$\quad\quad \sigma_A$ = standard deviation of the amplitude.

Hence,

$$\mu_A/\sigma_A = 1.91 \quad (= \text{signal-to-noise ratio, SNR}). \tag{14}$$

This property of equation (12) shows that the SNR of a medium containing a large number of scatterers is independent of the transducer and of the properties of the medium. Because the signal power is proportional to the number of scatterers, it follows from equation (13) that the average amplitude level is proportional to the square root of this number [7].

2.2.2 Second order statistics

The analysis of the second order statistics was confined to the autocovariance function (ACVF), which is a measure of the average size of the speckles in the B-mode image [15,9]. Since it has to be expected that the spatial properties in lateral (x) and axial (z) directions differ, the two-dimensional ACVF was calculated:

$$\text{ACVF}(x,y) = \iint_{region} dx'dz'\{A(x',z') - \langle A\rangle\}\{A(x'+x, z'+z) - \langle A\rangle\} \tag{15}$$

with A = amplitude
$\quad \langle A\rangle$ = mean value of the amplitude in the region involved.

An example of a 2D-ACVF of a slice of a B-mode echogram (2×0.5) cm is shown in figure 2a.

Every ACVF was characterized by the full width at half maximum (FWHM) sizes of its cross sections through the origin in lateral and axial directions, as shown in figure 2b.

A theoretical description was given by Wagner et al. [9]. They considered a tissue model with a large number of uniformly distributed, discrete, ideal scatterers. For the case that the time waveform of the transducer had a Gaussian envelope and the impulse response of the transducer may be separated in a part depending on the lateral coordinate and a part depending on the axial coordinate, the following expressions were
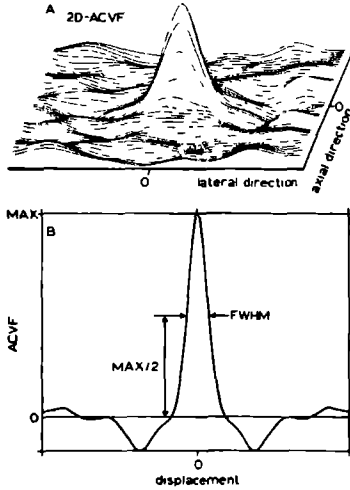
Figure 2: *a) Quasi three dimensional plot of a two dimensional autocovariance function (2D-ACVF). b) Definition of Full Width at Half Maximum (FWHM) of a cross section through the two dimensional autocovariance function.*

found for the FWHM's of the ACVF of the B-mode speckle in the focal zone of the transducer [12]:

$$\text{FWHM}_{lat} = 0.80\frac{\lambda F}{D'} \quad \text{with } D' = D/1.08 \tag{16}$$

$$\text{FWHM}_{az} = 2.17\sigma_z = 1.63\sigma_t = 0.26/\sigma_f \tag{17}$$

with F = focal distance of the transducer

D = diameter of the transducer

σ_z, σ_t and σ_f = standard deviation of the Gaussian sound pulse in the spatial (mm), time (μs) and frequency (MHz) domains respectively (FWHM_{az} in mm).

In discrete form, the ACVF in equation (15) can be written as [16]

$$c_{uu}(i,j) = \frac{1}{KM} \sum_{m=0}^{M-|i|-1} \sum_{n=0}^{N-|j|-1} \{u(m,n) - \langle u\rangle\}\{u(m+i,n+j) - \langle u\rangle\}, \tag{18}$$

in which $u(m,n)$ is a two dimensional array of amplitudes in the x and z directions respectively. Because c_{uu} may be considered as a convolution of $u(m,n)$ with $u(-m,-n)$, the ACVF can be easily calculated in the frequency domain after a Fourier transform:

$$C_{uu}(\omega_x,\omega_z) = U(\omega_x,\omega_z)U^*(\omega_x,\omega_z) = |U(\omega_x,\omega_z)|^2, \tag{19}$$

with C and U being the Fourier transforms of c_{uu} and $u(m,n)$, respectively. After transforming $C_{uu}(\omega_x,\omega_z)$ back to the spatial domain, the cross sections in the x and z directions are taken.

3   Tissue phantoms and experimental techniques

The basic material of the tissue phantoms consisted of degassed and distilled water
in which 5 percent gelatin was solved at 60°C. A powder of very fine carbon grains
($\simeq 30\mu$m diameter) was stirred through the material after which the cylinder (plexiglass)
containing the material was slowly rotated during the coagulation for 4 to 6 hours.
The dimensions of the phantom were 6 cm diameter and 8 cm height. The density of
scatterers was approximately 10^6 cm^{-3}, the sound velocity in the phantom was 1526 ± 1
m/s, and the attenuation $(1.7 \pm 0.2)10^{-2}$ Np/cm.MHz. The measurements described in
section 4.1.2 were performed with a focussed transducer (Picker) with $f_c = 5.6$ MHz,
$\sigma_f = 1.1$ MHz (almost Gaussian envelope, cf. Fig. 3), diameter 13 mm, and geometric
focus 7.25 cm. The experiments of section 4.2.2 were performed with a transducer
(Picker) with $f_c = 3.5$ MHz, $\sigma_f = 0.72$ MHz, diameter 19 mm, and geometrical focus at
9 cm. The transducers were connected to a transmitter/receiver system (custom made,
bandwidth 30 MHz, dynamic range 40 dB). The rf signal was linearly amplified and low-
pass filtered (15 MHz, fourth order Chebyshev filter). The signal was digitized with a 50
MHz sampling rate and intermediately stored in a transient recorder (Biomation 8100).
The digitization errors were reduced by time averaging 92 rf sweeps while systematically
changing the DC offset over 23 digitization levels during this procedure. The transient
recorder was software controlled by a PDP 11/34 computer (Digital Equipment). The
B-mode echograms were measured by using a scanning system (computer controlled
XYZ system, resolution 1 μm) which made a linear scan of 161 rf lines in steps of 0.125
mm. The rf lines were then software demodulated and stored for further processing.
During the scanning, the tissue phantom was placed in a temperature controlled water
tank at 20°C. The rf signals were always obtained from the same, windowed, slice of
the material 0.5 cm below the top surface and 0.5 cm thick. When the measuring
distance was changed the transducer was moved accordingly from, or to, this slice. The
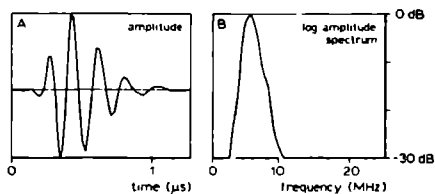attenuation over the small depth range of the slice was neglected.

Figure 3: *Echo waveform (a) and amplitude spectrum (b) of the transducer
used in the experiments with center frequency $f_c = 5.6$ MHz.*

4   Results

4.1   First and second order speckle statistics as a function of depth (diffraction effects)

4.1.1   Simulations

The simulated transducer had the following characteristics: velocity surface weighting function constant ($=1$), diameter $2a = 13$ mm, focus at 8 cm, central frequency $f_c = 5$ MHz, bandwidth $\sigma_f = 1.0$ MHz (Gaussian). A plot of the rf waveform and the spectrum are shown in figure 4. The tissue was modelled with a sound velocity of 1500 m/s and a scatterer density of 1000 cm^{-3}. The B-scans were simulated at mutual distances of 2 cm from 2 to 16 cm depth range and each B-scan consisted of 161 A-scan lines. The A-scans covered an area of 2 cm lateral and 0.5 cm axial. The tissue volume involved in the calculations was rectangular, with dimensions: $(10 \times 2 \times 0.8)$ cm. The B-mode pictures, obtained after normalization of the gray scale, are displayed in figure 5a.

The results of the first order statistics are shown in figure 6. Figure 6a shows the average echoamplitude levels versus depth and it will be evident that a maximum is reached at, or slightly before, the focus. The SNR ($= \mu_A/\sigma_A$) in figure 6b displays a slight decrease before the geometrical focus and approached the Rayleigh distribution limit (1.91, cf. section 2) for small and for large depths. The dip around the focus has to be explained by the decrease of the beam cross section in that region, whereby the total number of scatterers in the resolution cell volume becomes too low to obtain Rayleigh statistics.

The second order statistics are displayed in figure 7. The FWHM of the lateral ACVF as shown in figure 7a increases monotonically until far beyond the focus and decreases at still larger depths. This is a quite unexpected result, but, as will be discussed further on, it is confirmed by experiments. The decrease might qualitatively be explained by the rapid growth of the insonated volume (and thereby of the number of scatterers involved) beyond the focus, which as in the near zone yields a finer interference pattern. The FWHM of the axial ACVF (Fig. 7b) remains constant over the whole distance to a first approximation.

It is tentatively concluded from these results that the SNR and the axial FWHM are constant with depth, if the scatterer density is high enough (i.e., > 1000 cm^{-3}).
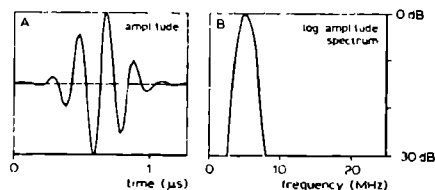
Figure 4: *Echo waveform (a) and amplitude spectrum (b) of the simulated transducer with $f_c = 5.6$ MHz.*
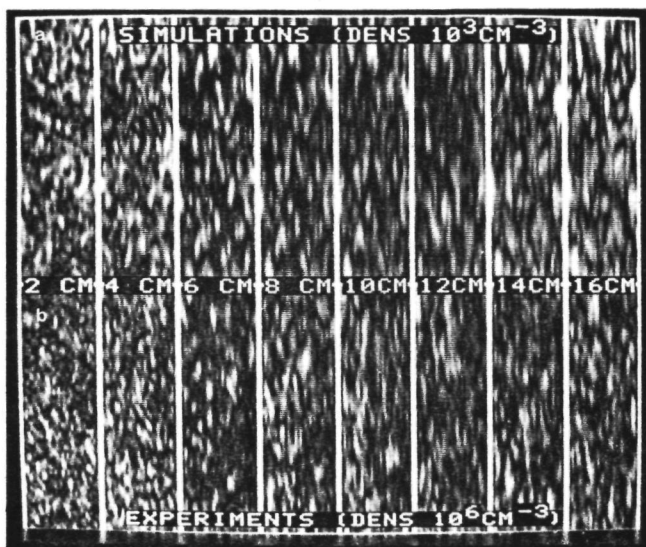
Figure 5: *B-mode scans (after gray level normalization) of a cloud of scatterers in a medium without attenuation at several distances to the transducer. The transducer is radiating from left to right. Dimensions: lateral × axial = 2.0 × 0.5 cm (161 × 334 samples). a) Simulations. b) Experiments using the 5.6 MHz transducer.*
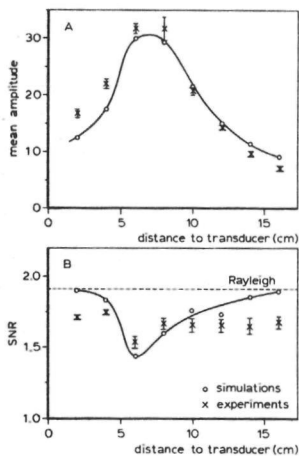
Figure 6: *First order statistics of simulated and measured B-mode scans as a function of distance to the transducer. a) Average amplitude, μ_A, b) Signal-to-noise ratio, $SNR = \mu_A / \sigma_A$.*
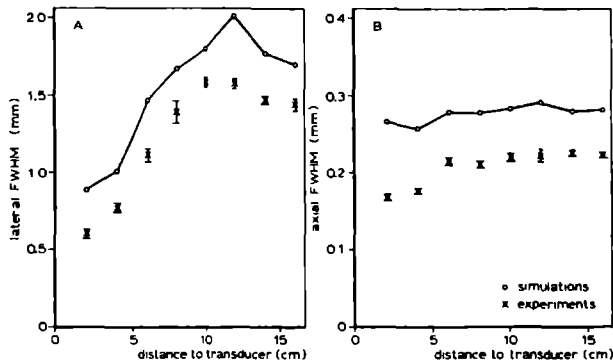
Figure 7: *Second order statistics of simulated and measured B-mode scans as a function of distance to the transducer. FWHM of the 2D-ACVF in lateral (a) and axial (b) directions.*

The average amplitude and the lateral FWHM depend greatly on distance and hence display a large diffraction effect.

4.1.2 Experiments

The experiments were performed with the set-up and the transducer as given in section 3. The B-mode echograms of the scans at $2, 4, \ldots, 16$ cm are shown in figure 5b. The results obtained for the average echo level are shown in figure 6a. As can be seen the experimental data points correspond closely to the simulations. On the contrary, the experimental SNR data (Fig. 6b) are much different from those of the simulations, although the trend is the same: a dip just in front of the focus. The short and long distance limits of the experimental data are well below the Rayleigh limit (1.65 instead of 1.91). A possible explanation may be that during the coagulation of the gelatin, some clotting of the carbon particles has occurred, thereby decreasing the scatterer density. The FWHM curves contradict this explanation. It can be seen in figure 7a that the lateral ACVF is lower than that for the simulations and has the same trend. Narrower ACVF's can be expected if the scatterer density is larger instead of lower! The axial FWHM values of the experiments (Fig. 7b) show a lower value before focus. The differences are small (15 percent) but statistically significant, as follows from the error bars given with the data points. Furthermore, the experimental data in figure 7b are much lower than those obtained from the simulations.

4.1.3 Attenuation

The data points of the simulations in figure 7a were recalculated after insertion of an attenuation slope constant of 0.1 Np/cm.MHz by using the linear-with-depth shift of the center frequency of the (Gaussian) spectrum (cf. section 2). The B-mode echograms resulting after gray scale normalization (i.e., ideal TGC) are shown in figure

Figure 8: *Simulated B-mode scans (after gray level normalization) of a cloud of scatterers in a medium without attenuation (a) and a medium with attenuation 0.1 Np/cm.MHz (b), at several distances to the transducer. The dimensions are the same as in figure 5.*

8b, together with those of the original data (like Fig. 5a) in figure 8a. It will be evident that a very dramatic effect on the lateral aspect of the texture is achieved by introducing attenuation. This is also quite clear in figure 9a in which the lateral ACVF width is drawn. Over a distance of 16 cm, a four fold increase of the FWHM is caused by the diffraction plus attenuation. The most striking feature of figure 9a is that the slope of the curves is steepest around the focus, the region preferred by ultrasonographers because of the good lateral resolution (for specular reflectors!) but apparently with the least constant lateral texture. The axial FWHM is not influenced very much by the attenuation (Fig. 9b).

4.2 First and second order statistics as a function of scatterer density

4.2.1 Simulations

The simulations were performed by using the performance characteristics of the transducer employed in the experiments: weighting function of the surface velocity $(1 - (x_0/a)^4)$, $f_c = 3.5$ MHz, $\sigma_f = 0.72$ MHz, diameter $2a = 19$ mm, geometric focus 10 cm. The time waveform of the transmission pulse and the logarithmic spectrum are shown in figure 10. The simulated tissue ($c = 1500$ m/s, no attenuation) was localized in the geometrical focal zone. The density of scatterers was changed from 100 to 19000 cm^{-3}. In order to diminish the uncertainty of the results, six B-scans were simulated for each density value. Six results for the first and second order statistics were thus obtained and the mean and standard deviation were estimated. The average figures together with the standard deviation thus obtained will be presented. The clouds of scatterers covered a
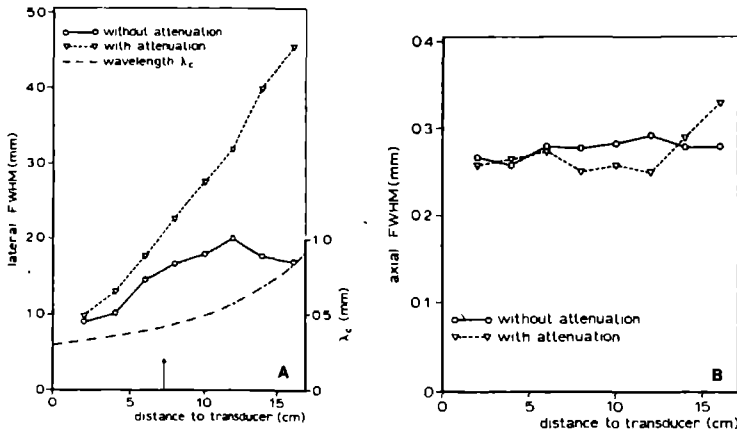
Figure 9: *Second order statistics of simulated B-mode scans as a function of distance to the transducer comparing a medium without attenuation with a medium with attenuation 0.1 Np/cm.MHz. FWHM of the 2D-ACVF in lateral (a) and axial (b) directions. The increase with distance of the centroid wavelength, due to the attenuation, is also plotted in (a).*

rectangular volume of $(6 \times 2 \times 0.8)$ cm^3 (x, y, z directions). The B-mode echograms are constructed from 161 scan lines over a 2 cm width and a 0.5 cm depth (cf. Fig. 11).

The average echo amplitude and the SNR versus scatterer density are shown in figures 12a and 12b, respectively. Since the density is plotted on a logarithmic scale figure 12a displays the expected square root dependence to the density (cf. section 2) over the range investigated. From figure 12b it becomes evident that the limit of 1.91 (Rayleigh distribution) will be reached for densities larger than 10^4 cm^{-3}. The results of the ACVF analysis are presented in figures 13a and 13b. The FWHM values of the lateral ACVF (Fig. 13a) decrease to a good approximation proportionally to the logarithm of the density up to the highest density 19000 cm^{-3} simulated. At higher densities, the lateral FWHM reaches a limit set by equation (16): FWHM$_{lat}$ = 1.96
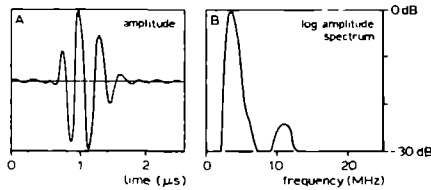
Figure 10: *Echo waveform and amplitude spectrum of the 3.5 MHz, D = 19 mm transducer, focussed at 9 cm, (Picker).*
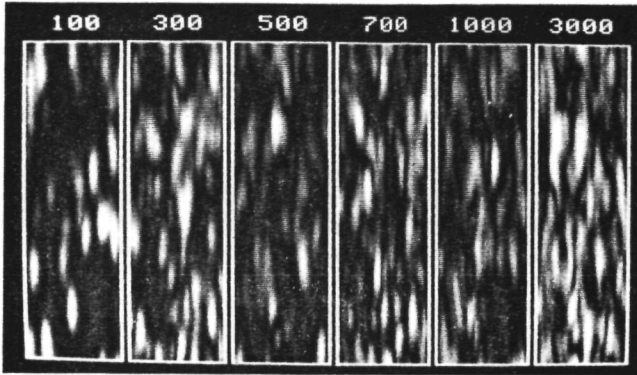
Figure 11: *Simulated B-mode scans (after gray level normalization) of clouds of scatterers with several densities, positioned in the focal zone of the 3.5 MHz transducer. The dimensions are the same as in figure 5.*

mm. This result of course indicates the usefulness of the lateral texture characteristics as a tissue typing parameter. This statement is however counterbalanced to a large extent by the result shown in figure 7a from which it has to be concluded that the lateral ACVF is greatly influenced by the diffraction of the transducer. The FWHM values of the axial ACVF (Fig. 13b) indicate that at densities larger than 1000 cm^{-3} the limit set by the bandwidth of the transducer is reached. Equation (17) yields a limit for the FWHM$_{ax}$ = 0.38 mm. This may indicate that the axial ACVF is not a good indicator of histologic tissue characteristics.

4.2.2 Experiment

Only one experiment was performed using the tissue phantom (cf. section 3). The characteristics of the employed 3.5 MHz transducer were slightly different from those used in the simulations (cf. section 3, section 4.2.1., Fig. 10). A number of 6 independent B-scans were registered and the following results were obtained:

$$
\begin{aligned}
\text{SNR} &= 1.7 \pm 0.1 \\
\text{FWHM}_{lat} &= 1.68 \pm 0.06 \text{ mm} \\
\text{FWHM}_{ax} &= 0.365 \pm 0.025 \text{ mm}.
\end{aligned}
$$

As in figure 6b, the SNR value is lower than would be expected from a scatterer density of 10^5 cm^{-3}. Due to the difference in focal distances between the simulated ($F = 10$ cm) and experimental ($F = 9$ cm) transducers, the value for the lateral ACVF could not be directly compared. For the experimental transducer (cf. section 3), equation (16) yields: FWHM$_{lat}$ = 1.76 mm, which is comparable with the experimental value of 1.68 ± 0.06 mm.

The axial FWHM is in good agreement with the theoretical value mentioned above.
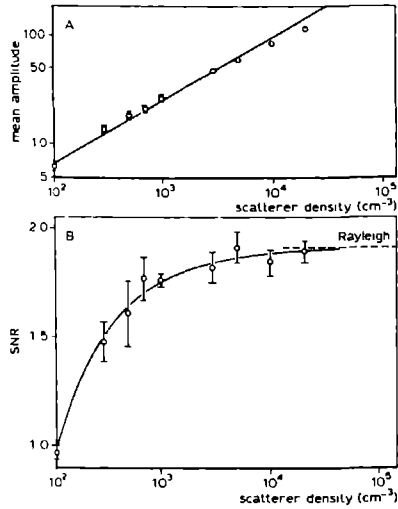
Figure 12: *First order statistics of simulated B-mode scans as a fuction of the density of the scatterers. a) Average amplitude, with drawn line displaying the theoretical square-root dependence [7], b) SNR, with theoretical limit of 1.91 set by Rayleigh statistics.*
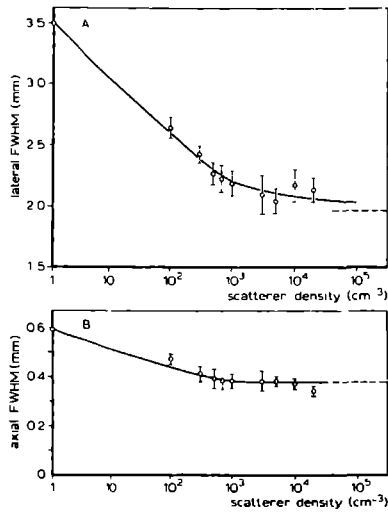

Figure 13: *Second order statistics of simulated B-mode scans as a function of the density of the scatterers. FWHM of the 2D-ACVF of the B-mode scans in lateral (a) and axial (b) directions.*

5   Discussion

5.1   Dependence of texture parameters on distance to the transducer: diffraction effects

The mean echo level appeared to increase monotonically towards the focus and to decrease beyond it. Several effects could explain this observation. The energy contained in the transmitted sound pulse remains constant, while the diameter decreases till the focus and increased beyond it. Therefore, the intensity increases until the focus and the inverse beyond it [17]. Furthermore, the number of scatterers contained in the pulse is subjected to the same but inverse proportionality. Since the backscattered intensity is proportional to this number, the effects of beam diameter and number of scatterers cancel each other out. The last effect concerns the inverse proportionality of the backscattered intensity that is received by the transducer to the square of the distance of the scatterers to the transducer. Therefore, it is to be concluded that the amplitude (mean) should be inversely proportional to the distance to the transducer. This dependency is observed only beyond the focus. The signal-to-noise ratio versus distance to the transducer displayed a minimum at focus (Fig. 6b). This minimum has to be explained by the decreased number of scatterers contained in the smaller pulse volume in the focal zone. This explanation is supported by the observation that both in the near field and the far field, the limit set by the Rayleigh distribution is reached. It may be concluded, that an *in vitro* investigation of the effective number of scatterers contained in a biological tissue can be optimally performed in the focal zone of a transducer. In *in vivo* conditions, small beam distortions by intermediate tissues might very much influence the pulse volume and hence the reliability of the results.

The axial FWHM of the 2D-ACVF showed a small but significantly lowered value in the region until the focal zone (Fig. 7b). An explanation for this behaviour could not be conceived, although it might be possible that at higher scatterer densities than employed in this study the theoretical constancy of the axial FWHM [9] will be better conserved. Insertion of the bandwidth of the transducers employed in the experiments and in the simulations into equation (17) yields the theoretical values of $FWHM_{ax} = 0.24$ mm and $FWHM_{ax} = 0.26$ mm, respectively, at the focal zone. The value of 0.26 mm is approximately 11 percent lower than that of the simulated points. The density of scatterers used in the simulations, however, was only 1000 cm^{-3}, which satisfies only marginally Rayleigh conditions, whereas the theoretical value is found at very large densities. So the results of section 4.2 show that this difference of the densities can explain the difference between theory and simulations. For the experimental transducer the theoretical value is 12 percent higher than the experimental $FWHM_{ax}$ values. This is almost the same correspondence as was found by Smith et al. [12] in the comparison of their theoretical values for the focal zone to the simulated and experimental values based on the work of Foster et al. [10], although the scatterer density they used was much higher (simulations: $3.3 \cdot 10^4$ cm^{-3}, experiments: $6.6 \cdot 10^4$ cm^{-3}).

The lateral FWHM of the 2D-ACVF increases from the transducer face to far beyond the focus. The assumption of a proportionality of the lateral width of the speckle to the distance to the transducer [8] is only confirmed in the focal region. The minimum lateral FWHM found in this study is of the order of two times the wavelength. Furthermore, the curves as found are sigmoid shaped, both for the experiments and for

the simulations. The experimental curve in figure 7a is lower than that for the simulations. The employment of equation (16) for the lateral FWHM at the focus yields for the employed transducer: $FWHM_{lat} = 1.27$ mm (experiments), and $FWHM_{lat} = 1.59$ mm (simulations). These values reasonably correspond to the data at focus in figure 7a. The difference of 0.3 mm appeared to be found at all depths. This observation is not easily understood, but it should be kept in mind that the scatterer density in both situations differs, so part of the explanation might be found in this difference.

The two striking effects of attenuation on the lateral FWHM versus depth curve (Fig. 9), i.e., the strongly increased lateral size of the texture and the disappearance of the decrease at large depths may be mentioned again. The value of 0.1 Np/cm.MHz (= 0.87 dB/cm.MHz) may be relatively large, but even for an attenuation coefficient that is half of this value the influence may still be called considerable.

5.2   Dependence of texture parameters on scatterer density

The average echo amplitude level appeared to be proportional to the square root of the density, as predicted by Flax et al. [7] from random-walk theory. This property makes the average echo amplitude a useful texture parameter for tissue characterization. The SNR reached the limit for a Rayleigh probability density function of 1.91 at densities above 10^4 cm^{-3}, or 10 mm^{-3}. This density is somewhat higher than the effective density of scatterers contributing to backscattering in the low megahertz frequency range in the liver [18]. Cloostermans et al. [19] observed in carefully controlled *in vitro* experiments with human liver biopsies a value of 1.1. The transducer they employed had a working frequency of 7.5 MHz, a focal distance of 6 cm, a bandwidth of 4 MHz and a diameter of 19 mm. In figure 12b a SNR of 1.1 is found at 125 cm^{-3} for the simulated 3.5 MHz transducer. The important quantity involved is the number of scatterers within the insonated volume. This volume is about 25 times smaller for the transducer employed by Cloostermans than for our transducer. Therefore the density number of 125 should be multiplied by 25 in order to obtain a situation comparable to the one in figure 12b. At the thus obtained density (3000 cm^{-3}) a value of 1.87 would have been found for our transducer. This value is almost at the limit (1.91) for high densities, therefore 3.5 MHz transducers are not suited to discriminate microstructural changes by SNR measurements.

The axial FWHM appeared to become independent of the scatterer density at values above 10^3 cm^{-3}. Dickinson [6], who employed the inhomogeneous continuum model observed an irregular, but, on the average, constant FWHM when the autocorrelation length of the model was changed. Unfortunately, all his figures were given in arbitrary units, so it is not possible to compare the results quantitatively to those given in this study. The limit value of the axial FWHM for large densities should for the employed transducer be 0.38 mm, when equation (16) given by Smith and Wagner [9,12] is used. This value is almost identical to the limit shown in figure 13b.

The lateral FWHM appeared to decrease proportionally to the logarithm of the density over a rather large range. The limit set by theory, equation (16), is 1.96 mm. The experimental value is lower, but this is to be expected. Dickinson [6] did not observe a monotonic relation between the lateral ACVF and the correlation distance. Transferring this result to the density data, it has to be expected that a decrease of the FWHM should be observed at very low scatterer densities. The FWHM of the ACVF

of the lateral point spread function appeared to be however 3.5 mm, which is on the continuous line in figure 13a, so the prediction by Dickinson is not confirmed.

5.3   Other dependencies

Although not explicitly investigated in this article several other dependencies can be pointed out based on literature, but which may need further investigation.

The diameter of the transducer and the beam diameter (nonfocussed transducer) will influence the average reflectivity level because the number of scatterers is proportional to the area of the cross section. The average echo amplitude is proportional to the square root of this number and therefore proportional to the diameter. The SNR may be dependent on the diameter for low scatterer densities. The axial FWHM is for relatively high scatterer densities independent of the diameter. The lateral FWHM is at focus proportional to the diameter [6,9,10,12].

The center frequency of the transducer governs the focal diameter [17] and thereby the lateral FWHM [9,10,12]. The axial FWHM is independent of the center frequency. Because of the frequency dependence of the focal diameter, the average echo amplitude will also be dependent on the center frequency. The SNR will only depend on this frequency for low scatterer densities.

The bandwidth of the transducer will influence the axial FWHM [9] in a predictable way. Because the focal diameter is also dependent on the bandwidth (pulsed model), a small influence will be present on the lateral FWHM.

Both the simulations and the experiments were based on a sound field undisturbed by the scattering of intermediate tissues. In *in vivo* conditions, however, distortion is to be expected by subcutaneous tissue layers. This influence has to be the subject of further studies prior to application of the results presented in this study to clinical echograms.

References

[1] Kossoff, G., Display techniques in ultrasound pulse echo investigations: a review, *J. Clin. Ultrasound 2*, 60-72 (1974).

[2] Burckhardt, C.B., Speckle in ultrasound B-mode scans, *IEEE Trans. Son. Ultrason. SU-25*, 1-6 (1978).

[3] Abbott, J.G., and Thurstone, F.L., Acoustic speckle: theory and experimental analysis, *Ultrasonic Imaging 1*, 303-324 (1979).

[4] Goodman, J.W., Statistical Properties of Laser Speckle Patterns, in *Laser Speckle and Related Phenomena*, J.C. Dainty, ed., pp. 9-75 (Springer Verlag, Berlin, 1975).

[5] Bamber, J.C., and Dickinson, R.J., Ultrasonic B-scanning: a computer simulation, *Phys. Med. Biol. 25*, 463-479 (1980).

[6] Dickinson, R.J., A Computer Model for Speckle in Ultrasound Images: Theory and Application, in *Acoustical Imaging*, Vol. 10, A. Metherell, ed., pp. 115-129 (Plenum Press, New York, 1982).

[7] Flax, S.W., Glover, G.H., and Pelc, N.J., Textural variations in B-mode ultrasonography: a stochastic model, *Ultrasonic Imaging 3*, 235-257 (1981).

[8] Smith, S.W., Sandrik, J.M., Wagner, R.F., van Ramm, O.T., Measurements and Analysis in Ultrasound B-scans, in *Acoustical Imaging*, Vol. 10, A. Metherell, ed., pp. 195-211 (Plenum Press, New York, 1982).

[9] Wagner, R.F., Smith, S.W., Sandrik, J.M., and Lopez, H., Statistics of speckle in ultrasound B-scans, *IEEE Trans. Son. Ultrason. SU-30*, 156-163 (1983).

[10] Foster, D.E., Arditi, M., Foster, F.S., Patterson, M.S., and Hunt, J.W., Computer simulations of speckle in B-scan images, *Ultrasonic Imaging 5*, 308-330 (1983).

[11] Stepanishen, P.R., Transient radiation from pistons in an infinite planar baffle, *J. Acoust. Soc. Amer. 49*, 1629-1638 (1971).

[12] Smith, S.W., and Wagner, R.F., Ultrasound speckle size and lesion signal-to-noise ratio: verification of theory, *Ultrasonic Imaging 6*, 174-180 (1984).

[13] Verhoef, W.A., Cloostermans, M.J.T.M., and Thijssen, J.M., The impulse response of a focussed source with an arbitrary axisymmetric surface velocity distribution, *J. Acoust. Soc. Amer. 75*, 1716-1721 (1984).

[14] Verhoef, W.A., Cloostermans, M.J.T.M., and Thijssen, J.M., Diffraction and dispersion effects on the estimation of ultrasound attenuation and velocity in biological tissues, *IEEE Trans. Biomed. Eng. BME-32*, 521-529 (1985).

[15] Papoulis, A., *Probability, Random Variables and Stochastic Processes* (McGraw Hill, New York, 1965).

[16] Oppenheim, A.V., and Schafer, R.W., *Digital Signal Processing* (Prentice Hall, Englewood Cliffs, 1975).

[17] Kossoff, G., Analysis of focussing action of spherically curved transducers, *Ultrasound Med. Biol. 5*, 359-365 (1979).

[18] Nicholas, D., Evaluation of backscattering coefficients for excised human tissues: results, interpretation and associated measurements, *Ultrasound Med. Biol. 8*, 17-28 (1982).

[19] Cloostermans, M.J.T.M., Mol, H., Verhoef, W.A., and Thijssen, J.M., In-vitro estimation of acoustic parameters of the liver and correlations with histology, *Ultrasound Med. Biol. 12*, 39-51 (1986).

III

Phase-Derivative Imaging I: Methods and Stabilization Analysis

R.L. Romijn   B.J. Oosterveld   J.M. Thijssen

The potential of using the phase derivative (PD) for echographic imaging was investigated. The PD data were calculated by four methods: zero crossing (ZCS) with squelch addition, analytic signal either with squelch addition (ASS) or with employment of a Wiener kernel (ASW), and unwrapped phase (UNP). The large peaks which occur in an unprocessed PD signal were "stabilized" by some kind of smoothing algorithm. The effects of the amplitude of the squelch signal and of the degree of smoothing were systematically investigated for experimental and simulated one and two dimensional RF echograms. The optimal pictures obtained for all four PD estimation methods were compared to the amplitude modulated (AM) image obtained from the same RF data. It is concluded that three different PD images can be derived: AM dominated (ZCS, ASS), mixed AM-PD (ASW) and pure PD (UNP) images. Some preliminary conclusions regarding the potential of PD imaging for medical diagnostics were drawn. These conclusions were based on quantitative first order statistics and on a qualitative assessment of second order statistics of the PD image texture.

Key words: FM imaging; instantaneous frequency; Phase derivative imaging; ultrasound.

1 Introduction

Conventional B-mode imaging is concerned with the envelope information contained in the recorded echo lines. The resolution and statistical properties in the depth direction of these images are mainly dependent on the bandwidth, which is inversely proportional to the time duration of the individual echoes. Additionally the instantaneous frequency might be employed as an information source as well. For instance, a smoothed version of this instantaneous frequency can be used to estimate the attenuation of ultrasound in biological tissues. Several methods to achieve this have been devised: zero-crossing density [1,2], peak shift of the amplitude spectrum [3], short-time Fourier analysis [4] (centroid shift of the spectrum) and smoothed phase derivative [5]. The latter method will be discussed more extensively in this paper.

The instantaneous frequency has been used in a somewhat different context, i.e., imaging the first derivative of the instantaneous phase of the echographic signals with respect to time [6,7]. For bandlimited and frequency-modulated signals, this method is equivalent to frequency demodulation. However, echographic signals basically result

from two kinds of interactions of ultrasound with tissue: pure reflections which, depending on the sign of the impedance discontinuity, are either zero phase or $\pm\pi$-shifted phase, and backscattering from a large number of small diffractive scatterers. In the latter case, which holds for most parenchymal tissues, the resulting signal can be described as a "speckle" pattern due to interference at the transducer face. Apart from the frequency shift caused by attenuation, it will be shown, that echographic signals can be more properly described as phase modulated signals rather than frequency modulated signals.

Imaging of the phase derivative might potentially be useful in revealing structural characteristics of tissues, which can be obscured in the envelope signal. For instance, constructive and destructive interferences will occur at random when the echoes arrive from gradually-deeper tissues and the corresponding phase jumps are not always clearly resolved in the envelope signal. This statement is equivalent to saying that the analytic signal that can be calculated for the echogram also has zeroes in the lower half complex plane [8]. This statement can be extended to the following: if an analytic function has no zeroes in the bounded lower half plane, then the original signal in the complex time domain will have only real zeroes (as follows from the Hermite-Biehler Theorem [8]). This means that the signal in real time is a real-zero signal as well, i.e., the signal can be completely characterized, except for a multiplicative constant, by its zero crossings. A technique to transform a signal into a real-zero signal has been used for some time in speech and communication technology and consists simply of the addition of an adequately-defined sine wave, the so-called "squelch" [8-10]. The method applies only to bounded and bandlimited signals. For this class of signals, it can be shown that a real-zero signal results if the amplitude of the squelch is larger than the maximum signal amplitude and its frequency larger than the highest signal frequency. This method has been introduced in medical ultrasound by Ferrari and colleagues [6,7] and elaborated by Seggie and Komaili [11-13]. These authors investigated the zero-crossing method to estimate the instantaneous frequency.

Another method for this estimation, also discussed by Ferrari [14] and Seggie [12], is the time derivative of the phase of the analytic signal. This derivative is quite unstable for two reasons: phase jumps may be discontinuous with time and, for small signal amplitudes, a recurrent undefined state is approached [13]. A "stabilization" may be achieved by adding a squelch signal, as mentioned above. A different approach for stabilizing the phase derivative has been proposed by Mesdag [5]. This author introduced a Wiener kernel, which contains an adjustable stabilization term. His first results were very promising, both for imaging purposes and, when using higher stabilization, for estimating the frequency shift due to attenuation.

In this paper, the three cited techniques: zero crossing estimation and phase derivative, both with the addition of a squelch signal, and the phase derivative with Wiener-kernel stabilization, are systematically investigated and the results compared to a fourth method: phase unwrapping followed by smoothing and differentiation with respect to time [15]. It will be evident that stabilization in this method is achieved by adequate low-pass filtering of the phase signal. Conclusions are drawn with regard to the most preferable stabilization approach for each method and to the optimality for the purpose of imaging. The results of the stabilization study were used in the investigation of beam diffraction effects on first and second order gray scale parameters of two-dimensional

phase-derivative (PD) echograms as described in a companion paper [16,17].

2   Generation of echographic data

2.1   Methods

Echographic RF signals were obtained in three different ways:

1. Radiofrequency echogram (1 line) obtained from a tissue-mimicking phantom, containing two low-amplitude regions. Transducer (Picker): 3.5 MHz center frequency, -6 dB bandwidth: 1.7 MHz, no TGC. Sampling frequency was 50 MHz.

2. Simulated 2-dimensional echogram: 161 lines, linearly scanned, of a scattering medium without attenuation. Density of scatterers 1000 per cubic centimeter, scattering volume in the focal zone of the transducer. Transducer characteristics as in 1. The simulation program calculated the echogram by using the impulse response method [18-20]. Sampling frequency was 50 MHz.

3. Echogram (2D) of a tissue-mimicking phantom (RMI). A volume was scanned which contained a low-contrast cylindrical region. Transducer and transmitter/receiver as in 1.

3   Instantaneous frequency estimation methods

3.1   Zero-crossing method

As described in the Introduction, the zero-crossing method yields a reliable instantaneous frequency estimate if a real-zero signal is available. This is achieved by adding a squelch signal to the original echogram:

$$x(t) = e(t) + A_s \cos(2\pi f_s t) \qquad (1)$$

where $e(t)$ = echogram

A_s = squelch amplitude $A_s \geq \max |e(t)|$

f_s = squelch frequency $f_s \geq f_{max}$.

The zero-crossings of $x(t)$ are estimated and the instantaneous frequency is obtained by taking the inverse of the time intervals between the zero crossings.

The radiofrequency echogram from a phantom (Methods 1) is shown in trace 1 of figure 1. The envelope is drawn as well, whereas the two low amplitude regions can be seen in the left and central parts. The instantaneous frequency signal was obtained after addition of a squelch signal of 5 MHz with amplitude increasing from 1 to 121 percent of the maximum of the envelope in traces 2 through 6. The average frequency was subtracted and then the signals were rectified and subsequently smoothed by a 0.4 μs cosine window. It will be evident that the peaks corresponding to destructive interference gradual disappear with increasing squelch amplitude. This is of course due to the fact that for low envelope levels, the instantaneous frequency is almost identical to the squelch frequency. Because of the subtraction of the mean frequency the resulting frequency signal tends to zero. Apart from details in the "texture", it can be concluded that a high squelch amplitude yields an "instantaneous frequency", or PD, signal which is equivalent to the original signal after amplitude demodulation.
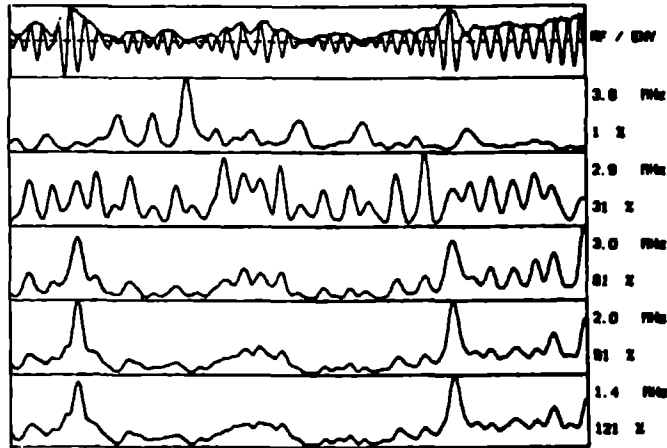
Figure 1: *Trace 1: RF echogram of tissue phantom with two low amplitude regions; AM drawn on top of the rf. Traces 2 through 6: PD echograms estimated by zero-crossing method (ZCS); squelch signal increasing from 1 to 121 percent of maximum AM level.*

In conclusion, the addition of a squelch signal does not bring about the desired improvement in the PD estimate by completion of the set of zero crossings. On the contrary, the AM information dominates the PD echogram at full squelch amplitude levels (91, 121 percent in Fig. 1), with only minor differences in amplitude contrast and axial resolution as compared to the conventional AM image. The phase information at higher amplitude levels is practically identical to the variations in the envelope due to the phase effects.

3.2 Phase derivative of the analytic signal and squelch addition

The envelope and the phase of a bandlimited signal can be obtained from the analytic signal, $a(t)$ [21,22]:

$$a(t) = e(t) + j\bar{e}(t) \tag{2}$$

where $\bar{e}(t) = e(t) * \frac{1}{\pi t}$ = Hilbert transform.

Then the envelope and the phase follow from:

$$|a(t)| = \sqrt{e^2(t) + \bar{e}^2(t)} \tag{3}$$

$$\phi(t) = \arctan\frac{\bar{e}(t)}{e(t)}. \tag{4}$$

The phase derivative (instantaneous angular frequency, frequency modulation) is then calculated by differentiation of equation (4):
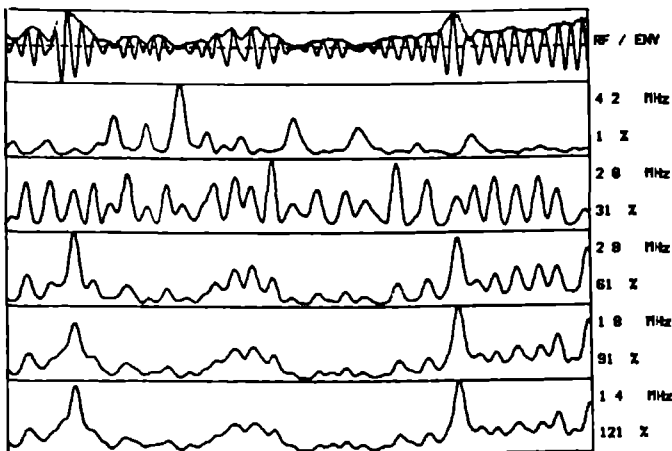
Figure 2: *Same as figure 1, PD estimated by analytic signal method and squelch addition (ASS).*

$$\phi'(t) = \frac{e(t)\tilde{e}'(t) - e'(t)\tilde{e}(t)}{|a(t)|^2}. \tag{5}$$

Equation (5) shows that the phase derivative becomes unstable if $e(t)$ approaches zero. The formula that results if a squelch signal is added can be found in [13]. The squelch signal yields a kind of stabilization of the phase derivative [11,12].

The method is illustrated by figure 2. As in figure 1, trace 1 in this figure shows the original RF signal and its envelope. The second trace shows the result of the PD after addition of a squelch signal with an amplitude of 1 percent of the maximum envelope. Apart from small details, this trace is identical to trace 2 in figure 1, i.e., phase transitions are quite well displayed because of smoothing after rectification of the PD signal and preliminary subtraction of the mean frequency (squelch + signal). The effects of increasing the squelch amplitude are similar to those described for the zero-crossing method.

In conclusion, the analytic signal method that includes a squelch signal to estimate the PD signal yields results which are practically identical to those of the zero crossing method. The conclusions formulated there apply to the analytic signal method plus squelch.

3.3 Phase derivative of the analytic signal and stabilization by Wiener kernel

In contrast to the two methods discussed above, stabilization of the phase derivative, or instantaneous frequency, is now achieved *a posteriori*. Therefore, the PD, as estimated by the analytic signal method as described in the previous section, is further processed by multiplication with a Wiener Kernel. This method was introduced by Mesdag [5]
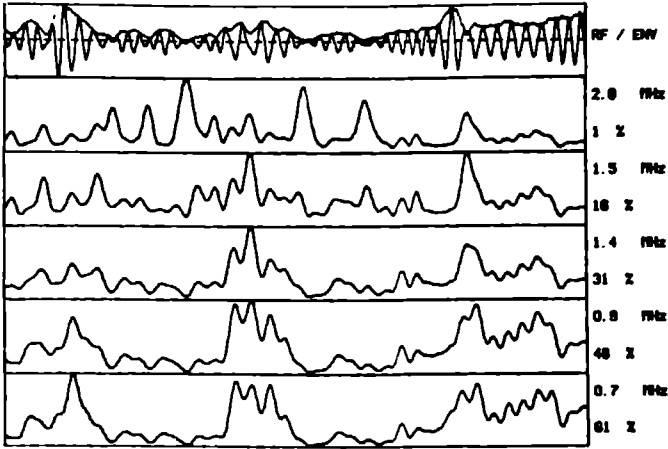
Figure 3: *Same as figure 1, PD estimated by analytic signal method and Wiener Kernel (ASW). Traces 2 through 6: stabilization factor in WK increasing from 1 to 61 percent.*

and proceeds as follows:

$$
\hat{\phi}'(t) = \begin{cases} \dfrac{2|a(t)|^2}{|a(t)|^2 + \varepsilon^2}(\phi'(t) - \omega_c) + \omega_c & \text{if } |a(t)| < \varepsilon \\[2em] \phi'(t) & \text{if } |a(t)| \geq \varepsilon \end{cases} \tag{6}
$$

where $\phi'(t)$ = new estimate of PD

ω_c = angular center frequency of ultrasound pulse

ε = stabilization factor.

The first right hand term of this equation is similar to a Wiener filter (in the frequency domain), where ε^2 then stands for the noise power [21].

As in the previous two methods, the PD is subsequently rectified and smoothed by a 0.4 μs cosine window.

The potential of the method is illustrated in figure 3. Trace 2 shows again almost pure phase information. Comparison with the corresponding traces in figures 1 and 2 leads one to conclude that the Wiener kernel yields a higher "contrast" of the phase transitions, even at the very low stabilization factor of one percent. The increase of this factor to levels over 30 percent produces a quite obvious enhancement of the PD at high levels of the envelope, while preserving the phase information in the "texture". Moreover, the resolution and the contrast are better than in the AM echogram.

In conclusion, the analytic signal method with Wiener kernel produces well-preserved phase information at amplitude levels which depend on the stabilization factor in the kernel. The contrast and "sharpness" of texture contours are also superior to those obtained by the previous methods.

3.4 Phase derivative from unwrapped phase

The alternative method to estimate the phase derivative from equation (4) is to calculate
the phase as a function of time explicitly and then perform a differentiation with respect
to time. The phase signal can be written as

$$\phi(t) = \omega_c t + \theta(t) \tag{7}$$

where $\theta(t)$ = stochastic phase term due to backscattering. Therefore,

$$\phi'(t) = \omega_c + \theta'(t). \tag{8}$$

Standard algorithms to calculate the phase angle from equation (4) are modulo 2π.
Therefore, a continuous phase versus time function can only be obtained if the disconti-
nuities produced by the algorithm at multiples of 2π are removed by a reset procedure,
which is known as "unwrapping" [23]. This technique was developed for the calcula-
tion of phase spectra by DFT algorithms, but was applied to the present problem by
the authors. The remaining discontinuities caused by the unwrapping were removed by
a variable length smoothing window (cosine). The phase versus time signal was then
differentiated with respect to time (Eq. 8), ω_c was subtracted and the resulting signal
was rectified. As before, the final processing step was a smoothing by a 0.4 μs sliding
cosine window that suppressed the large transients caused by the differentiation.

The quality of the PD signal produced by this method can be evaluated from figure
4. It is obvious that the resulting PD with only little smoothing prior to rectification
(trace 2) is almost identical to the corresponding trace in figures 1 through 3. Therefore,
the discontinuities caused by the unwrapping are of minor importance. Nevertheless,
the variable smoothing of the unrectified PD, as shown in traces 3 through 6, produces
remarkable effects. It is evident that the phase information is preserved and that the
effects at low envelope magnitudes (i.e., high PD peaks) are gradually suppressed. The
final trace (6) shows a PD signal that contains almost no amplitude information. The
phase information present in trace 6 displays constructive and destructive interference
effects equally well.

In conclusion, the unwrapped phase method produces a PD echogram that almost
exclusively contains phase information and no amplitude information. The deleterious
effects caused by very low, or zero, echo amplitude levels may be prevented by additional
amplitude weighting, or "hard" thresholding.

4 First order statistics of PD images

4.1 Zero crossing method

The 2-D RF echogram that was simulated as described in section 2 was processed
with five different amplitudes of the squelch signal, ranging from 1 to 121 percent, as
before. The histograms are shown in the left column of figure 5. It can be observed
that the histogram changes from almost exponential for the original PD data (1 percent
squelch amplitude) to a "Rayleigh"-like curve at high amplitudes of the squelch signal.
Summarizing statistical parameters are depicted in the right column of figure 5. The
top three graphs show a gradual decrease of the frequency range involved which starts

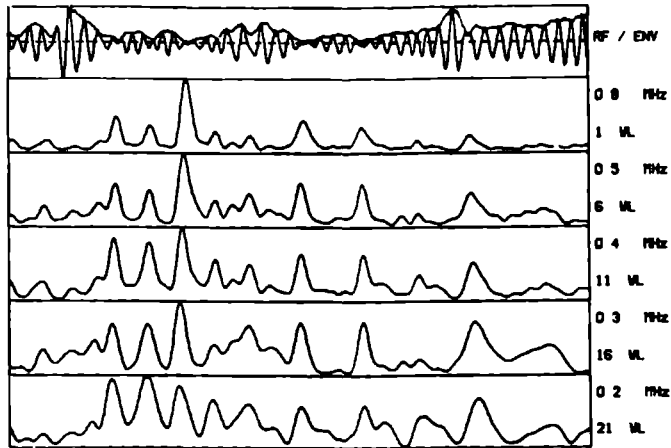**Figure 4:** *Same as in figure 1, PD estimated by unwrapped phase method (UNP). Traces 2 through 6: primary smoothing window length from 1 to 21 samples (50 MHz).*
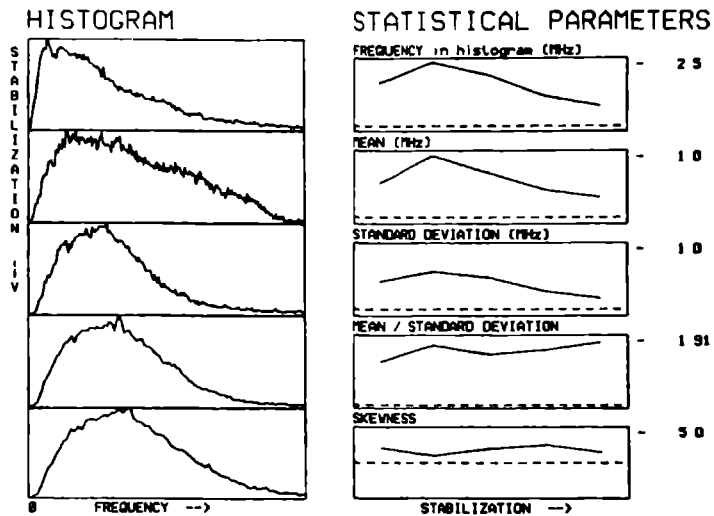
Figure 5: *First-order statistics of 2-D phase derivative image obtained from simulated rf data, ZCS method (Fig. 1). Left column: histograms obtained from PD images with increasing squelch amplitude. Right column: histogram parameters. Note different abscissas.*
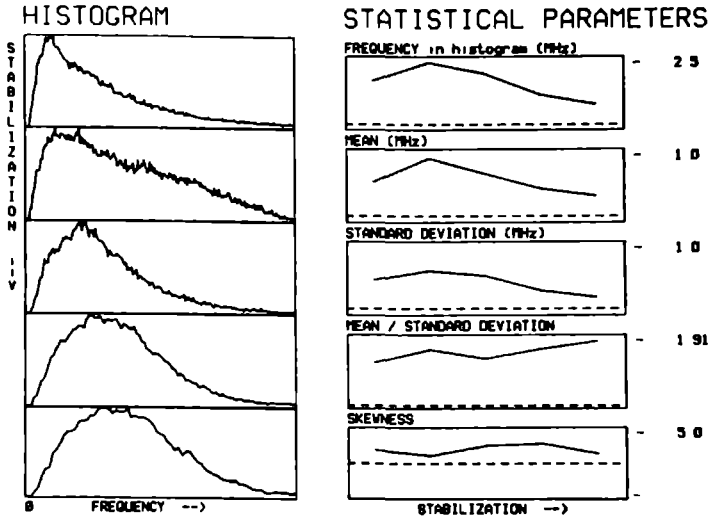
Figure 6: *Same as figure 5 for ASS method (Fig. 2).*

at 31 percent squelch amplitude. The mean over standard deviation, which is the "pixel signal-to-noise ratio" of the images, remains almost constant, although the highest value is found at 121 percent. It may be concluded, therefore, that a small enhancement of the available information is obtained by using the theoretically-optimum squelch amplitude. The ultimate value of the SNR equals 1.71, which is very close to the limit obtained for the amplitude-coded B-mode images [19,20] and which corresponds to the value for a Rayleigh probability distribution [21].

4.2 Analytic signal method and squelch addition

As was indicated in the previous section, this method yields practically identical results as the zero crossing method. Again, the results at a 31 percent squelch amplitude level are not monotonic with respect to those obtained at 1 percent level. The statistical measures (Fig. 6) confirm the observations that may be made from the histograms.

4.3 Analytic signal method and Wiener kernel

The histograms shown in the left column of figure 7 display a tendency to less skewness which is more subtle than in the two previous cases. In addition, the histograms become significantly smoother at the higher stabilization levels (46 and 61 percent, respectively). The right column in figure 7 displays a gradual decrease of the frequency span of the images, whereas the pixel signal-to-noise ratio remains constant at 1.58 over the whole range of stabilization levels, from 1 to 61 percent. Therefore, increasing the stabilization improves just the accuracy of the SNR estimates, while no bias is present in this method.

HISTOGRAM   STATISTICAL PARAMETERS
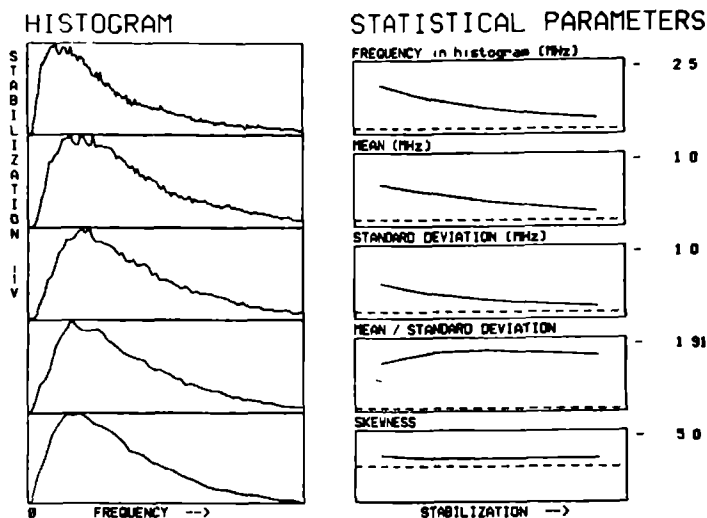
Figure 7: *Same as figure 5 for ASW method (Fig. 3).*

4.4   Unwrapped phase method

As remarked in the previous section, the stabilization applied to this method produces just a smoothing without the introduction of any influence of amplitude information. One might expect, therefore, a gradual decrease of the skewness of the histogram with increasing smoothing level (cf. Fig. 8, left column) and a corresponding decrease of the mean and standard deviations. The latter decrease becomes obvious from the graphs in the right column of figure 8. The SNR, on the other hand, displays only a minimal tendency to increase, reaching a final value at a 21-point window length (i.e., 0.4 μs) of the predifferentiation smoothing filter. The shape of the histograms does not change in the same way as in the other three methods. As can be seen, the low levels are preserved, which shows as a steep increase at these levels, but the peak of the histogram broadens. In other words, the tendency for a change from an exponential to a Rayleigh-like pdf is not found for this estimation method.

4.5   Conclusion

The addition of an optimal squelch signal yields a small improvement of the SNR of the PD images. The pdf approaches a Rayleigh distribution, which is expressed in an increase of the SNR value. It is questionable whether a PD estimation technique involving a squelch signal is relevant to imaging. The first-order statistics of the PD images obtained with the Wiener kernel, as well as with the unwrapped phase method, confirm the observations made in the foregoing section.
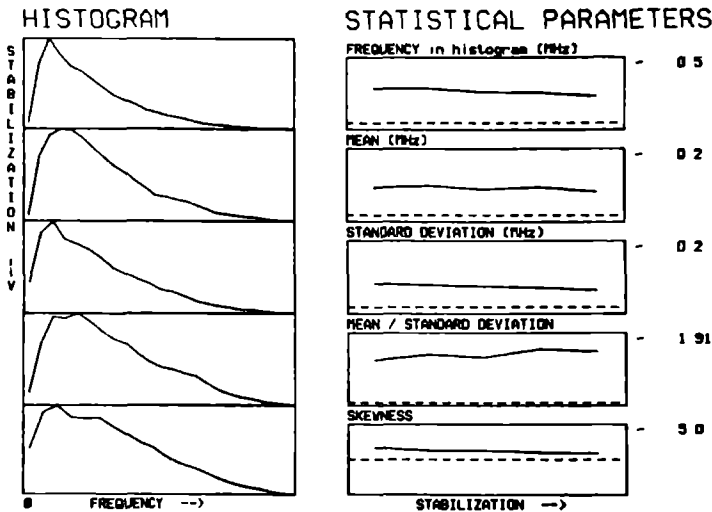
Figure 8: *Same as figure 5 for UNP method (Fig. 4).*

5 2-D phase derivative (PD) images

In this section, the images obtained from a simulation of a homogeneous and isotropically scattering medium and from a tissue phantom are shown and qualitatively evaluated. For a quantitative study, the reader is referred to a subsequent publication [17].

Figure 9 displays four rows of five images, all from the same simulation. Each row illustrates the effects of increasing degrees of stabilization from left to right (Section 3). In the top row, the results from the zero crossing method are shown, where the amplitude of the squelch is expressed as the percentage of the maximum RF amplitude over the whole picture. At 1 percent (leftmost picture in top row), a pure PD echogram is obtained; at 91 and 121 percent, the influence of the squelch is completed. The latter two pictures are rather similar to conventional (AM) B-mode images; whether the difference is significant cannot be decided visually. At intermediate squelch amplitudes, an "anomaly" occurs, which is quite evident at 31 percent. This phenomenon needs further exploration.

The second row from the top displays the images obtained by the analytic signal method and addition of a squelch. The differences from the top row are very small and may be insignificant.

The third row gives the results from the analytic signal method with a Wiener kernel. The stabilization factor ε (Section 3, Eq. (6)) is given as a percentage of the highest amplitude level. As before, the leftmost picture shows a pure PD echogram. In this row, the changes are gradual from left to right and the rightmost image displays an "AM-like" texture. However, the lateral "speckle" size (vertical in the images) is obviously much smaller than in the two top rows at high stabilization. This observation is in addition to the ones made in the previous sections regarding the axial texture characteristics.
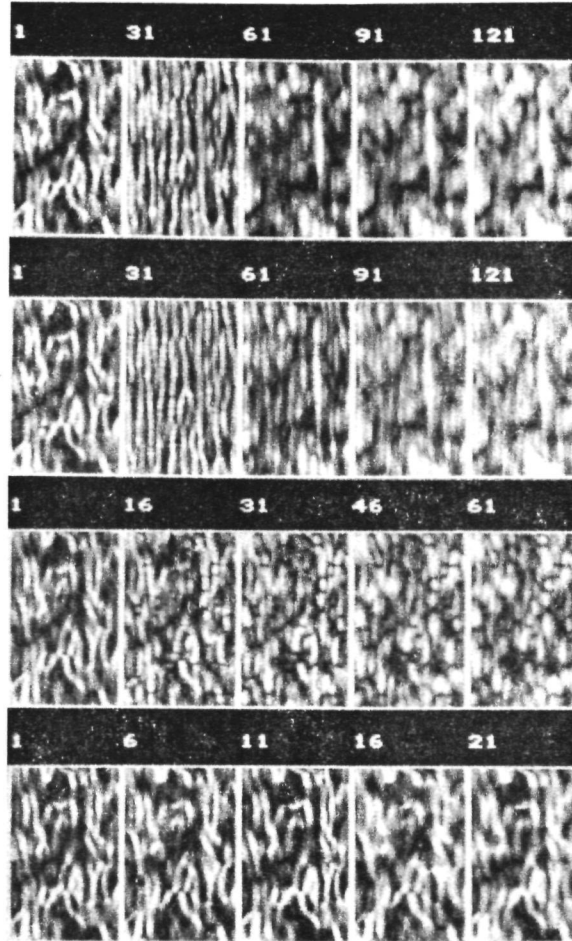
Figure 9: *2-D PD images obtained from simulated rf data. Top row: ZCS method: squelch amplitude from 1-121 percent. 2nd row: ASS method: squelch amplitude from 1-121 percent. 3rd row: ASW method: stabilization from 1-61 percent. Bottom row: UNP method: smoothing window length 1-21 samples.*

The fourth row (bottom) was obtained by the "unwrapped phase" method and the stabilization factor points to the length of the smoothing window as expressed by the number of signal samples involved (sampling rate 50 MHz). The pictures display a gradual coarsening of the texture in the direction of depth (horizontal) as can be expected from the increasing smoothing and small changes in the contrast. The pictures are quite different in texture from the "optimally-stabilized" images, i.e., the two rightmost of the other three rows. This observation confirms the one made in the previous sections regarding the 1-D echograms (i.e., axial direction only): this method produces images exclusively based on PD information.

A more adequate qualitative comparison between AM imaging and the various kinds
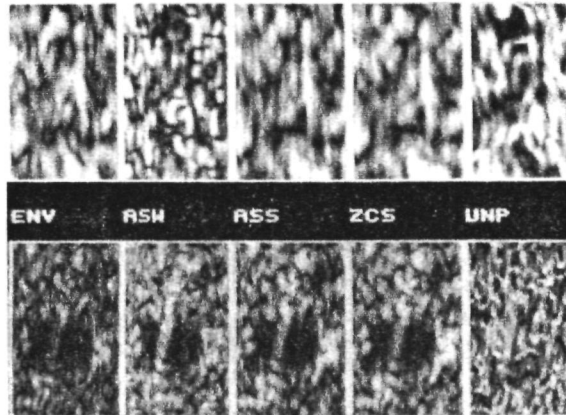
Figure 10: *Top row: AM image and optimum PD images of four estimation methods for simulated data. Bottom row: same for data obtained from tissue phantom.*

of PD images may be made with figure 10. In the top row, the results are shown which were obtained from the simulated data; in the bottom row, the results are from the data measured in the tissue-mimicking phantom. In the top row, the similarity already assumed becomes evident from the AM, i.e., envelope-detected image (ENV) and the images from the methods employing a squelch stabilization (ASS, ZCS). The Wiener kernel method appears not only to yield a diminished lateral "speckle" size but also an increased "speckle" contrast. In the lower row, the most salient picture is the rightmost one, which was obtained by the unwrapped phase method. It may be clear that the low amplitude "cysts" are completely absent. Further conclusions that may be drawn from section 3 are not clearly evident.

6 Discussion

In this paper, a heuristic approach has been followed to assess the potential of phase-derivative imaging, or FM imaging as it is sometimes called. The main conclusion from the comparitive study of four estimation methods is that a choice can be made between three different images: AM-dominated PD, mixed AM-PD and pure PD. The diagnostic value of these possibilities is not fully assessed in this paper. Some conclusions with regard to this question are evidenced nevertheless. The mixed AM-PD images produced by the analytic signal with Wiener kernel method display a smaller lateral width of the "speckle" and also good outlining of lesions, both by gray level contrast and by spatial resolution. These properties could be highly relevant in producing a valuable alternative to conventional AM B-mode images. The AM-dominated PD images, on the other hand, do not possess these qualities and are therefore less likely candidates for this purpose. The pure PD images, produced by the phase unwrapping method, are so different from AM images that intuitive conclusions can not easily be made. It is clear, however, that

amplitude (i.e., gray level) contrast is removed completely. Only if this information is replaced by a new parameter, would one expect any diagnostic value for the detection and differentiation of focal lesions. A likely candidate is a local instantaneous frequency contrast caused by the different backscattering transfer function of the lesion compared to that of the surrounding tissue. Evidence regarding the importance of PD images for the detection and differentiation of diffuse lesions may arise from a quantitative study of the first and second order statistics, which is described in a companion paper [17].

The data presented in this paper did not involve the possible effects of beam diffraction and attenuation. It may be anticipated, however, that in the process of image construction, problems will arise. The PD data are corrected for the mean frequency before rectification. Since beam diffraction influences the mean frequency in a nonmonotonic fashion when passing from the transducer face towards the focus and beyond [18], this effect has to be estimated for every transducer employed, and then accounted for. The attenuation produces a monotonic decrease of the center frequency with increasing depth [23,24]. Correct PD imaging, therefore, necessitates estimation and subsequent correction for the attenuation coefficient of the tissue prior to image formation.

References

[1] Ferrari, L., Jones, J., Gonzalez, V., and Behrens, M., In vivo measurement of attenuation based on the theory of Gaussian pulse propagation, *Ultrasonic Imaging* *4*, 178 (1982) (Abstract only).

[2] Flax, S.W., Pelc, N.J., Glover, G.H., Gutmann, F.D., and McLachlan, M., Spectral characterization and attenuation measurements in ultrasound, *Ultrasonic Imaging* *5*, 95-116 (1983).

[3] Dines, K.A., and Kak, A.C., Ultrasonic absorption tomography of soft tissues, *Ultrasonic Imaging 1*, 16-33 (1979).

[4] Fink, M., Hottier, F., and Cardoso, J.F., Ultrasonic signal processing for in vivo attenuation measurement: Short-time Fourier analysis, *Ultrasonic Imaging 5*, 117-135 (1983).

[5] Mesdag, P.R., *Estimation of Medium Parameters by Acoustic Echo Measurements* (Thesis, Delft University of Technology, 1985).

[6] Ferrari, L.A., Jones, J.P., Gonzalez, V., and Behrens, M., Acoustical imaging using the phase of echowaveforms, in *Acoustical Imaging, Vol. 12*, E.A. Ash, and C.R. Hill, eds., pp. 635-641 (Plenum Press, New York, 1982).

[7] Ferrari, L.A., Jones, J.P., Gonzalez, V., and Behrens, M., Ultrasound B-mode images derived from the phase of A-line echosignals, *Ultrasonic Imaging 4*, 192 (1982) (Abstract only).

[8] Requicha, A.A.G., The zeroes of entire functions: theory and engineering applications, *Proc. of the IEEE 68*, 308-328 (1980).

[9] Bar-David, I., An implicit sampling theorem for bounded band-limited functions, *Information and Control 24*, 36-44 (1974).

[10] Kay, S.M., and Sudhaker, R., A zero crossing-based spectrum analyzer, *IEEE Trans. Acoust. Speech Signal Proc. ASSP-34*, 96-104 (1986).

[11] Seggie, D.A., Leeman, S., Shin, S.B., Sankar, P.V., and Ferrari, L.A., The use of phase information in ultrasound imaging; in *Ultrasonic Tissue Characterization, Vol. 4*, J.M. Thijssen, and M. Smith, eds., pp. 59-66 (Fac. of Medicine Printing Office, Nijmegen, 1985).

[12] Seggie, D.A., Doherty, G.M., Leeman, S., and Ferrari, L.A., Ultrasonic imaging using the instantaneous frequency of pulse-echo signals, in *Acoustical Imaging, Vol. 14*, A.F. Berkhout, J. Ridder, and L.F. van der Wal, eds., pp. 487-496 (Plenum Press, New York, 1985).

[13] Komaili, J., Sankar, P.V., Ferrari, L.A., and Leeman, S., The instantaneous frequency of a sinewave squelched bandlimited signal, *Ultrasonic Imaging 8*, 285-295 (1986).

[14] Ferrari, L.A., Sankar, P.V., Fink, M., Shin, S.B., and Chandler, P., Use of signal phase in medical ultrasound, *Acta Electronica 26*, 111-120 (1984).

[15] Romijn, R.L., Oosterveld, B.J., and Thijssen, J.M., Calculation and stabilization methods of instantaneous frequency echograms, *Ultrasonic Imaging 8*, 42-43 (1986) (Abstract only).

[16] Oosterveld, B.J., Romijn, R.L., and Thijssen, J.M., Diffraction analysis of instantaneous frequency (FM) images, *Ultrasonic Imaging 8*, 43 (1986) (Abstract only).

[17] Oosterveld, B.J., Romijn, R.L., and Thijssen, J.M., Phase derivative imaging II: effects of beam diffraction and scatterer density, *Ultrasonic Imaging 11*, 153-174 (1989).

[18] Verhoef, W.A., Cloostermans, M.J.T.M., and Thijssen, J.M., Diffraction and dispersion effects on the estimation of ultrasound attenuation and velocity in biological tissues, *IEEE Trans. Biomed. Eng. BME-32*, 521-529 (1985).

[19] Thijssen, J.M., and Oosterveld, B.J., Texture in B-mode echograms: a simulation study of the effects of diffraction and of scatterer density on gray scale statistics, in *Acoustical Imaging, Vol. 14*, A.F. Berkhout, J. Ridder, and L.F. van der Wal, eds., pp. 481-486 (Plenum Press, New York, 1985).

[20] Oosterveld, B.J., Thijssen, J.M., and Verhoef, W.A., Texture of B-mode echograms: 3-D simulations and experiments of the effects of diffraction and scatterer density, *Ultrasonic Imaging 7*, 142-160 (1985).

[21] Papoulis, A., *Probability, Random Variables and Stochastic Processes* (McGraw Hill, New York, 1965).

[22] Whalen, A.D., *Detection of Signals In Noise* (Academic Press, New York, 1971).

[23] Dines, K.A., and Kak, A.C., Ultrasonic attenuation tomography of soft tissues, *Ultrasonic Imaging 1*, 16-33 (1979).

[24] Kuc, R., Schwartz, M., Von Miesky, L., parametric estimation of the attenuation coefficient slope for soft tissue, in *IEEE Ultrasonics Symposium Proceedings*, pp. 44-47 (IEEE in 1976 Cat. No. CH1120-5SU).

IV

Phase-Derivative Imaging II: Effects of Beam Diffraction and Scatterer Density

B.J. Oosterveld   R.L. Romijn   J.M. Thijssen

The potential of using the phase derivative (PD) of the radiofrequency echograms for producing two-dimensional grey scale images was further investigated. The PD images were produced by five different algorithms, which according to the results described in the companion paper yield PD images dominated by the amplitude (envelope, ENV), mixed PD-AM images and pure PD images. These images are termed according to their algorithms: ZCS, zero crossing counter with squelch; ASS, analytic signal with squelch; ASW, analytic signal with Wiener kernel; UNP, unwrapped phase; and SAS, smoothed analytic signal. The rf data were obtained from simulations and from experiments with a tissue mimicking phantom. PD images were analysed by calculation of the first and second order grey level statistics: mean level, signal-to-noise ratio (SNR) and the full width at half maximum (FWHM) of the autocovariance functions (ACVF). These parameters were systematically investigated for a range of depths with respect to the transducer and a range of scatterer densities of the insonated medium. The UNP and SAS images do not suffer much from the diffraction effect but do not display much information about the scatterer density either. The ASW and ASS images qualitatively display beam diffraction effects similar to those of the AM images, with the exception of the mean value which is at the minimum in the focus, where the AM yields a sharp maximum at that depth. The mean and the SNR of the ASW and ASS images increase with increasing scatterer density and saturate at a density of 5000 cm^{-3}. The mean value of the envelope, however, displays a square root dependency over the whole range. The axial and lateral FWHM of the ACVF of the UNP and SAS methods are not significantly dependent on the scatterer density and decrease with increasing density for the ASW and ASS images, as was observed in the envelope images. It may be concluded that ASW and ASS methods produce PD grey scale images which are equally well suited for the diagnosis of diffuse diseases of parenchymal tissues as conventional AM images. The smaller "speckle" size of the ASW images might be advantageous, for the detection of focal lesions, but the lesion contrast is found to be much lower than for the ENV.

Key words: Acoustic speckle; B-mode echogram; diffraction; FM imaging; frequency demodulation; Phase Derivative (PD) imaging; scattering; texture; ultrasound.

1 Introduction

The employment of the phase information in rf echo signals to construct a new type of B-mode images is receiving increasing interest. A few clinical studies in which commercial

frequency demodulation systems were used have even been published [1,2]. Some time ago, we started investigating various methods to obtain what we call "phase derivative" (PD) images and reported preliminary results [3,4]. Optimization of the stabilization methods and a comparison of the information content in the images produced by these methods have been reported in a companion paper [5].

The probability density function of the phase derivative or instantaneous frequency was derived by Rice [6] and recently by Broman [7] and Angelsen [8]. Rice also gave expressions for the autocorrelation function and the power spectral density. These only apply to the pure phase derivative. The estimate of the phase derivative, however, necessitates involvement of a stabilization, which will unavoidably affect the statistics of the phase derivative. Furthermore, we have chosen to use the rectified centralized phase derivative and to apply a smoothing operation before the imaging. This will affect the statistics even more. In the third paper in this series [9], we will derive expressions for the statistical properties of this kind of images. The analysis of the first order statistics in our first paper [5] revealed some quantitative insight in the statistical texture characteristics of echographic PD images.

In this paper, we discuss other interesting questions, which were investigated for conventional B-mode images and reported on by the present authors [10-12]. These concern the sensitivity of the PD images to the inhomogeneity of the sound beam due to focussing and diffraction ("diffraction effect"), and to the information contained in the images regarding the density of the scattering structures within the insonified medium. It is this latter question, that should be addressed in order to be able to assess the potential clinical relevance of PD imaging techniques.

2   Estimation of PD Echograms

In a companion paper [5], we described four different methods for estimating and stabilizing the phase derivative. In addition to these methods, a fifth method will be discussed here which was originally proposed by Angelsen [8] for the estimation of the frequency shift in Doppler signals (FM demodulation).

One can distinguish three different methods for estimating the phase derivative from the rf-signals:

- First, the estimation of the inverse of the time between successive zero crossings.

- Second, the estimation of the instantaneous phase from the rf signal $e(t)$ and its Hilbert transform $\tilde{e}(t)$ after unwrapping of the phase. One can determine its time derivative:

$$\phi'(t) = \frac{d}{dt} \arctan \left\{ \frac{\tilde{e}(t)}{e(t)} \right\} \tag{1}$$

- In the third method, the derivation is performed first on the arctangent which yields:

$$\phi'(t) = \frac{e(t)\tilde{e}'(t) - e'(t)\tilde{e}(t)}{|a(t)|^2} \tag{2}$$

where $a(t) = e(t) + j\tilde{e}(t)$ is the analytic signal corresponding to $e(t)$ and $|a(t)|$ is the envelope. We refer to this method as the analytic signal method.

Stabilization of equation (2) is necessary because the envelope $|a(t)|$ can become very small or even zero. Three stabilization techniques were used: addition of a squelch signal, weighting with a Wiener Kernel and smoothing. We investigated five combinations of estimation and stabilization of the phase derivative. For imaging purposes, each method was followed by the estimation and subsequent subtraction of the average instantaneous frequency followed by full wave rectification and low-pass filtering.

1. Zero crossing density with the addition of a squelch signal $(A_s \sin(\omega_s t))$ that is abbreviated as ZCS. As can be seen in figure 1, the time intervals (τ) between the zero crossings were estimated and the inverse of the intervals was then calculated (i.e., the instantaneous frequency).

2. Analytic signal method with the addition of a squelch signal $(A_s \sin(\omega_s t))$ abbreviated as ASS (figure 1, second column from left). The method proceeds with the calculation of the Hilbert transform of the resulting signal, $e(t) + A_s \sin(\omega_s t)$ followed by the calculation of the envelope $|a(t)|$ and the phase derivative according to equation (2).

3. Analytic signal method with a weighting by a Wiener Kernel (ASW). This method is illustrated in the third column from the left in figure 1. Since the first part of the calculations is identical to the one used in the previous method (ASS), this part is left open in the scheme. After the estimation of $\phi'(t)$ using equation (2), the centre frequency of the pulse of the employed transducer (ω_c) is subtracted and the result is then multiplied by a "Wiener" kernel as given in equation (6) in [5]:

$$
\hat{\phi}'(t) = \left\{
\begin{array}{ll}
\dfrac{2|a(t)|^2}{|a(t)|^2 + \varepsilon^2}(\phi'(t) - \omega_c) + \omega_c & \text{if } |a(t)| < \varepsilon \\[4mm]
\phi'(t) & \text{if } |a(t)| \geq \varepsilon
\end{array}
\right.
\tag{3}
$$

where $\hat{\phi}'(t) =$ stabilized estimate of the phase derivative,
$\varepsilon \quad =$ fraction of the maximum signal amplitude.

4. Unwrapped phase method (UNP), which is shown in the right column of figure 1. The instantaneous phase is estimated by taking the ratio of the Hilbert transform and the original rf signal and applying the arctangent operator as in equation (1). "Unwrapping" of the phase signal is necessary because of the modulo 2π output of the algorithm. Stabilization is achieved by low-pass filtering the unwrapped phase prior to derivation.

5. Smoothed analytic signal method (SAS). In this method, the denominator and the numerator of equation (2) are smoothed separately before the division is performed [17,18]:

$$
\hat{\phi}'(t) = \frac{\langle e(t)\tilde{e}'(t) - e'(t)\tilde{e}(t) \rangle}{\langle |a(t)|^2 \rangle},
\tag{4}
$$

where $\langle . \rangle$ denotes a smoothing operation. The stronger the smoothing, the more effective the stabilization will be.
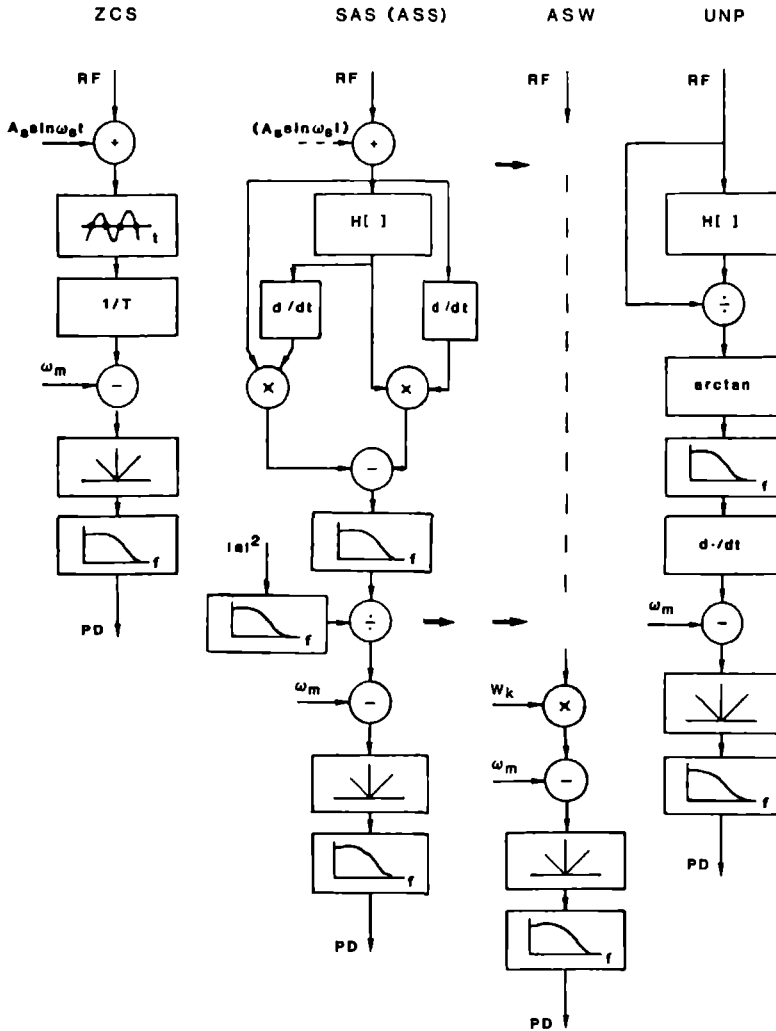
Figure 1: *Block diagram of the five methods of estimating the Phase Derivative (PD) echograms from the rf data. ZCS = zero crossings counter with squelch signal addition, SAS = smoothed analytic signal method [17]. ASS = analytic signal method with squelch addition, ASW = analytic signal method with Wiener kernel, UNP = unwrapped phase method (cf. [5]). The addition of the squelch signal to ASS is shown between brackets. The low-pass filters before the divison in SAS do not apply to the ASS and ASW.*

We concluded before [5] that both methods using squelch stabilization, ZCS and ASS, produce identical PD images. Since our results confirm this conclusion, we only reproduce the images and results of the ASS method in the figures.

3   Methods

The data employed in this study consisted of rf echograms obtained by computer simulation or by experiment.

3.1   Simulations

The computer simulated rf data were obtained by using the software package developed at our laboratory [13]. This package consists of a part which simulates ultrasound production and reception by a focussed transducer (impulse response method [14,15]) and a part that simulates a three-dimensional volume containing randomly distributed point scatterers. Two-dimensional line scans were produced by changing systematically the position of the transducer in a single plane with respect to the medium. The statistical properties of the B-mode scans obtained were verified by experiments [11], which showed that the simulations are realistic.

In the simulations, a circular single element transducer was employed with the following characteristics: centre frequency 5 MHz, standard deviation of the Gaussian spectrum 1 MHz, diameter 13 mm, focus at 8 cm and uniform surface velocity weighting function. The medium had a 1500 m/s sound velocity, no attenuation, and contained randomly distributed point scatterers with an average volume density as indicated with the results of the simulations. The simulated rf signals were sampled at 50 MHz.

3.2   Experiments

The effects caused by beam diffraction and focussing were investigated by the registration of rf-echograms from a tissue-mimicking phantom. The phantom was identical to the one employed in the former study on B-mode echograms [11]. It consisted of a 5 percent gelatin base material in which carbon powder (30 μm) was stirred before the congealing. The density of the scatterers was approximately 10^5 cm^{-3}, the sound velocity was 1526 ± 10 m/s, and the attenuation 0.15 ± 0.02 dB/cm.MHz. The transducer (Picker) had a diameter of 13 mm and the focus at 7.25 cm. The central frequency was 5.6 MHz and the "standard deviation" of the Gaussian spectrum was 1.1 MHz. The transducer was connected to a custom-made transmitter/receiver with a 30 MHz bandwidth. The rf signals were low-pass filtered by a 15 MHz 4th-order Chebyshev filter. The signals were digitized by a transient recorder (Biomation 8100) with a 50 MHz sampling rate (8 bits). The measurements were performed in a tank containing degassed distilled water at room temperature. The rf signals were time windowed at a depth 0.5 cm below the top surface of the phantom. The shift in the central frequency due to the attenuation in the phantom ($\Delta f \approx 0.01$ MHz) was neglected.

The various methods of producing PD echograms are illustrated by a clinical example: liver echogram of a healthy subject. This echogram was obtained with a mechanical sector scanner (Sonoline 3000, Siemens) employing a 3.0 MHz transducer. The data ac-

quisition was performed with a custom-made online system [16] at a digitization rate of
12 MHz (8 bits deep).

A squelch frequency of 8 MHz was employed in the simulations and experiments
with the 5 MHz transducer. For the in-vivo example, a squelch frequency of 3.0 MHz
was used, the centre frequency of the returned echo signals decreasing from 1.9 MHz to
1.6 MHz. The amplitude of the squelch signal was taken 120 percent of the maximum
amplitude of the rf signal. The stabilization term in the Wiener kernel (ASW method)
was taken at 30 percent of the mean signal power. The smoothing of the unwrapped
instantaneous phase (UNP) was performed by a 21 point sliding cosine window (duration
0.4 μs). In [5], these figures were estimated to yield optimal PD images. The final
smoothing operation (low-pass filter) on the rectified PD was performed by the same
21 point cosine window:

$$w(n) = \frac{1}{2}\left[1 - \cos\left(\frac{2\pi n}{N}\right)\right],\tag{5}$$

with $N = 21$.

The first and second order statistics of the PD images were calculated from the
"grey level" histograms (mean, and mean over standard deviation, SNR) and from the
autocovariance functions (ACVF). The two-dimensional ACVF is defined as:

$$R(x,y) = \iint_{area} dx'dz'\{A(x',z') \quad \langle A\rangle\}\{A(x'+x, z'+z) - \langle A\rangle\},\tag{6}$$

where A stands for the echo amplitude when the envelope is considered, or, in the
present case, for the rectified and smoothed PD.

4   Results

4.1   First and Second Order Statistics as a Function of Depth (Diffraction Effects)

4.1.1   Simulations

The PD images obtained from the simulated two-dimensional rf data are shown in figure
2 (increasing depth from left to right). The amplitude demodulated images indicated
by ENV are shown as well. A general trend can be visually appreciated that applies
to the series produced by all the methods: just as in the envelope images, the lateral
width (vertical) of the "speckle" increases with increasing depth. The eventual changes
of the mean grey level cannot be appreciated, because each image was normalized to

Figure 2: *Simulated grey scale images displaying the effects of beam diffraction
and focussing. The size of each image is 2 cm in the lateral (=vertical) direction
and 0.5 cm in the axial direction. The transducer is on the left transmitting to
the right. The distance from the transducer to the tissue are from left to right
2,4,6,8,10,12,14,16 cm indicated in the figure. a) envelope (ENV), b) ASW, c)
ASS, d) UNP, e) SAS.*
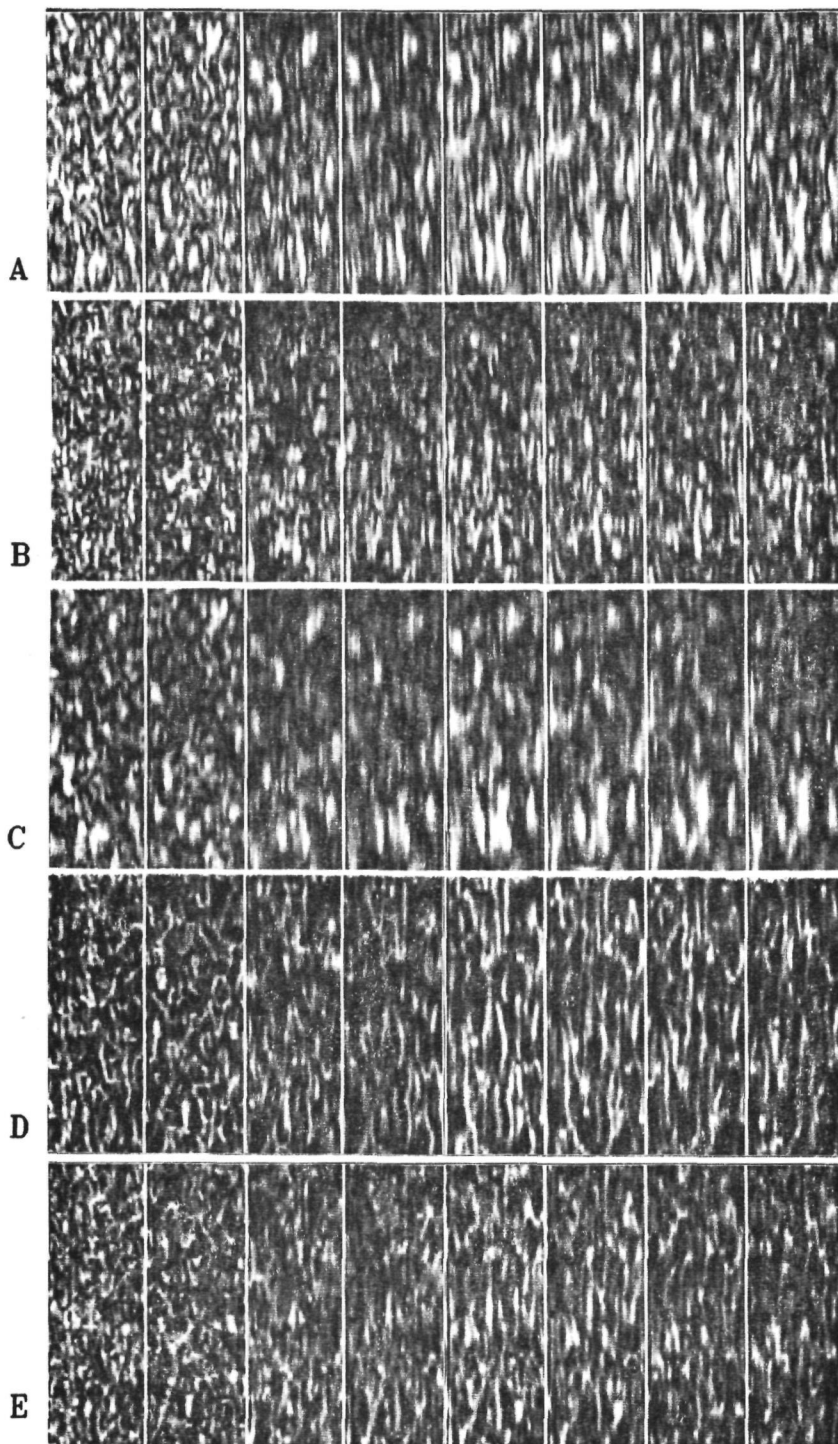
fit in the 64 grey levels of the display system. Furthermore, ASW echograms display a lateral speckle size smaller than that of the envelope or any of the other PD images. Finally, the UNP and SAS methods produce a texture that is different from that in all the other methods shown in figure 2 ("spaghetti-like").

We observe that the UNP method produces the purest PD images. In the other methods, envelope information is mixed to some extent with the PD information. The SAS images are closest in appearance to the UNP images. The ASW method incorporates envelope information to a "medium" extent. The ASS images are so much like the envelope images, that one has to conclude that not much PD information is left after the stabilization by a squelch signal.

Following this qualitative description of the most obvious characteristics of the PD images and of the effects of beam diffraction, we discuss the quantitative data of the first and second order statistics. The effects of beam diffraction on the first order statistics can be appreciated from figure 3. The analytic signal methods (ASS, ASW and SAS) display a trough in the depth range of the mean PD level at, or around, the focus as does the SNR vs. depth. As can be seen, the average of the envelope peaks at the focal distance, where the SNR has a minimum as well. The transient behavior of the mean of the envelope was attributed to the enhancement of the local intensity by focussing. The minimum of the SNR in focus was explained by the decrease of the sampling volume below a limit where the number of scatterers produces fully developed speckle (i.e., a Rayleigh pdf, with SNR = 1.91). These explanations may be applicable to PD images, because, as will be discussed below, the mean and SNR of the PD also depend on the scatterer density. The underlying mechanism is most probably the influence of echo amplitude inherent in the "stabilization" methods employed in the estimation of the PD.

The second order statistics are shown in figure 4. The axial FWHM of the ACVF appears to be fairly independent of depth for all the PD estimation methods (figure 4a). The PD data parallel the envelope data, but are 20 to 30 percent larger. The lateral FWHM data (figure 4b) gradually increase from a depth of 2 cm till beyond the focus (at 10 cm) and then stabilize, while the envelope data display a small decrease at large distances. The lateral size of the speckle of the ASW is of the order of 15 percent smaller than the ASS and the envelope. The UNP and SAS methods yield apparently an even smaller lateral size. This observation is not consistent with figure 2, where the lateral extent is shown to be larger. The explanation for this discrepancy is the strict processing of the autocovariance along the linear axial and lateral directions, while the UNP and SAS methods yield curled speckles.

4.1.2 Experiments

The effects of beam diffraction and focussing were investigated also by measurements with a tissue phantom. (Fig. 5). The results regarding the envelope of these measurements were in close agreement with the simulations, although in the previous publications [10-12] a density of 1000 cm^{-3} was used for the latter. As can be seen in figure 5a, the mean PD value does not change consistently with increasing depth. The UNP method produced mean values which are approximately 60 percent higher than for the other methods. The experimental envelope data showed a 200 percent increase of the mean in the focus.

Figure 3: *First order statistics of simulated PD images and ENV images vs. depth (cf. Fig. 2). a) mean grey level (frequency, amplitude), b) signal-to-noise ratio (SNR).*

The experimental SNR results are shown in figure 5b. As a general conclusion, it can be stated that at or near the focus, a minimum occurs, which confirms the simulation results (Fig. 3b). The SNR values obtained by the ASS method appear to be higher than 1.91 (i.e., for a Rayleigh distribution), as was observed for the simulations (Fig. 3b). The SNR of the envelope shows a small but significant decrease in the focus [11] which confirms the simulation result (Fig. 3b).

The experimental results of the PD speckle size (ACVF) are shown in figure 6. The axial FWHM displays almost no dependence on the distance to the transducer. Only the ASS method shows a small continuous increase in the axial size with distance. It might be concluded that the axial FWHM is not much influenced by beam diffraction
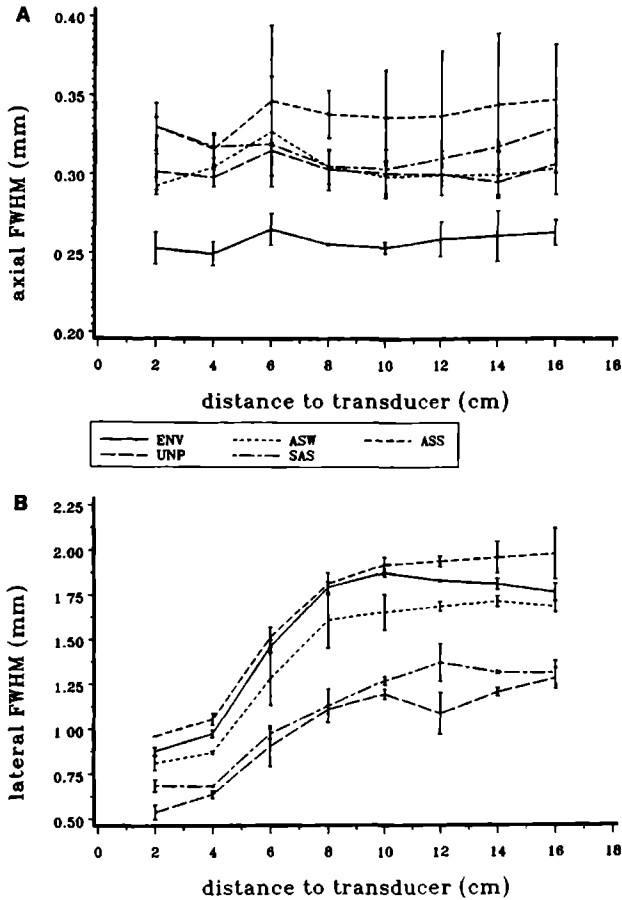
Figure 4: *Second order statistics of simulated PD images and ENV images vs. depth (cf. Fig. 2). a) axial full width at half maximum (FWHM) of the ACVF, b) Lateral FWHM of the ACVF.*

and focussing. From figure 4a and figure 6a, it becomes clear that the axial FWHM for the PD methods is consistently larger than for the envelope.

In figure 6b, the lateral FWHM of the PD speckle of the experimental data is displayed vs. distance. The relative increase with increasing depth is of the same order of magnitude as for the simulated data (Fig. 4b).

4.2   First and Second Order Statistics as a Function of Scatterer Density

Figure 7 displays examples of envelope and PD images obtained from simulations with varying density of scatterers. Because of the normalization of the gray levels in the various pictures, the changes in mean level are not displayed in figure 7. However,
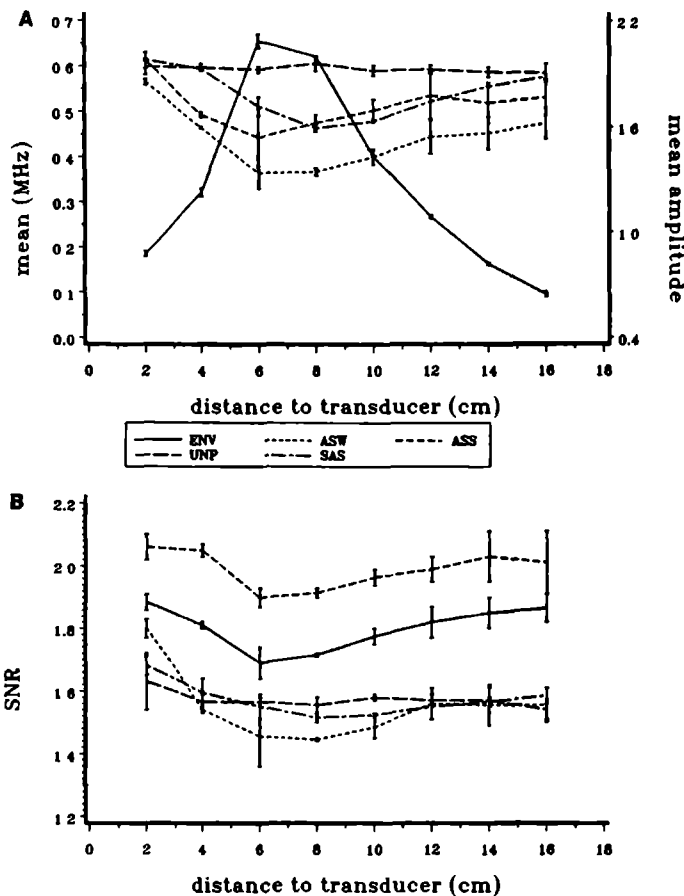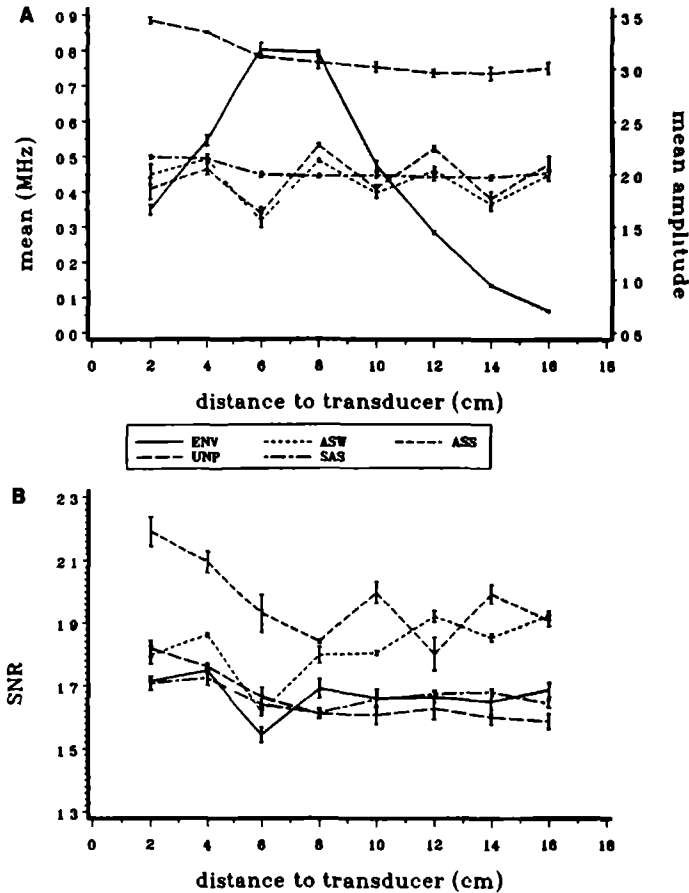
Figure 5: *First order statistics of experimental PD images and ENV images vs. depth. a) mean grey level (frequency, amplitude) b) SNR.*

several observations can be made with respect to the texture:

- the analytic signal method with squelch stabilization (ASS, Fig. 7c) yields pictures which are quite similar to the envelope pictures (Fig. 7a) as regards the size of the speckle and the gaps at low scatterer densities. The axial as well as lateral speckle sizes gradually decrease with increasing density.

- The Wiener kernel method (ASW, Fig. 7b) shows a distinct decrease of the axial speckle size. The lateral size is smaller than for the envelope and the ASS method over the whole range of densities and decreases also.

- The unwrapped phase method (UNP, Fig. 7d) and the smoothed analytic signal method (SAS, Fig. 7e) yield a definitely different kind of "speckle", which does not apparently depend on the density.
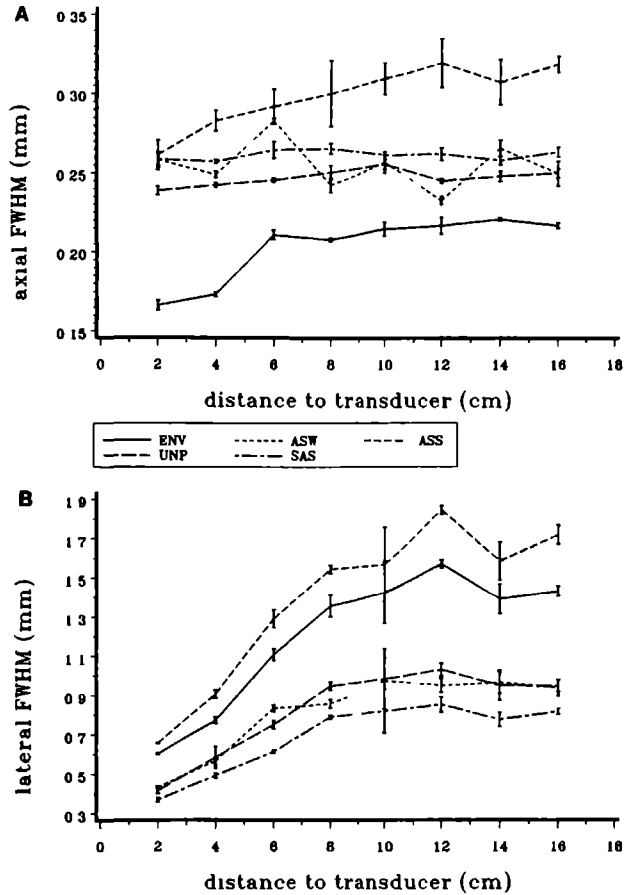
Figure 6: *Second order statistics of experimental PD images and ENV images vs. depth. a) axial FWHM of the ACVF, b) lateral FWHM of the ACVF.*

In our previous paper [5], we already concluded that the ASW method produces a display that is a mixture of amplitude and instantaneous frequency information. The results in figure 7 point to another important observation: the speckle density in these images is higher than for the envelope and ASS method.

In figure 8, the first order statistics of the PD methods, as well as of the envelope [8,9], as a function of scatterer density, are shown. The PD methods involving the envelope magnitude (ASS, ASW) produce an increase of the mean in the range of densities from 100 to approximately at 5000 cm^{-3} and then level off at a constant value. The average amplitude of the envelope in figure 8a is displayed by using a logarithmic ordinate, and thus demonstrates a square root dependence. The UNP and the SAS data do not display any significant change of the mean value with density.
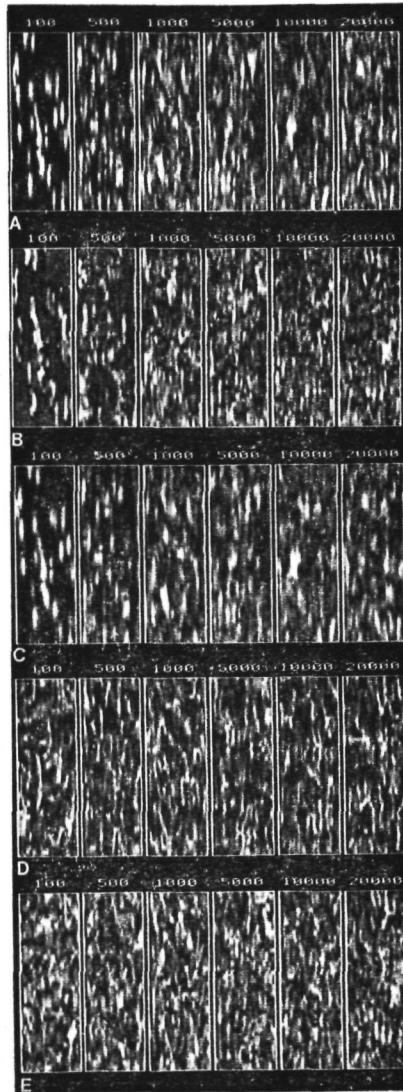
Figure 7: *Grey scale images of ENV and PD methods (ASW, ASS, UNP and SAS) simulated with scatterer density ranging from 100 cm^{-3} to 2.10^4 cm^{-3}.*
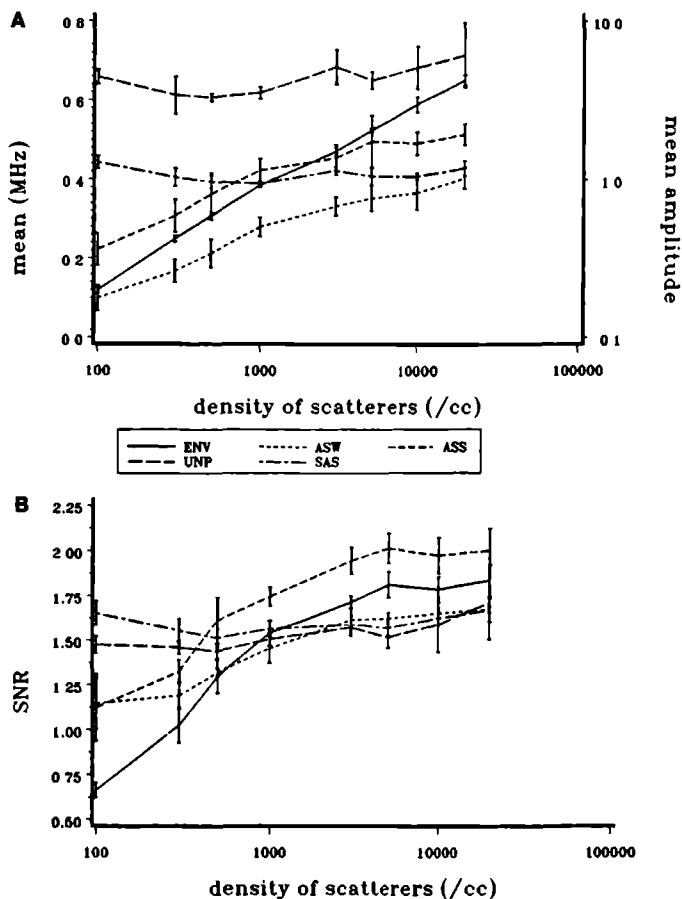
Figure 8: *First order statistics of PD and ENV images (cf. Fig. 7) for a range of scatterer densities. a) mean grey level (frequency, amplitude), b) SNR.*

The SNR data are summarized in figure 8b. The envelope and ASS method approach a limit value above densities of the order of 5000 cm^{-3}. For the envelope, this limit equals 1.91, which corresponds to a Rayleigh distribution. The ASS method yields somewhat higher values than the envelope. The SNR produced by the ASW, SAS and UNP methods reaches a limit lower than 1.91: in the order of 1.60. It is even questionable whether the SNR produced by the UNP and SAS methods is dependent on the density at all.

The second order statistics of the PD methods are shown in figure 9, again over a range of scatterer densities from 100 cm^{-3} to 2.10^4 cm^{-3}. Figure 9a displays the FWHM of the axial ACVF. The axial speckle size of the envelope decreases continuously with increasing density. The ASS and ASW methods also show a decrease. This decrease
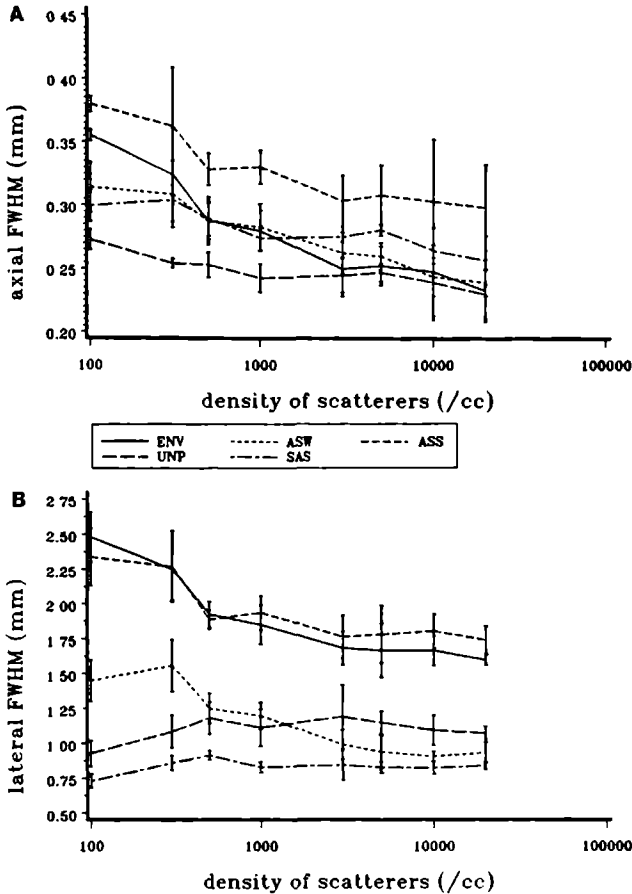
Figure 9: *Second order statistics of PD images and ENV images (cf. Fig. 7) for a range of scatterer densities. a) axial FWHM of the ACVF, b) lateral FWHM of the ACVF.*

is less pronounced than for the envelope. The SAS and UNP methods show almost no variation of the axial speckle size with density.

The results for the FWHM of the lateral ACVF (Fig. 9b) are quite similar to those of the axial ACVF in figure 9a. The ASS method follows closely the results of the envelope, whereas the ASW method yields a significantly lower, but still decreasing, size. The UNP and SAS methods display a low but constant lateral size.

When summarizing these results, it follows that the axial FWHM decreases by 25 percent (ENV, ASS, ASW) and the lateral width by 25 percent (ENV and ASS) and by 35 percent for the ASW method. Furthermore, none of the first and second order statistical parameters of the UNP nor of the SAS images exhibit a significant dependence
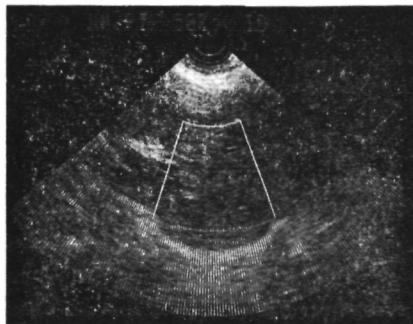
Figure 10: *Original B-mode image of liver of healthy subject; region of interest indicates area of rf data acquisition.*

on the scatterer density, a factor that excludes these methods for the differentation of diffuse diseases by PD texture analysis. A final conclusion from figure 9a and 9b is that the ASW method yields a much smaller speckle size than the envelope and the ASS method (of the order of 15 (axial) to 25 (lateral) percent). Therefore, the area of the speckle cell [19] produced by the ASW method is 60 percent of that produced by the envelope or the ASS method. For this reason, the ASW method offers a better means to detect focal lesions in a homogeneous tissue.

The devised PD estimation techniques are illustrated by a B-mode echogram obtained in vivo (Fig. 10). The region-of-interest (ROI) is indicated in the centre by a bright sector. The rf data from this region were collected in a single B-mode scan and, after complex demodulation, redisplayed without compression as an ENV image (Fig. 11, top). It can be noticed that the axial speckle size in the PD images is coarser than that of the ENV image. This is due to the final low-pass filtering of the PD data. The ASW shows a distinctly smaller lateral speckle size and some of the strong reflections are lost, but the contrast and the resolution for low reflective small areas (hepatic vessels) seems to be improved as compared to the ENV image (cf. [5]). The ASS method produces a lateral speckle size comparable to the ENV image and the high contrast regions are preserved. The UNP and the SAS images display a curled and laterally broad texture with a complete absence of the low reflective regions (vessels).

5   Discussion

The results presented in this paper confirm the conclusions presented in our previous paper [5]. The squelch stabilization technique (ASS and also ZCS) produces envelope dominated PD images, the Wiener Kernel stabilization (ASW) produces mixed ENV-PD images and the stabilization methods that involve only a smoothing (SAS and UNP) procedure pure PD images.

The PD images were obtained after rectification and subsequent low-pass filtering of the instantaneous phase derivative minus its local average. This procedure is analogous
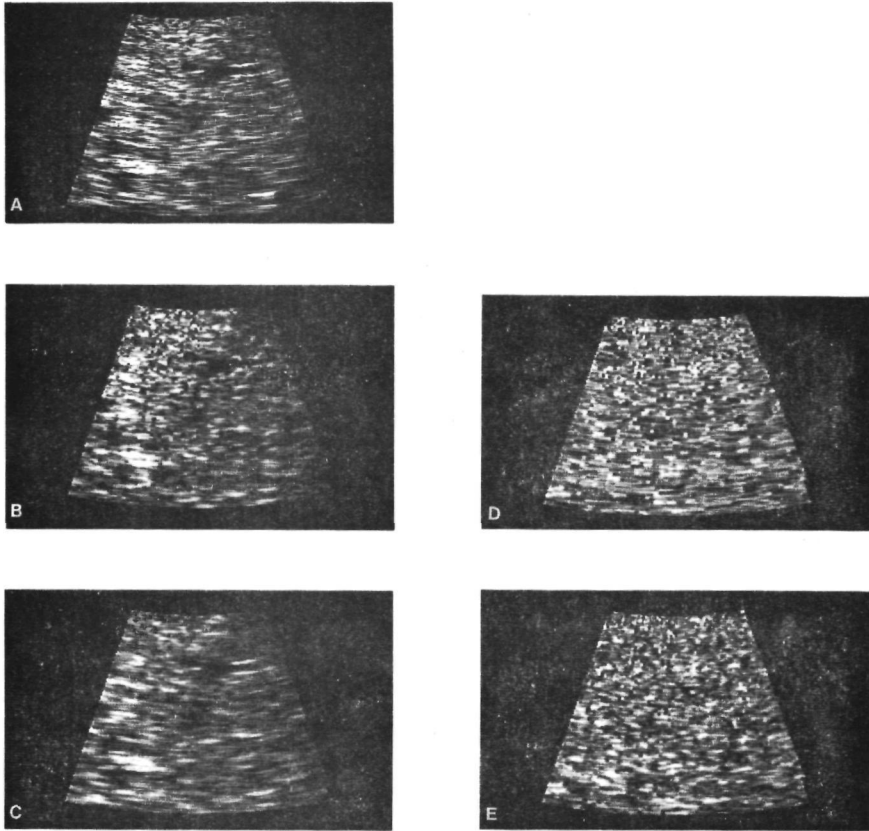
Figure 11: *From top to bottom: a) redisplay of ENV of ROI in figure 10, b) ASW, c) ASS, d) UNP, e) SAS.*

to that employed to process the rf signals when producing B-mode images. However, one should keep in mind that like the envelope, the phase derivative is a low frequency process [6], which means that the spectra lie around $f = 0$. For this reason, it is not possible to apply the complex demodulation procedure to the PD signals [20].

All the stabilization methods yield PD images that suffer from beam diffraction effects. However, the extent is not the same for all these methods. The expectation value of the unrectified instantaneous phase derivative is equal to the centroid frequency [8,9]. The local average of the PD is an approximation of the local centroid frequency. The depth dependence of the PD is the same as that of the centroid frequency [13]. The subtraction of the local average of the PD prior to the rectification removes this depth dependence. As a result, the mean PD estimated from the images (Figs. 3a, 5a) shows a depth dependence which differs from that of the centroid frequency. The purest PD images, obtained using the UNP method, show no significant beam effects at all. The mixing of PD with envelope information is the cause of the diffraction effects found with

the other methods. The same applies to the SNR. The second order statistics obtained by all the methods behave in the same way as the envelope. In the axial direction, there is almost no depth dependence and in the lateral direction, the speckle size increases until beyond the focal zone.

The stabilization methods that show the least beam influence (UNP and SAS) unfortunately also show the least sensitivity to the density of scatterers representing the tissue influence. Mixing more and more envelope with the PD (ASW, ASS) causes the PD images to become more and more sensitive to the density. This holds for all first and second order parameters that were investigated.

The ASS method yields images that look very much like the envelope images. The parameters calculated from the ASS images also show the same behaviour as the parameters from the envelope images, except for the average as explained above. The SNR found from the ASS images is 25 percent higher than the SNR found from the envelope. This may be attributed to the low-pass filter operation applied after the rectification of the PD to remove the sharp peaks. The filter reduces the standard deviation, but keeps the average the same which results in higher SNR. All the PD images yield larger axial speckle sizes than the envelope, which also may be attributed to the final low-pass filter, to some extent.

The ASW, SAS and UNP methods yield smaller lateral speckle sizes than the envelope as calculated with the lateral FWHM of the ACVF. The grey scale images in figures 2 and 7, however, indicate that this conclusion only holds for the ASW method. The SAS and UNP images show laterally extended curly speckles that are not aligned in the lateral direction. The calculation of the FWHM strictly in the lateral direction is not able to take this effect into account. The ASW, SAS and UNP methods also yield smaller SNR values than the envelope if the density of scatterers is high enough.

The ASS images do not add information about the scatterer density within the tissue to the information that can already be obtained from the envelope images. The observations made in reports of clinical studies [1,2] on the use of PD images obtained by a squelch method mainly concern an improved visibility of local abnormalities in the texture. The conclusion that this implies a correlation to hepatic structure is, however, questionable. The improvement was described by these authors as a connection of individual speckles in the depth direction. This tendency can be explained by the results in figure 9, where it is shown that the ASS method yields an axial speckle size 40 percent larger than the ENV method. The increased speckle contrast mentioned in [1,2] can be explained by the very small dynamic range of the PD signals as compared to the ENV signals. This effect is caused by the (partial) removal of the amplitude information: specular reflection levels do not differ much from speckle levels in PD images. The speckle contrast is then blown up by employing the full gray level range.

The SAS and UNP images do obviously not provide any information about the tissue at all. The ASW images which we qualified as mixed ENV-PD are the only sort of PD images that may add information to the information obtained from the envelope. The observation made in [5], that the ASW method yields smaller speckle sizes, is confirmed by the results presented in this paper (Figs. 2b, 7b and 11b). Since all four of the calculated statistical parameters depend on the density of scatterers, this observation may prove to be important. These properties may make the ASW image well suited for the detection of focal lesions, a task which benefits from having a large number of

independent speckles within the lesion area [21].

References

[1] Aufrichtig, D., Lottenberg, S., Hoefs, J., Ferrari, L.A., Friedenberg, R.M., Kanel, G., Cole-Beuglet, C., and Leeman, S., Frequency demodulated US: Evaluation in the liver, *Radiology 160*, 59-64 (1986).

[2] Ralls, P.W., Johnson, M.B., Kanel, G., Dobalian, D.M., Colletti, P.M., Boswell, W.D., Radin, D.R., and Halls, J.M., FM Sonography in diffuse liver disease: prospective assessment and blinded analysis, *Radiology 161*, 451-454 (1986).

[3] Romijn, R.L., Oosterveld, B.J., and Thijssen, J.M., Calculation and stabilization methods of instantaneous frequency echograms, *Ultrasonic Imaging 8*, 42-43 (1986) (Abstract only).

[4] Oosterveld, B.J., Romijn, R.L., and Thijssen, J.M., Diffraction analysis of instantaneous frequency (FM) images, *Ultrasonic Imaging 8*, 43 (1986) (Abstract only).

[5] Romijn, R.L., Oosterveld, B.J., and Thijssen, J.M., Phase-derivative imaging I: Methods and stabilization analysis, *Ultrasonic Imaging 9*, 147-161 (1987).

[6] Rice, S.O., Statistical properties of a sine wave and random noise, *Bell Systems Technical Journ. 27*, 109-157 (1948).

[7] Broman, H., The instantaneous frequency of a Gaussian signal: the one-dimensional density function, *IEEE Trans. Acoust. Speech Signal Proc. ASSP-29*, 108-111 (1981).

[8] Angelsen, B.A.J., Instantanous frequency, mean frequency, and variance of mean frequency estimators for ultrasonic blood velocity Doppler signals, *IEEE Trans., Biomed., Eng. BME-28*, 733-741 (1981).

[9] Thijssen, J.M., Oosterveld, B.J., and Romijn, R.L., Phase-derivative imaging III: theoretical derivation of first and second order statistics, *Ultrasonic Imaging* (in press).

[10] Thijssen, J.M. and Oosterveld, B.J., Texture in B-mode Echograms: a Simulation Study of the Effects of Diffraction and of Scatterer Density on Gray Scale Statistics, in *Acoustical Imaging*, Vol. 14, A.J. Berkhout, J. Ridder and L.F. van der Wal, eds., pp. 481-486 (Plenum Press, New York, 1985).

[11] Oosterveld, B.J., Thijssen, J.M., and Verhoef, W.A., Texture of B-mode echograms: 3-D simulations and experiments of the effects of diffraction and scatterer density, *Ultrasonic Imaging 7*, 142-150, (1985).

[12] Thijssen, J.M., and Oosterveld, B.J., Performance of Echographic Equipment and Potentials for Tissue Characterization, in *Procee- dings NASI on Mathematics and Computer Science in Medical Imaging*, M.A. Viergever and A. Todd-Prokopek, eds., pp. 455-468 (Springer, Berlin, 1988).

[13] Verhoef, W.A., Cloostermans, M.J.T.M., and Thijssen, J.M., Diffraction and dispersion effects on the estimation of ultrasound attenuation and velocity in biological tissues, *IEEE Trans. Biomed. Eng. BME-32*, 521-529 (1985).

[14] Stepanishen, P.R., Transient radiation from pistons in an infinite planar baffle, *J. Acoust. Soc. Am. 49*, 1629-1638 (1971).

[15] Verhoef, W.A., Cloostermans, M.J.T.M., and Thijssen, J.M., The impulse response of a focused source with an arbitary axisymmetric surface velocity distribution, *J. Acoust. Soc. Am. 75*, 1716-1721 (1984).

[16] Kruimer, W.H., Lammers, J.H.E., and Thijssen, J.M., Ultrasonic Biopsy Apparatus, in *Acoustical Imaging*, Vol. 14, A.J. Berkhout, J. Ridder, L.F. van der Wal, eds., pp. 665-667 (Plenum Press, New York, 1985).

[17] Papoulis, A., *Probability, Random Variables and Stochastic Processes* (McGraw Hill, Tokyo, 1965).

[18] Tsao, J.W., Morimura, S., Itoh, H., Itoh, I., and Konishi, T., Comparisons of images derived from amplitude, mean frequency and attenuation coefficient of pulse echosignals, *Jpn. J. Med. Ultrasonics 14*, 393-406, (1987).

[19] Wagner, R.F., Smith, S.W., Sandrik, J.M., and Lopez, H., Statistics of speckle in ultrasound B-scans, *IEEE Trans. Son. Ultrason. SU-30*, 156-163 (1983).

[20] Whalen, A.D., *Detection of signals in noise* (Academic Press, New York, 1971).

[21] Smith, S.W., Wagner, R.F., Sandrik, J.M., and Lopez, H., Low contrast detectability and contrast/detail analysis in medical ultrasound, *IEEE Trans. Son. Ultrason. SU-30*, 156-163 (1983).

V

Phase-Derivative Imaging III: Theoretical Derivation of First and Second Order Statistics

J.M. Thijssen   B.J. Oosterveld   R.L. Romijn

The echo signal obtained from a homogenous and isotropically scattering medium can be described as a Poisson time series which is convolved with the transmission pulse of the transducer. The probability density function (pdf) of this signal approximates to a Gaussian pdf for a narrowband pulse waveform. Methods to derive the phase-derivative (PD) signal from the complex envelope and the preenvelope of the echo signal are described. The first order pdf of the PD asymptotically becomes a Gaussian pdf by smoothing. Since the rectified PD is employed to obtain 2-dimensional grey scale images, the first order pdf as well as the signal-to-noise ratio (SNR) of this signal are also derived. The rectified PD is further smoothed by a cosine time window prior to the imaging. The SNR and the autocorrelation function (in the axial direction) of this latter signal can be derived under the assumption of a Gaussian spectrum of the transmission pulse. These first and second order characteristics of the PD images are calculated for the conditions employed in simulations and experiments reported previously and are quantitatively compared to the values obtained from these.

Key words: Acoustic scattering medium; demodulation; FM; instantaneous frequency; phase-derivative imaging; scattering medium. demodulation.

1 Introduction

The growing interest in the imaging of the phase information of echographic signals [1–9] induced a program in the authors' laboratory for a systematic evaluation. The approach reported on in two recent papers [10, 11] was basically similar to the one followed in the assessment of amplitude demodulated B-mode images [12–15]. However, prior to the evaluation of the so-termed phase-derivative (PD) images, a study was performed to assess the influence on the first and second order statistics of various approaches to estimate the PD, as well as of the degree of "stabilization" [10]. It was shown that the methods employing a squelch signal [16] yield PD images which are dominated by the envelope and, therefore, resemble greatly the conventional B-mode (ENV) images. The method employing a Wiener Kernel to stabilize the PD signals was shown to be characterized as a mixing of envelope and phase information and, finally, also "pure" PD images were obtained, by using the time derivative of the unwrapped smoothed phase.

The second paper [11] described quantitatively the first and second order statistical parameters of PD images derived by using five different estimation methods. These parameters were calculated from data obtained by realistic 3-dimensional simulations

of homogeneous media containing isotropically and randomly distributed scatterers. A large range of volume densities of the scatterers was employed. Moreover, the "diffraction effects", i.e., the influences of beam diffraction and focussing, on the statistical parameters were investigated.

In this paper, the first and second order statistics of the PD images are analytically derived in a stepwise fashion. The derivations are performed for the stabilization method which was called SAS in the second paper [11]. First, the concept of the PD is introduced while employing the complex envelope as well as the preenvelope (or analytic signal) of the rf signal. The first order probability density functions of the envelope, phase and phase derivative are obtained. In the next chapters, a method for estimating the stabilized PD signal is discussed, which produces a Gaussian pdf in a good approximation. Then, the mean, variance, and signal-to-noise ratio (SNR) of the rectified PD are derived from the pdf under the assumption of a Gaussian transmission pulse. Finally, the smoothing prior to the display of the rectified PD is introduced and analytic expressions for the SNR and the autocorrelation function are obtained.

2   Echogram of a homogeneous and isotropically scattering medium

Biological tissue is modelled as a medium with a constant speed of sound, containing scatterers which are distributed at random. The latter characteristic implies a homogeneous and isotropic distribution in space. For simplicity, the backscattering transfer function is taken to be frequency independent. The signal generating process can be considered then as a time series of impulses corresponding to a Poisson process. The impulses are convolved with the received echo waveform $h(t)$. This waveform is depending on the transmit/receive characteristics of the transducer, the transfer characteristics of the medium (attenuation) and the backscattering properties of the inhomogeneities within the medium. In the following, the medium is considered homogeneous and isotropic and attenuation is not taken into account. It is further assumed that the plane wave approximation is valid. The impulses are characterized by a random amplitude a_m and a phase ϕ_m. The phase can either be 0 or π, depending on the impedance of the scatterer with respect to that of the surrounding medium. The echo signal $x(t)$ (see Fig. 1a) can then be written as:

$$x(t) = \sum_{m=1}^{N} a_m h(t - t_m) \cos \phi_m, \tag{1}$$

where t_m = time of flight of the echo from scatterer m, $t_m \in (0, T)$

$\quad\quad T$ = duration of the echosignal

$\quad\quad N$ = number of echoes during time T (i.e., number of scatterers within the sampled volume).

The spectra of $x(t)$ and the related waveforms discussed further on are shown in figures 2a through 2g.

Taking the effective duration of the pulse waveform $h(t)$ equal to τ and the bandwidth $\beta = 1/\tau$, it can be stated that the transmission pulse is relatively narrow band if $\tau \gg T/N$, or $\beta \ll N/T$. For this condition, it can be shown [17,18] that the first
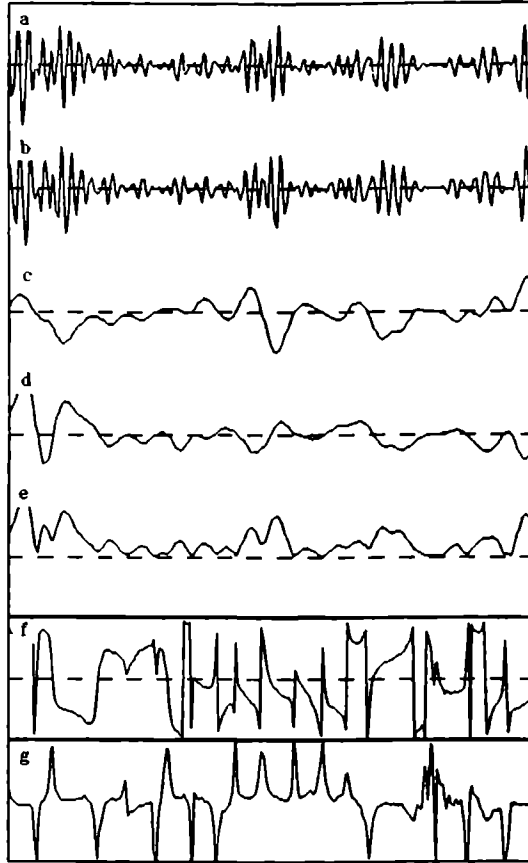
Figure 1: *a) Radiofrequency echogram $x(t)$ (Full time range = 7.5 μs, f_c = 7 MHz), b) Hilbert transform $\tilde{x}(t)$. c) Cosine component $a(t)$. d) Sine component $b(t)$. e) Envelope $e(t)$. f) Instantaneous phase $\theta(t)$ (range: $-\pi/2$ to $+\pi/2$). g) Phase derivative $\dot{\theta}(t)$ (range: 3 to 11 MHz).*

order probability density function of $x(t)$ is asymptotically Gaussian (central limit theorem). The power spectrum of $x(t)$, which is the Fourier transform of its autocorrelation function, can be derived from the characteristic function [17] and it approximates to:

$$S_{xx}(f) \approx \gamma \langle a_m^2 \cos^2 \phi_m w_h(f) \rangle_T \qquad (2)$$

where $w_h(f) = 2|H(f)|^2/\tau$, in which $H(f)$ is the Fourier transform of $h(t)$, and
$\gamma \quad = \overline{N}\tau/T$, for $\overline{N}$ = average number of scatterers.

Because $\cos \phi_m = \pm 1$ the term $\cos^2 \phi_m$ can be replaced by 1. Introducing $n = \overline{N}/T$, the average echo density, and inserting the expression for $w_h(f)$ in Eq. (2) yields (see Fig.
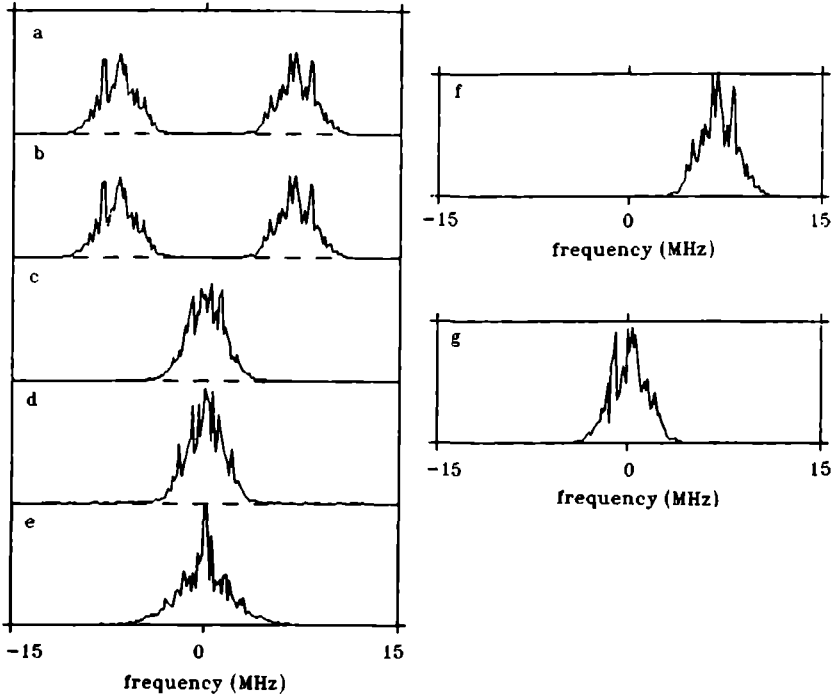
Figure 2: *a) through e) Amplitude spectra corresponding to the signals in figures 1a through 1e. f) Spectrum of preenvelope $x_p(t)$. g) Spectrum of complex envelope $\hat{x}(t)$.*

2a):

$$S_{xx}(f) = 2na^2|H(f)|^2 \tag{3}$$

where $a^2 = \langle a_m^2 \rangle_T$.

Because homogeneous scattering is assumed, the averaging in Eqs. (2) and (3) can be performed over an ensemble of signals, or over duration T of a single echo signal. The thus derived spectrum is still narrowband because only the power spectrum of the transmission pulse is present in the foregoing equations.

3 Phase derivative and its statistics

As was remarked before, $x(t)$ is a Gaussian stochastic process. Therefore, the complex envelope $\hat{x}(t)$ is a complex Gaussian variable [19, 20]. We can decompose $x(t)$ by writing:

$$x(t) = a(t) \cos \omega_c t - b(t) \sin \omega_c t \tag{4}$$

where $a(t)$ and $b(t)$ are the cosine and sine components of $x(t)$ (Fig. 1c and 1d, respectively), which can also be shown to be real Gaussian processes [18], and ω_c is the central

frequency of the narrow band signal $x(t)$. The complex envelope is defined as:

$$\hat{x}(t) = a(t) + ib(t) = e(t)\exp\{i\theta(t)\}, \tag{5}$$

(and its spectrum is shown in Fig. 2g) where

$$e(t) = |\hat{x}(t)| = \{a^2(t) + b^2(t)\}^{\frac{1}{2}} = \text{envelope (Fig. 1e)}, \tag{6}$$

$$\theta(t) = \arctan\{b(t)/a(t)\} = \text{instantaneous phase}. \tag{7}$$

The phase derivative (PD) is defined as:

$$\dot{\theta}(t) = \frac{d\theta(t)}{dt}. \tag{8}$$

The instantaneous phase of the rf echogram in figure 1a is shown in figure 1f. Note the jumping between $-\pi/2$ and $+\pi/2$ (i.e., no unwrapping applied). The PD of the rf signal in figure 1a is displayed in figure 1g. The complex envelope has a circular joint Gaussian pdf [18]

$$p_1(a, b) = (2\pi\psi)^{-1}\exp\{-[a^2(t) + b^2(t)]/2\psi\}, \tag{9}$$

where

$$\psi = \langle a^2(t) \rangle = \langle b^2(t) \rangle = \int\limits_0^\infty S_{xx}(f)df = M_0,$$

and

$$M_n = (2\pi)^n \int\limits_0^\infty S_{xx}(f)(f - f_c)^n\, df \tag{10}$$

are the central moments of the spectrum. The formulation in Eq. (9) is equivalent to a random walk in 2-D space.

In practical situations, it is more convenient to use the analytic signal (preenvelope) $x_p(t)$, rather than the complex envelope, to calculate the phase derivative [20]:

$$x_p(t) = x(t) + i\tilde{x}(t), \tag{11}$$

where

$$\tilde{x}(t) = (1/\pi)\int\limits_0^\infty \frac{x(t')}{(t - t')}dt', \tag{12}$$

is the Hilbert transform of $x(t)$ (see Fig. 1b).

Using Eq. (4), it can easily be shown that:

$$\tilde{x}(t) = a(t)\sin\omega_c t + b(t)\cos\omega_c t. \tag{13}$$

Insertion of Eqs. (4) and (13) in Eq. (11) yields the preenvelope:

$$x_p(t) = \{a(t) + ib(t)\}\exp(i\omega_c t) \tag{14}$$

$$= e(t)\exp\{i[\omega_c t + \theta(t)]\} \tag{15}$$

$$= e(t)\exp\{i\Theta(t)\}, \tag{16}$$

where $e(t)$, and $\theta(t)$ are identical to those given in Eqs. (6) and (7) and $\Theta(t)$ is the angular phase as defined in the preceeding papers [10, 11]. The spectrum of the preenvelope of the rf signal in figure 1a is shown in figure 2f.

It can be concluded from Eq. (14) that $x_p(t)$ also has a circular Gaussian pdf. When comparing Eqs. (5) and (15), it becomes immediately clear that the only difference that will occur when estimating the phase derivative from the preenvelope instead of the complex envelope will be a shift of the mean value, from zero to the central frequency $f_c = \omega_c/2\pi$. For that reason, the discussion in the following chapters applies equally well to the analytic signal method.

As was shown by Rice [21] (see also [22, 23]), the probability density functions of the parameters listed in Eqs. (6), (7) and (8) can be derived by partial integration of the joint pdf:

$$p_1(E, \dot{E}, \theta, \dot{\theta}) - E^2(4\pi^2 B) \exp\{-M_2 E^2/2B + M_0(\dot{E}^2 + E^2\dot{\theta}^2)\}, \tag{17}$$

where $B = M_0 M_2$ and in which it has been assumed that the spectrum of $x(t)$ is symmetric, hence $M_1 = 0$. It then follows that:

$$p_1(E) = E/\psi \exp\{-E^2/2\psi\} \quad \text{(Rayleigh pdf)}, \tag{18}$$

$$p_1(\theta) = 1/2\pi \quad \text{(uniform pdf)}, \tag{19}$$

$$p_1(\dot{\theta}) = \tfrac{1}{2}(M_0/M_2)^{\frac{1}{2}}(1 + M_0\dot{\theta}^2/M_2)^{-\frac{3}{2}}. \tag{20}$$

The latter equation can be further specified for a signal with a Gaussian spectrum:

$$p_1(\dot{\theta}) = 2\pi^2\sigma_f^2(4\pi^2\sigma_f^2 + \dot{\theta}^2)^{-\frac{3}{2}} \tag{21}$$

where σ_f = the standard deviation of Gaussian spectrum $(M_2 = 4\pi^2\sigma_f^2\psi)$. A plot of the pdf as given by Eq. (21) is shown in figure 3a together with a histogram of the PD obtained by simulation of an echogram [11].

As was shown by Rice [21], the mean value of $\dot{\theta}$ equals zero and its standard deviation is infinite, because the second order moment of $p_1(\dot{\theta})$ does not exist. The full-width-at-half-maximum (FWHM) of the pdf (Eq. (21)) can be calculated:

$$\text{FWHM} = 1.53\,(2\pi\sigma_f) \tag{22}$$

4 Estimation of phase derivative

When the phase derivative is estimated from the complex envelope, it is convenient to remove the extreme values (to prevent overflow of the computer), by averaging over time (smoothing). For that reason, a different approach to the phase derivative will be followed now:

$$\langle\dot{\theta}(t)\rangle = [\int\limits_0^\infty \omega S_{\hat{x}\hat{x}}(\omega)d\omega] / [\int\limits_0^\infty S_{\hat{x}\hat{x}}(\omega)d\omega] \tag{23}$$

Employing the Wiener-Kinchine relation:

$$S_{\hat{x}\hat{x}}(f) = |X_{\hat{x}\hat{x}}(f)|^2 = \int\limits_{-\infty}^\infty R_{\hat{x}\hat{x}}(\tau)\exp(-\imath\omega\tau)d\tau \tag{24}$$
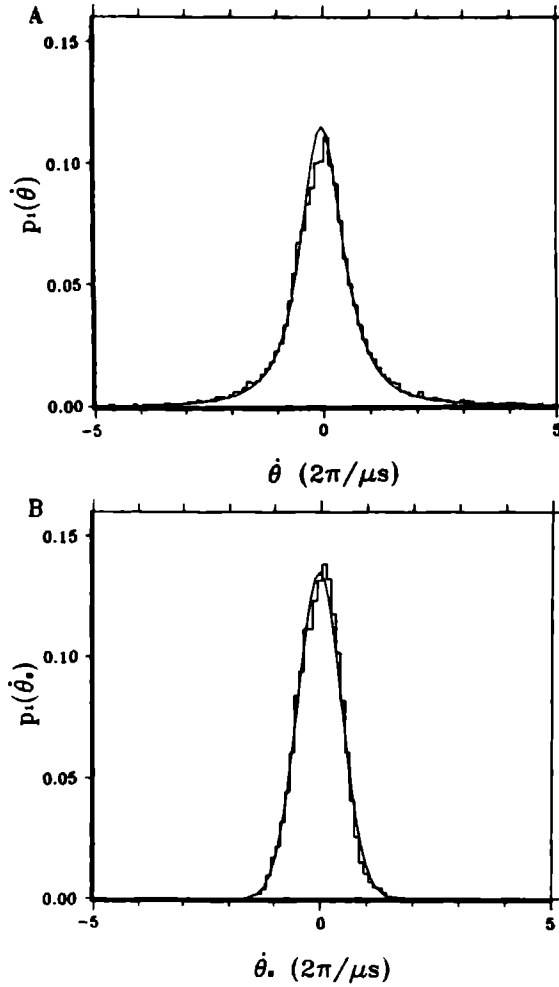
Figure 3: *a) Histogram of unsmoothed PD derived from simulated echograms* $(f_c = 5\ MHz)$. *Drawn line indicates pdf obtained with Eq. (21). b) Histogram of PD obtained by implementing a 16-point rectangular presmoothing filter (cf. Eq. (29)). Drawn line indicates best fitting Gaussian pdf.*

where $R_{\hat{x}\hat{x}}(\tau) = \langle \hat{x}^*(t)\hat{x}(t+\tau) \rangle$ is the autocorrelation function of $\hat{x}(t)$,

$\langle.\rangle$ means ensemble averaging, and

* means taking the complex conjugate.

Then with Eq. (5), it follows from this definition [19]:

$$R_{\hat{x}\hat{x}}(\tau) = R_{aa}(\tau) + R_{bb}(\tau) + i\{R_{ab}(\tau) - R_{ba}(\tau)\}. \tag{25}$$

Combining Eq. (23) and (24) yields:

$$\langle \dot{\theta}(t) \rangle = -i\dot{R}_{\hat{x}\hat{x}}(0)/R_{\hat{x}\hat{x}}(0). \tag{26}$$

Insertion of Eq. (25) yields:

$$\langle \dot{\theta}(t) \rangle = \{ \dot{R}_{ab}(0) - \dot{R}_{ba}(0) \} / \{ R_{aa}(0) + R_{bb}(0) \} \tag{27}$$

or:

$$\langle \dot{\theta}(t) \rangle = \langle \dot{b}(t)a(t) - \dot{a}(t)b(t) \rangle / \langle a^2(t) + b^2(t) \rangle \tag{28}$$

The ensemble averaging in this formula can be replaced by time averaging over a period length T because of the stationarity of the echosignal $x(t)$ (cf. [17]).

In conclusion: averaging of the numerator and denominator separately, before the division, yields an unbiased and numerically stabilized estimate of the phase derivative with a finite variance. It may be mentioned that this conclusion was reached by Angelsen [22] as well, but for the instantaneous frequency of Doppler signals (frequency modulation). The averaging over time is equivalent to increasing the number of independent observations of the instantaneous frequency that are integrated, when the duration of the integration period is increased. According to the central limit theorem, the asymptotic form of $\dot{\theta}(t)$ will therefore be a Gaussian pdf. [7]. In other words, the longer the duration of the averaging, the more the extreme values of the phase derivative will be smoothed and the variance of $\dot{\theta}$ will become finite. Therefore,

$$\langle \dot{\theta} \rangle_T = \langle \dot{b}(t)a(t) - \dot{a}(t)b(t) \rangle_T / \langle a^2(t) + b^2(t) \rangle_T, \tag{29}$$

where T = duration of time window of averaging.

The smoothed estimate of the instantaneous phase derivative $\dot{\theta}(t)$ is then:

$$\dot{\theta}_s(t) = \lim_{T \to \infty} \langle \dot{\theta} \rangle_T$$

and

$$\lim_{T \to \infty} p_1(\dot{\theta}_s) = \text{Gaussian pdf.}$$

As an example, the histogram of the PD derived by using an averaging window of 16 data points is shown in figure 3b, together with the best fitting Gaussian pdf. The same echo data were used as in figure 3a.

5 First order statistics of rectified phase derivative

It is of major interest to calculate the mean and standard deviation of the rectified derivative because this derivative is employed for the construction of echographic images. Therefore, these variables yield a concise quantification of the first order grey level statistics of these images. The rectified phase derivative is defined by:

$$\Phi = |\dot{\theta}| \tag{30}$$

and the first order pdf by

$$p_1(\Phi) = 2p_1(\dot{\theta}), \quad \Phi \in (0, \infty), \tag{31}$$

and

$$\langle \Phi \rangle = \int_0^\infty \Phi p_1(\Phi) d\Phi. \tag{32}$$

Rewriting Eq. (21) for Φ yields:

$$p_1(\Phi) = (2\pi\sigma_f)^2 \{(2\pi\sigma_f)^2 + \Phi^2\}^{-\frac{3}{2}}. \tag{33}$$

While making use of the indefinite integral [24]:

$$\int y(a^2 + y^2)^{-\frac{3}{2}} dy = -(a^2 + y^2)^{-\frac{1}{2}}, \tag{34}$$

Eq. (32) yields:

$$\langle \Phi \rangle = 2\pi\sigma_f. \tag{35}$$

In order to be able to assess the "speckle" contrast, or the inverse i.e., the signal-to-noise ratio, of an image the variance of Φ should be known as well. The second moment of Φ:

$$\langle \Phi^2 \rangle = \int_0^\infty \Phi^2 p_1(\Phi) d\Phi. \tag{36}$$

When using Eq. (33) and taking another indefinite integral from [24]:

$$\int y^2(a^2 + y^2)^{-\frac{3}{2}} dy = \ln\{y + (y^2 + a^2)^{\frac{1}{2}}\} - y(y^2 + a^2)^{-\frac{1}{2}} \tag{37}$$

it follows that:

$$\langle \Phi^2 \rangle = (2\pi\sigma_f)^2 \left[\ln\left\{ \frac{\Phi_m + ((2\pi\sigma_f)^2 + \Phi_m^2)^{\frac{1}{2}}}{2\pi\sigma_f} \right\} - \Phi_m((2\pi\sigma_f)^2 + \Phi_m^2)^{-\frac{1}{2}} \right] \tag{38}$$

In the latter equation, the upper boundary of the integral in Eq. (36) has been limited to a value Φ_m. On the one hand, this limiting is partly achieved by the integration over a certain window (Eq. (29)) and on the other hand it may still be necessary to insert a "hard" limiter in the algorithm, based on this equation, which removes the extreme values of Φ.

The results expressed in Eq. (35) and (38) are sufficient to express the SNR of the rectified PD image:

$$\text{SNR} = \langle \Phi \rangle / ((\langle \Phi^2 \rangle - \langle \Phi \rangle^2)^{\frac{1}{2}} \tag{39}$$

6 First and second order statistics of rectified and smoothed phase derivative

In this section, the first order statistics of Φ will be derived while making use of the approximate Gaussian pdf of $\dot{\theta}_s$. It can be shown [19] that the autocorrelation of a rectified Gaussian random variable equals:

$$R_{\Phi\Phi}(\tau) = 2R_{\dot{\theta}_s \dot{\theta}_s}(0)(\cos\eta + \eta\sin\eta)/\pi. \tag{40}$$

where $\eta = \arcsin\{R_{\dot{\theta}_s \dot{\theta}_s}(\tau)/R_{\dot{\theta}_s \dot{\theta}_s}(0)\}$.

Because $\dot{\theta}_s$ has a pdf which is symmetric around zero, it may be clear that $R_{\dot{\theta}_s \dot{\theta}_s}(0) = \sigma_{\dot{\theta}_s}^2$.

It can be shown [19] that for the rectified PD the mean value is given by:

$$\langle \Phi \rangle = \{2R_{\dot{\theta}_s \dot{\theta}_s}(0)/\pi\}^{\frac{1}{2}} = (2/\pi)^{\frac{1}{2}} \sigma_{\dot{\theta}_s}. \tag{41}$$

and using Eq. (40)

$$\langle \Phi^2 \rangle = R_{\Phi\Phi}(0) = R_{\dot{\theta}_s \dot{\theta}_s}(0) = \sigma^2_{\dot{\theta}_s}. \tag{42}$$

Then it follows for the "presmoothed" and rectified PD:

$$\text{SNR} = \langle \Phi \rangle/(\langle \Phi^2 \rangle - \langle \Phi \rangle^2)^{\frac{1}{2}} = \{2/(\pi - 2)\}^{\frac{1}{2}} = 1.325. \tag{43}$$

The next step in the processing is a low-pass filtering (smoothing) of the rectified PD by a 22 points cosine window function (duration $\tau_g = 4\mu s$). This filter can be characterized by its impulse response function $g(t)$:

$$g(t) = \{1 - \cos(2\pi t/\tau_g)\}/\tau_g, \quad t \in (0, \tau_g). \tag{44}$$

From this definition it follows that:

$$\int_{-\infty}^{\infty} g(t)\, dt = \int_{0}^{\tau_g} g(t)\, dt = 1. \tag{45}$$

The filtered version Φ denoted by Φ_g is the convolution of $\Phi(t)$ with $g(t)$:

$$\Phi_g(t) = \int_{-\infty}^{\infty} g(\tau)\Phi(t - \tau)\, d\tau. \tag{46}$$

Because of stationarity, it follows for the mean value (cf. Eq. (41)):

$$\langle \Phi_g \rangle = \langle \Phi \rangle \int_{0}^{\tau_g} g(\tau)\, d\tau = \langle \Phi \rangle. \tag{47}$$

$$= (2/\pi)^{\frac{1}{2}} \sigma_{\dot{\theta}_s} \tag{48}$$

The histograms of the filtered rectified PD are shown in figure 4a for a cosine filter with lengths of 10, 22 and 34 data samples, respectively. The curve marked 1 in this figure shows the histogram of the rectified PD, where the data used in figure 3 were employed again. A presmoothing was performed by using a data window of 13 samples.

Figure 4b shows the histogram in figure 4a with a cosine window length of 34 data points again, but now together with the best fitting Rayleigh pdf. It is evident that the approximation is rather good, which means that the presmoothing produces a band limited Gaussian PD to a fair approximation.

An estimate of the standard deviation of the (pre)smoothed unrectified PD, $\sigma_{\dot{\theta}_s}$, can be approximately derived from the FWHM of the pdf of the unsmoothed PD (Eq. (22)). Assuming that the smoothing operation mainly suppresses the tails of the pdf, it follows that Eq. (22) applies to the pdf of the smoothed PD as well. For a Gaussian pdf, it can easily be shown that:

$$\sigma_{\dot{\theta}_s} = 0.42\text{FWHM}_{\dot{\theta}_s}. \tag{49}$$
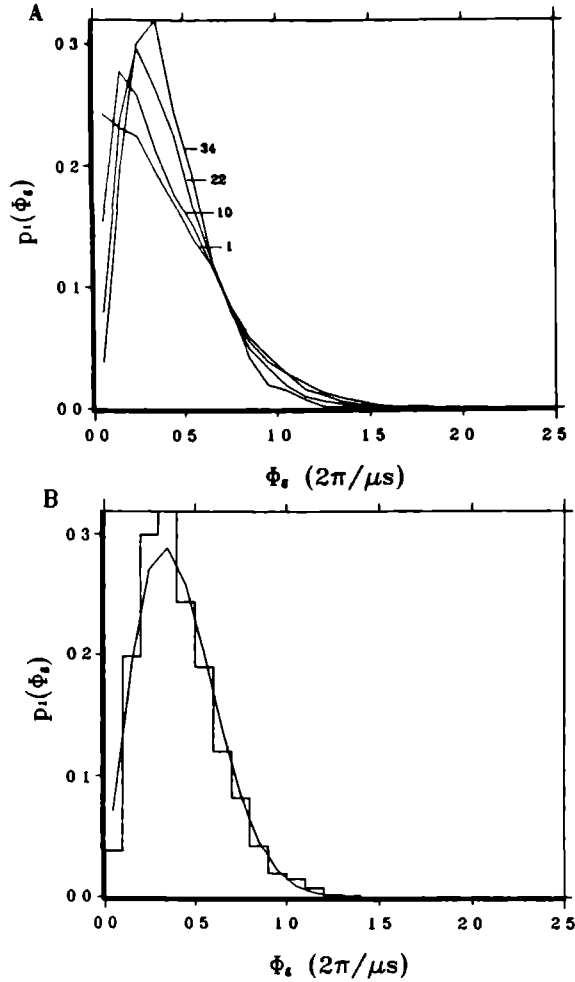
Figure 4: *a) Histograms of rectified PD obtained with a 13 point presmoothing filter and cosine filters of 1, 10, 22 and 34 data point lenghts applied after rectification. b) Histogram as in A, with 34-point cosine window and best fitting Rayleigh pdf (drawn line).*

Then with Eq. (22) it follows:

$$\sigma_{\dot{\theta}_s} \approx 4\sigma_f, \tag{50}$$

and insertion of this relation in Eq. (48) yields:

$$\langle \Phi_g \rangle = (2/\pi)^{\frac{1}{2}} 4\sigma_f \approx 3.2\sigma_f. \tag{51}$$

In order to be able to estimate the variance of Φ_g, its mean squared value has still to

be derived. Starting with the unsmoothed PD:

$$R_{\dot{\theta}_s\dot{\theta}_s}(t_1, t_2) = \int\limits_{-\infty}^{+\infty}\!\!\!\int s(\alpha)\langle\dot{\theta}(t_1 - \alpha)\dot{\theta}^*(t_2 - \beta)\rangle s^*(\beta)\,d\alpha d\beta, \tag{52}$$

where $s(t)$ is the impulse response of the presmoothing filter and assuming stationarity of the PD, i.e., $t = t_2 - t_1$, Eq. (52) can be rewritten [25]:

$$R_{\dot{\theta}_s\dot{\theta}_s}(t) = \int\limits_{-\infty}^{\infty} \rho_s(\alpha)R_{\dot{\theta}\dot{\theta}}(t - \alpha)\,d\alpha, \tag{53}$$

where

$$\rho(\alpha) = \int\limits_{-\infty}^{\infty} s(x)s^*(x + \alpha)\,d\alpha \tag{54}$$

is the autocorrelation of the impulse response of the filter.

The expression for $R_{\dot{\theta}\dot{\theta}}$ was derived by Rice [21]:

$$R_{\dot{\theta}\dot{\theta}}(\tau) = -2\pi^2\sigma_f^2\ln\{1 - \exp(-2\pi^2\sigma_f^2\tau^2)\}. \tag{55}$$

Plots of $R_{\dot{\theta}\dot{\theta}}(\tau)$ (Eq. (55)) and $R_{\dot{\theta}_s\dot{\theta}_s}(\tau)$ (Eq. (53)) are shown in figures 5a and b, curves marked "t". The curves marked "s" in these figures were obtained from the simulations. It may be mentioned that $\sigma_{\dot{\theta}_s}$ in Eq. (48) can be exactly calculated, rather than the approximation given by Eq. (50), by using Eq. (53):

$$\langle\dot{\theta}_s^2\rangle = \int\limits_{-\infty}^{\infty} \rho_s(\alpha)R_{\dot{\theta}\dot{\theta}}(-\alpha)\,d\alpha = \sigma_{\dot{\theta}_s}^2. \tag{56}$$

Inserting Eq. (53) in Eq. (40) yields the expression for $R_{\Phi\Phi}$, the autocorrelation of the rectified PD. This autocorrelation is plotted in figure 5c ("t") again with the corresponding curve obtained from the simulations ("s"). The calculations proceed then in the way as given by Eqs. (53) and (54), but now applied to the rectified PD:

$$R_{\Phi_g\Phi_g}(t) = \int\limits_{-\infty}^{\infty} \rho_g(\tau)R_{\Phi\Phi}(t - \tau)\,d\tau, \tag{57}$$

where the postrectification filter is indicated by the symbol g and $\rho_g(\tau)$ is the autocorrelation of this filter (cf. Eq. (54)). This final autocorrelation is shown in figure 5d ("t") together with the curve obtained from the simulations ("s"). Then:

$$\langle\Phi_g^2\rangle = \int\limits_{-\infty}^{\infty} \rho_g(\tau)R_{\Phi\Phi}(-\tau)\,d\tau. \tag{58}$$

Applying the Wiener-Kinchine theory, this expression can be rewritten:

$$\langle\Phi_g^2\rangle = \frac{1}{2\pi} \int\limits_{-\infty}^{\infty} |G(j\omega)|^2 W_\Phi(j\omega)\,d\omega, \tag{59}$$
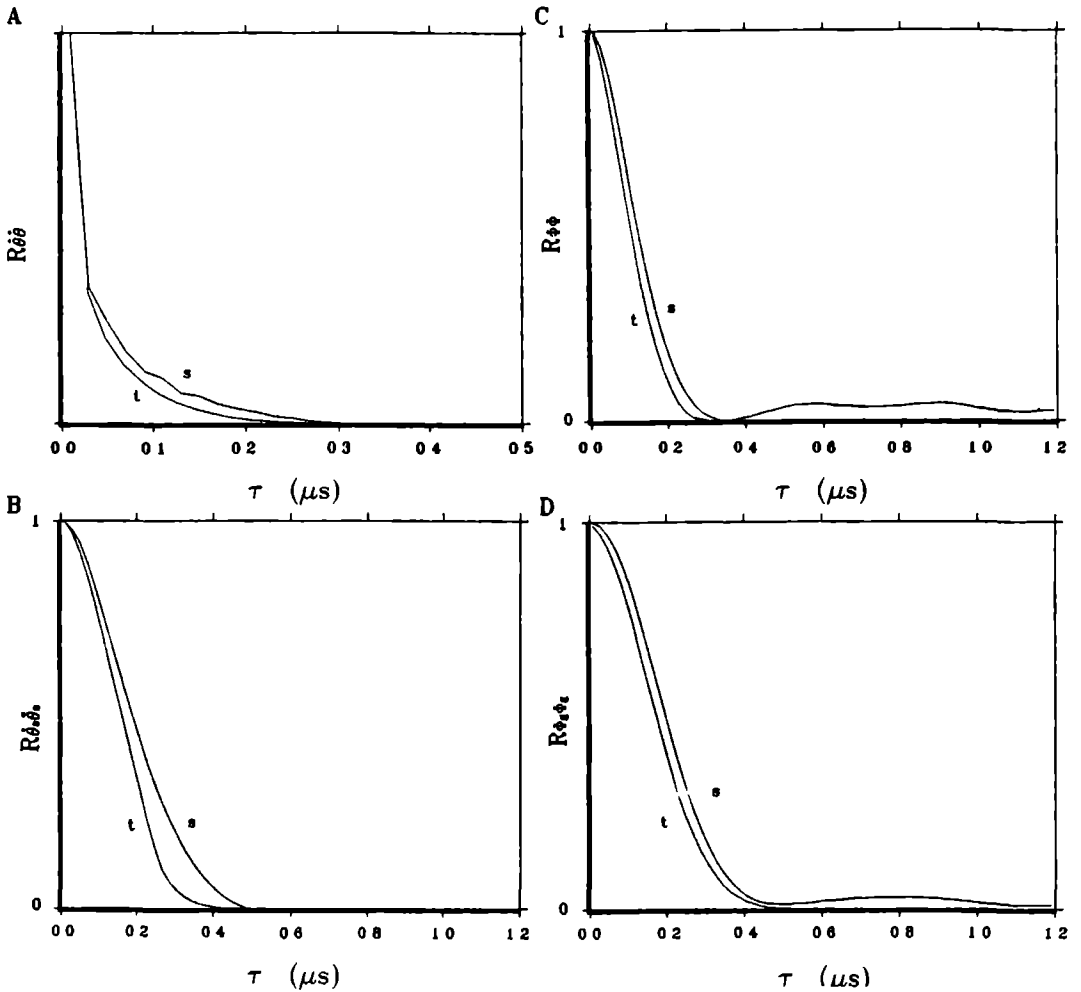
Figure 5: *a) Autocorrelation of the unsmoothed PD, t = theoretical curve (Eq. (56)), s = curve from simulations. b) Autocorrelation of the presmoothed (13 points) PD (Eq. (53)). c) Autocorrelation of the presmoothed and rectified PD (Eq. (40)). d) Autocorrelation of the presmoothed, rectified and postsmoothed (22 points) PD (Eq. (57)).*
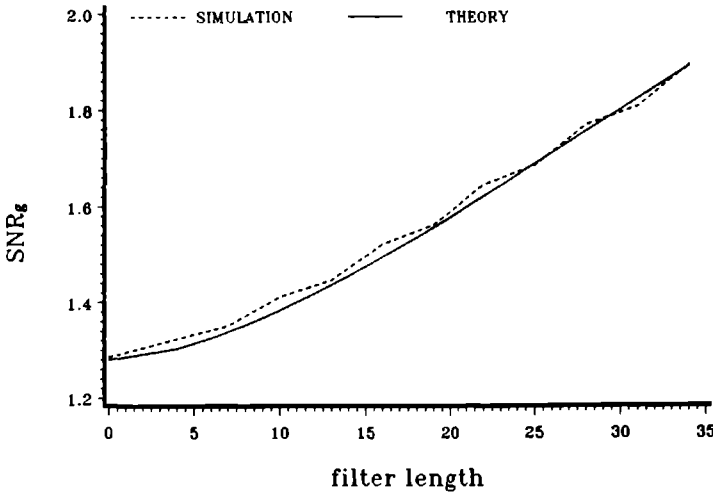
Figure 6: *Signal-to-noise ratio of presmoothed (13 points), rectified and filtered PD, SNR_g, using a cosine filter, for a range of filter lengths from 1 to 34 data points.*

where $G(j\omega)$ is the transfer function of the (post) smoothing filter,

$W_\Phi(j\omega)$ is the Fourier transform of $R_{\Phi\Phi}$.

The final SNR of the presmoothed, rectified and postfiltered PD is then obtained from Eq. (48) and (59):

$$\text{SNR}_g = \langle \Phi_g \rangle / \{ \langle \Phi_g^2 \rangle - \langle \Phi_g \rangle^2 \}^{\frac{1}{2}}. \tag{60}$$

The effects of the filtering of the rectified PD on the SNR_g are illustrated by figure 6, where the same data were employed as in the other figures. As can be seen, at filter length 0 (no filtering), the SNR approximates the value that is mentioned in Eq. (43), i.e., of the order of 1.3. Increasing the length of the filter yields a continuous increase of the SNR_g. The gradual change of the histogram to a Rayleigh pdf (Fig. 4) using the cosine windows of a length increasing from 1 to 34 data points is reflected here in the limit SNR_g of the order of 1.9. This value should be considered, however, as a relative limit, because increasing the window length would produce a further increase of SNR_g. The explanation of this phenomenon can be found in Eqs. (48) and (51) in which the mean PD appears to be independent of the filter length, whereas, it can be expected that the variance of the PD decreases with increasing window length.

It may be concluded from figure 6 that a high "point" SNR is obtained by filtering of the rectified PD. However, this implies a decrease of the axial resolution i.e., a coarsening of the PD "speckle" and, therefore, the so-called "lesion" SNR [26,27] does not change at all.

		PD		
ENV	μ	SNR	$FWHM_{az}$	$FWHM_{lat}$
μ	*	0.70	−0.62	*
SNR	*	*	*	*
$FWHM_{az}$	*	−0.69	0.73	*
$FWHM_{lat}$	*	*	*	0.48

Table 1: *Crosscorrelation coefficients of the parameters obtained from the AM image and the parameters obtained from the PD image ($p < 0.01$). $FWHM_{az}$ and $FWHM_{lat}$ are the Full Widths at Half Maximum of the 2D autocovariance function of the image in axial and lateral directions. An asterisk indicates a not significant correlation.*

7 Discussion

The stabilization of the PD by presmoothing was introduced to reduce the outliers of the derivative of the instantaneous phase. The smoothing filter of 16 samples duration is shown to yield a Gaussian pdf to a good approximation (Fig. 3b). This does not imply that the rectified PD has a Rayleigh pdf. The rectified PD instead has a pdf that is identical to a half-Gaussian if no postsmoothing is applied and this pdf approaches a Rayleigh pdf at a filter length of 34 samples (Fig. 4). This behavior is reflected in the SNR (Fig. 6) that goes from 1.3 to 1.9 when the postsmoothing filter-length is increased from 1 to 34 samples.

The theoretically derived autocorrelations of the various stages of the PD calculations are somewhat narrower than those obtained from the simulated echograms. This difference may partly be ascribed to the limited length of the presmoothing filter (13 samples), which yields a Gaussian pdf of the unrectified PD to a limited degree. Therefore, Eq. (40) holds only approximately. Furthermore, the theoretical curves were obtained by applying Eq. (53). In this equation, the autocorrelation of the instantaneous PD is low-pass filtered (i.e., smoothed). The calculation of the autocorrelation from the simulations was performed after smoothing of the PD according to Eq. (29). This was necessitated by the large PD values occuring if no smoothing was applied. The difference between the autocorrelation functions in figure 5 is well within the spread found for the series of simulations that was discussed in [11]. Nevertheless, it can be concluded, that the first and second order statistics of the PD images are now well understood. The clinical importance of these images is, however, still to be shown. An indication about this importance may be found in the correlations between parameters of the first and second order statistical characteristics of the AM (i.e., video) images and the PD images of the same data. This was investigated with the computer simulated data in figures 8 and 9 of the preceding article [11], while considering only the scatterer densities of 3000 cm^{-3} and higher, where fully developed speckle is present. The PD images produced with the SAS method, which is based on Eq. (28), were used. Table 1 shows the crosscorrelation coefficients that were significant ($p < 0.01$). It may be concluded that the mean of PD images is not correlated with AM-image parameters. However, the mean does not yield information on the scatterer density and therefore is not a likely

diagnostic parameter [11]. The other statistical parameters of PD images are highly correlated with one of those of the AM images. The conclusion drawn in [11] that the SAS method does not contribute to tissue characterization is herewith confirmed. This statement does hold, in case the scattering characteristics (size of the scatterers) remain constant. If, however, the backscatter spectrum is modified due to pathology the PD images may be advantageous as compared to AM images. This may be illustrated by the findings of Romijn [28] on the differentiation of two histologically distinguished types of intraocular melanomas. This author observed a significant contribution of the $FWHM_{ax}$ of the PD images to the discriminant function.

References

[1] Ferrari, L.A., Jones, J.P., Gonzalez, V., and Behrens, M., Acoustical imaging using the phase of echo wave forms, in *Acoustical Imaging*, Vol. 12, E.A. Ash and C.R. Hill, eds., pp. 635-641 (Plenum Press, New York, 1982).

[2] Ferrari, L.A., Jones, J.P., Gonzalez, V., and Behrens, M., Ultrasound B-mode images derived from the phase of A-line echosignals, *Ultrasonic Imaging 4*, 192 (1982) (abstract only).

[3] Ferrari, L.A., Sankar, P.V., Fink, M., Shin, S.B., and Chandler, P., Use of signal phase in medical ultrasound, *Acta Electronica 26*, 111-120 (1984).

[4] Seggie, D.A., Leeman, S., Shin, S.B., Sankar, P.V., and Ferrari, L.A., The use of phase information in ultrasound imaging; in *Ultrasonic Tissue Characterization*, Vol. 4, J.M. Thijssen and M. Smith, eds., pp. 59-66 (Fac. of Medicine Printing Office, Nijmegen, 1985).

[5] Seggie, D.A., Doherty, G.M., Leeman, S., and Ferrari, L.A., Ultrasonic imaging using the instantaneous frequency of pulse-echo signals, in *Acoustical Imaging*, Vol. 14, A.F. Berkhout, J. Ridder and L.F. van der Wal, eds., pp. 487-496 (Plenum Press, New York, 1985).

[6] Komaili, J., Sankar, P.V., Ferrari, L.A., and Leeman, S., The instantaneous frequency of a sinewave squelched bandlimited signal, *Ultrasonic Imaging 8*, 285-295 (1986).

[7] Tsao, J., Morimura, S., Itoh, H., Itoh, T., and Konishi, T., Comparisons of images derived from amplitude, mean frequency and attenuation coefficient of pulse echo signals, *Jpn. J. Med. Ultrasonics 14*, 393-406 (1987).

[8] Romijn, R.L., Oosterveld, B.J., and Thijssen, J.M., Calculation and stabilization methods of instantaneous frequency echograms, *Ultrasonic Imaging 8*, 42-43 (1986) (abstract only).

[9] Oosterveld, B.J., Romijn, R.L., and Thijssen, J.M., Diffraction analysis of instantaneous frequency (FM) images, *Ultrasonic Imaging 8*, 43 (1986) (abstract only).

[10] Romijn, R.L., Oosterveld, B.J., and Thijssen, J.M., Phase-derivative imaging I: Methods and stabilization analysis, *Ultrasonic Imaging 9*, 147-161 (1987).

[11] Oosterveld, B.J., Romijn, R.L., and Thijssen, J.M., Phase-derivative imaging II: Effects of beam diffraction and of scatterer density, *Ultrasonic Imaging 11*, 153-174 (1989).

[12] Thijssen, J.M., and Oosterveld, B.J., Texture in B-mode echograms: a simulation study of the effects of diffraction and of scatterer density on gray scale statistics, in *Acoustical Imaging*, Vol. 14, A.F. Berkhout, J. Ridder and L.F. van der Wal, eds., pp. 481-486 (Plenum Press, New York, 1985).

[13] Oosterveld, B.J., Thijssen, J.M., and Verhoef, W.A., Texture of B-mode echograms: 3-D simulations and experiments of the effects of diffraction and scatterer density, *Ultrasonic Imaging 7*, 142-160 (1985).

[14] Thijssen, J.M., and Oosterveld, B.J., Performance of echographic equipment and potential for tissue characterization, *Proc. NATO-ASI Mathematics Computer Sci. Med. Imag.*, M.A. Viergever and A. Todd-Prokopek, eds., pp. 455-468, (Springer Berlin, 1987).

[15] Thijssen, J.M., Oosterveld, B.J., and Romijn, R.L., Texture in amplitude modulated (AM) and phase-derivative (PD) echograms, *Proc. Int. Symp. Pattern Recognition Acoust. Imag.*, Vol. 768, L.A. Ferrari, ed., pp. 162-167 (SPIE, Bellingham, 1987).

[16] Requicha, A.A.G., The zeroes of entire functions: theory and engineering applications, *Proc. of the IEEE 68*, 308-328 (1974).

[17] Middleton, D., On the theory of random noise. Phenomenological models, I, II, *J. Appl. Phys. 22*, 1143-1152, 1153-1161 (1951).

[18] Middleton, D., *An Introduction to Statistical Communication Theory* (McGraw-Hill, New York, 1960).

[19] Papoulis, A., *Probability, Random variables and Stochastic Processes* (McGraw-Hill, New York, 1965).

[20] Whalen, A.D., *Detection of Signals in Noise* (Academic Press, New York, 1971).

[21] Rice, S.O., Statistical properties of a sine wave plus random noise, *Bell Syst. Techn. J. 27*, 109-157 (1948).

[22] Angelsen, B.A.J., Instantaneous frequency, mean frequency, and variance of mean frequency estimators for ultrasonic blood velocity Doppler signals, *IEEE Trans. Biomed. Eng. BME-28*, 733-741 (1981).

[23] Broman, H., The instantaneous frequency of a Gaussian signal: the one-dimensional density function, *IEEE Trans. Acoust. Speech Signal Processing ASSP-29*, 108-111 (1981).

[24] Spiegel, M.A., *Mathemathical Handbook of Formulas and Tables* (McGraw-Hill, New York, 1968).

[25] Papoulis, A., *Signal Analysis*, Chap. 9 (McGraw-Hill, New York, 1977).

[26] Wagner, R.F., and Brown, D.G., Unified SNR analysis of medical imaging systems, *Phys. Med. Biol. 30*, 489-518 (1985).

[27] Thijssen, J.M., Oosterveld, B.J., and Wagner, R.F., Gray level transforms and lesion detectability in echographic images, *Ultrasonic Imaging 10*, 171-175 (1988).

[28] Romijn, R.L., *On the quantitative analysis of Ultrasound Signals and Application to Intraocular Melanomas* (Fac. Medicine Printing Office, Nijmegen, 1990).

VI

Gray Level Transforms and Lesion Detectability in Echographic Images

J.M. Thijssen   B.J. Oosterveld   R.F. Wagner[*]

In search of the optimal display of echographic information for the detection of focal lesions, a systematic study was performed considering a wide range of gray level transforms (i.e., lookup tables). This range comprised power functions of the echo envelope signal ($1/8 \leq n \leq 8$), power functions of the logarithmic transform and a sigmoid function. The implications of the transforms on the first order statistics (histogram, "point signal-to-noise ratio" SNR_p) and on the second order statistics (autocorrelation function) could be derived both analytically, and from the analysis of simulated and experimentally obtained echograms of homogeneously scattering tissue models. These results were employed to estimate the lesion signal-to-noise ratio SNR_ℓ, which specifies the detectability of a lesion by an ideal observer. It was found, both theoretically and practically, that the intensity display corresponds to the optimal transform (i.e., $n = 2$) for a low contrast lesion. When the data were first logarithmically compressed, the lesion SNR appeared to increase with increasing power ($1/8 \leq n \leq 8$). A logarithmic transform followed by a sigmoid compression did not produce much improvement. These effects of gray level transforms on the SNR_ℓ were shown to be relatively small, with the exception of powers $n > 2$ when applied to linear (i.e., amplitude) data. In the case of high lesion contrast, the sequence of log compression, followed by a square law produced the optimum SNR_ℓ. This sequence is equivalent to the processing within echographic equipment, where the TV monitor has a gamma of the order of 2.

Key words: Acoustic speckle; B-mode echogram; gray level statistics; gray level transform; lesion detection; signal-to-noise ratio (SNR).

1   Introduction

Echographic equipment for medical diagnosis was considerably improved by the introduction of digital electronics at the end of the seventies. The scan converter memory enabled a real-time display of the echo envelope signal as gray levels in the two-dimensional B-mode echograms. Present day equipment stores the echo levels in 6 to 8 bits, i.e., 64 to 256 gray levels. The enormous range of reflectivity levels occurring in biological tissues nevertheless requires the data to be compressed before digitization takes place, whereas the attenuation within the tissues necessitates the employment of time (i.e., depth) dependent amplification. Compression of the echo levels is generally achieved

---

[*]Center for Devices and Radiological Health, FDA, Rockville, MD, USA

by a logarithmic amplifier, with a range of 80 dB or more of echo strength. The diagnostician is offered a wide variety of controls of the equipment (preprocessing) and of display facilities after an image has been digitally stored (viz., "frozen"). These so called postprocessing facilities comprise a set of lookup tables to encode the stored echo levels into gray levels at the TV monitor. The tables can often be displayed as curves and are functionally termed as: linear, high-level expand, midrange expand, etc. Since logarithmic compression is performed before storage, a linear lookup table still means a logarithmic relationship between echo strength and gray level encoding. Furthermore, the display characteristics of the TV monitor, being the last part of the imaging chain should be taken into consideration. The dependence of the gray level (i.e., luminance) of the monitor on the steering voltage is a power function. This power is generally called the gamma of the monitor and it is of the order of 2 to 3 depending on the TV standard [1].

Following the early work by Burckhardt [2], Abbott and Thurstone [3] and Bamber and Dickinson [4], the concepts of texture analysis of echograms obtained from homogeneously scattering media have recently been expanded by Wagner et al. [5] and Smith et al. [6,7]. The formalisms worked out in the field of statistical (coherent) optics [8] were rigorously applied to medical ultrasound and adequate analytic expressions for the first and second order statistics could be derived. This analysis was confined to the case of fully developed speckle, which means that the density of scattering sites within the insonified medium is high enough to approach the limit where the speckle statistics become independent of the scatterer density (with the exception of the mean echo level). The applicability of the theoretical framework to actual situations was checked with phantom studies by various authors [7,9-11]. Furthermore, the authors [10,12,13] investigated systematically the effects of lower scatterer densities and of the diffraction and focussing of the sound beam on the gray level statistics by realistic three dimensional simulations, as well as by experiments.

The work discussed so far has been concerned with what may be called the point statistics (first order gray level statistics) and the spatial statistics (second order gray level statistics) of the speckle. In a practical clinical situation, the diagnostic problem very often is to detect a focal lesion, e.g. a tumour, within an organ. This problem is termed lesion detection, therefore, and it was tackled theoretically by Smith et al. [6], fitting in the unified approach to lesion detection by Wagner and Brown [14]. These authors showed that in addition to the first order statistics (viz., point signal-to-noise ratio), the autocorrelation function, which describes the average speckle size, has to be taken into account. It is for this reason that an obvious depression of speckle contrast (enhancement of point SNR) by some processing method will not necessarily yield an improvement of the lesion detectability.

Smith et al. [15] developed a tissue phantom that can be employed for the estimation of contrast detail curves in psychophysical studies on lesion detection. They measured the relative contrast of the echo level of the lesions with respect to the background in a linear data acquisition system [15] and after photographic image registration on film [16]. Their conclusion was that a human observer behaves suboptimally with respect to an ideal observer. However, the problem of gray level encoding has not been tackled either theoretically or experimentally until recently [17] and the present paper is a full report on this subject.

2 Methods

In this paper, data were used that were obtained either by computer simulation or by scanning a tissue-like phantom. The simulations were made by employing the software package described in earlier publications [10,18,19]. This package enables us to simulate generation of the ultrasonic waveform by a transducer, propagation of the ultrasound, backscattering by a homogeneous cloud of randomly positioned scatterers, complex demodulation of rf lines and finally construction of B-mode images. The whole acoustical process is performed in three dimensional space.

The conditions of the simulations were:

Transducer: center frequency $f_c = 3.0$ MHz
bandwidth (-6 dB) $\Delta f = 0.94$ MHz (Gaussian spectrum)
diameter $2a = 19$ mm
focus at 10 cm
surface velocity weighting $(1 - (x/a)^4)$
Tissue: velocity 1500 m/s, no attenuation
density of scatterers: 10^4 cm^{-3}.
B-mode area: centered around the focus, depth 1 cm, width 2 cm.

The simulations were repeated twenty times, with independently generated "tissues". Ten scans served then as the "background". The remaining ten which were multiplied by a factor of 1.3, and of 3.0, representing the low contrast and the high contrast case respectively, served as the "lesion". Note that this way of obtaining lesion data is allowed because acoustical speckle noise is multiplicative and has a Rayleigh distribution, for which the standard deviation is proportional to the mean amplitude.

The experiments were performed by using the online data acquisition and processing equipment developed at our laboratory, which was described in its preliminary version [20], but which has been recently expanded by incorporating an array processor (VAP64B, DSP Inc.). This system was interfaced to an abdominal scanner (Sonoline 3000, Siemens Inc.) with the transducer characteristics of $f_c = 3.0$ MHz, bandwidth (-6 dB), $\Delta f = 0.94$ MHz, diameter $2a = 19$ mm and focus at 7.5 cm. After a linear amplification, the rf data and the TGC driving voltage were digitized at 12 MHz in 8 bits by a transient recorder (BE 256, Bakker Electronics). The experiments were performed with a commercial version of the tissue-like phantom developed by Smith et al. [15] (Nuclear Associates, Inc.). The frequency dependent attenuation was estimated after appropriate TGC compensation and diffraction correction [19,21,22]. Twenty scans were acquired from different sites of the phantom. Ten of the scans were multiplied by a factor of 1.3 and of 3.0. These sets served as the lesions as before with the simulations.

All these data were processed with a complex demodulation algorithm, thus yielding the envelope signals for the video B-mode echograms. The final step in the signal processing was the processing of the echo amplitudes by nonlinear transformations to encode the final gray levels (Fig. 1):

power function: V^n $(1/8 \leq n \leq 8)$,
log-power function: $\{\log(1 + V)\}^n$ $(1/8 \leq n \leq 8)$,
log-sigmoid function: $\arctan[\log(1 + V) - 1] + \pi/2$.
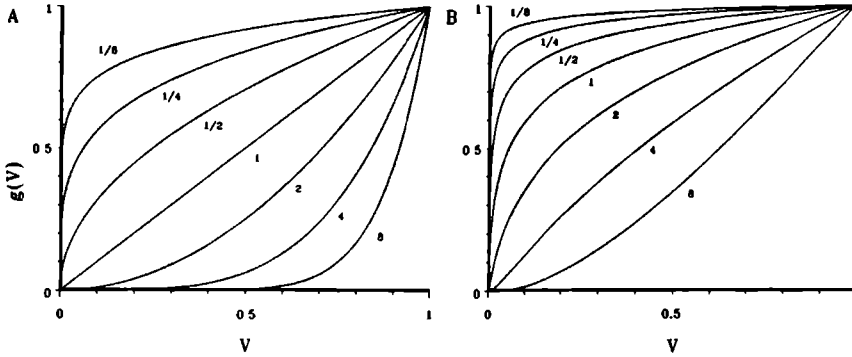
Figure 1: *Gray-level transforms versus gray level V. Both axes were normalized to the maximum values. a) Power law transforms, V^n, with powers n ranging from 1/8 to 8 indicated along the lines. b) Power law transforms of logarithmically compressed data, $[\log(1 + V)]^n$.*

In order to prevent overflow problems with low values of the variable V, the logarithm of $(1 + V)$ was considered. This induces no serious limitation because in practice the 6 to 8 bits grey level storage yields a range from 0 to 63, or 0 to 255 of the variable V.

The implications of these gray level transforms for first and second order gray level statistics are theoretically derived in appendices A and B.

3   Results

3.1   First order statistics

The effects of the various transforms on the grey level histogram were investigated by using the simulated data. Figure 2a shows these histograms for the power law transforms, together with the probability density functions (pdf) as given by:

$$f(V') = \frac{V'^{\frac{1-n}{n}}}{n\sigma^2} \exp\left\{\frac{-V'^{\frac{2}{n}}}{2\sigma^2}\right\} \tag{1}$$

where $V' = V^n = g(V)$ as derived in Appendix B (Eq. (B4)). The histogram shown for $n = 1$ runs from grey level 0 to 127, and corresponds to a Rayleigh pdf with $\mu_V = 39$ and $\mu_V = 20.4$.

The consequences of a logarithmic compression prior to the power law transform are shown in figure 2b. By this compression, the pdf's are deformed towards the higher gray levels, and are given by (cf. Eq. (B12)):

$$f(V') \approx \frac{V'^{\frac{1-n}{n}}}{n\sigma^2} e^{-2V'^{\frac{1}{n}}} \exp\left\{\frac{-e^{2V'^{\frac{1}{n}}}}{2\sigma^2}\right\}, \tag{2}$$

where $V' = \{\ln(1 + V)\}^n = g(V)$.
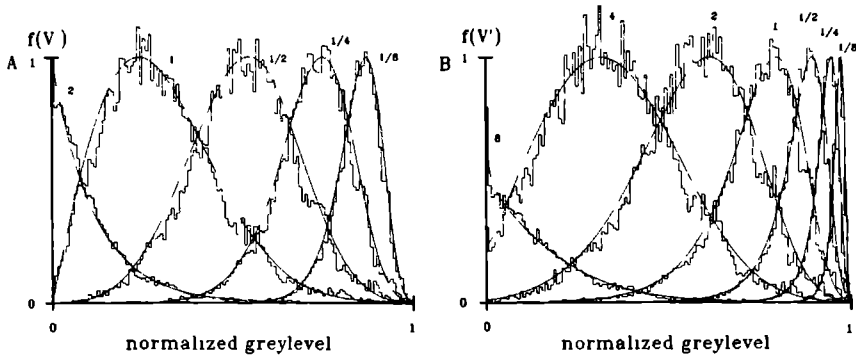
Figure 2: *Theoretical pdf's (continuous lines) and gray level histograms estimated from simulated B-mode data. To facilitate the display, the pdf's were normalized to their maximum values. a) Power law transforms. b) Power law transforms of log compressed data.*

Figures 2a and 2b show that the theoretically derived pdf's yield an adequate fit to the histograms of the (simulated) B-mode data. A summarizing parameter of the histograms is the point signal-to-noise ratio, SNR_p as defined by:

$$SNR_p = \frac{\mu_{V'}}{\sigma_{V'}} \tag{3}$$

The SNR_p was estimated from the histograms obtained for the simulated images (Fig. 3a) and for the images measured from the tissue mimicking phantom (Fig. 3b). The data points in these figures show the mean values obtained from ten independent images, either simulated or measured. The standard error of the mean is indicated by vertical bars which are visible only at low values of the powers. It is obvious that both figures show a rather large range of SNR_p values over the range of powers involved. The final point of the log-compressed data, indicated by LSC, stands for S-shaped compression after the log compression, which is described by the arctangent of the log data. The SNR_p for LSC might be calculated by the approximate formulas given in Appendix B (Eqs. (B24) and (B20b)).

It can be concluded that the results of the experiments are practically identical to those obtained by the simulations. Therefore, the conclusion can be drawn that the log compression increases the SNR_p by a factor of four approximately, independently of the power n (dashed lines vs. solid lines in figure 3). This result can be stated also as a decrease of the speckle contrast by a factor of four, due to log compression.

The question might be asked as to whether these results are in agreement with the exact analytical formulas. The SNR_p in case of a power law transform has been derived in the Appendix (Eq. B8):

$$SNR_p = \Gamma(n/2 + 1)[\Gamma(n + 1) - \Gamma^2(n/2 + 1)]^{-\frac{1}{2}}. \tag{4}$$

In order to facilitate the comparison the simulated data (Fig. 3a) were reproduced in
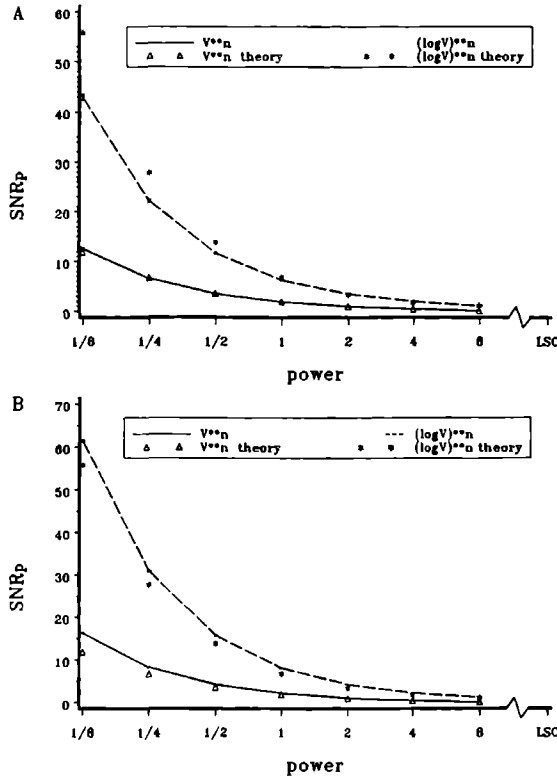
Figure 3: *Point signal-to-noise ratio, SNR, versus logarithmic magnitude of the power of the transform. Error bars indicate one standard error of the mean (10 realizations). LSC indicates the sigmoid compression curve (arctan of log-compressed data). a) Simulated data. b) Data measured from tissue mimicking phantom. Triangles: values calculated using equation (4). Asterisks: values calculated using equation (5).*

a plot with a logarithmic ordinate (Fig. 4). The data calculated by equation (4) are depicted as triangles. It can be concluded that these theoretical data correspond rather well with the data from the simulations. The formula to calculate the SNR_p of the power law transforms of the log-compressed data is an approximation, as is derived in Appendix B (Eq. (B18)):

$$ SNR_p \approx \frac{\mu_V}{\sigma_V} \frac{\ln(1 + \mu_V)}{n} + \frac{\sigma_V}{2\mu_V} \left\{ \frac{n-1}{\ln(1 + \mu_V)} - 1 \right\}. \tag{5} $$

The results obtained by this formula, with $\mu_V = 39$ and $\sigma_V = 20.4$, are shown in figure 4 by the asterisks. The correspondence of the points with the data from the simulations is almost exact at $n = 1$, but less for other values of the power n.
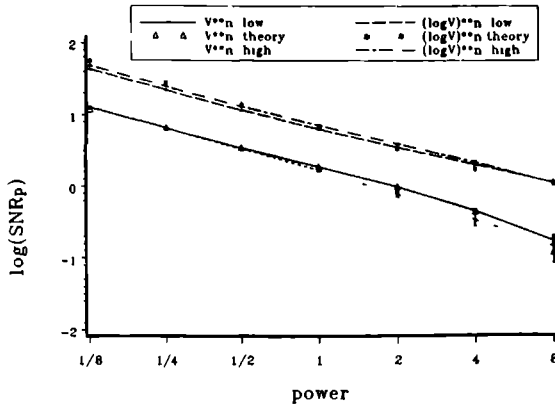
Figure 4: *Double-log plot of data in figure 3a. Also shown are the results for the large contrast case (Eq (7)).*

Since the noise of the image speckle is essentially multiplicative, one should consider the effect of a large contrast in case of lesion detection. As is derived in Appendix A, the so-called lesion signal-to-noise-ratio, SNR_ℓ, in this situation, equals (Eq. (A16)).

$$SNR_\ell = C_\ell SNR_p^* M^{\frac{1}{2}}, \tag{6}$$

where $C_\ell = 2\dfrac{\langle g(V_2)\rangle - \langle g(V_1)\rangle}{\langle g(V_2)\rangle + \langle g(V_1)\rangle}$, the lesion contrast,

M = the number of speckle cells within the area of the lesion

and

$$SNR_p^* = \frac{1}{2}\frac{\langle g(V_2)\rangle + \langle g(V_1)\rangle}{\sqrt{\sigma_{1,p}^2 + \sigma_{1,p}^2}}, \tag{7}$$

the subscripts indicating the background (1) or the lesion (2). The SNR_p^* was calculated as before from the simulated and measured B-mode images, but now for two sets of ten images with a contrast $C_\ell = 1$ $(n = 1)$. The ensemble averages and variances, after nonlinear processing, were then calculated.

The formula to calculate the SNR_p^* (Eq. (7)) was modified by a multiplicative factor of $\sqrt{2}$ in order to facilitate a comparison with the SNR_p data obtained by equation (3). Only values thus calculated from the simulations are displayed in figure 4. It can be concluded that this "large-contrast" case yields a progressively different SNR_p^* as compared to the original SNR_p with increasing value of the power for the power law compression. The log-compressed data, however, display an increased SNR_p^* as compared to the original one (i.e., low contrast SNR_p). This difference can be described by a constant factor of 12 percent for powers in the range $1/8 \leq n \leq 2$. At still higher powers, the difference decreases and even reverses.

3.2   Second order statistics

The second order statistics were characterized by the autocorrelation function (ACF). The general expression for the ACF is (cf. Eq. (B26)):

$$E\{g(V(x))g(V(x')); \Delta x\} =$$
$$\iint_{-\infty}^{\infty} g(V(x))g(V(x'))f_2(V(x), V(x'); \Delta x)dV(x)dV(x'), \qquad (8)$$

where $V(x)$ and $V(x')$ are echo levels at positions x and x',

$\Delta x = x' - x$,

$f_2(.)$ = joint pdf (see Eq. (A6)).

Equation (8) can be analytically derived in case of a single power law (cf. Eq. (B27)), but not for the log-compressed data. The autocovariance function ACVF, rather than the ACF, was calculated. The ACVF is defined as the centralized ACF, which means that the square of expectation value $E\{g(V(x))\} = \langle g(V(x))\rangle$ has to be subtracted from the right hand integral in equation (8). The impulse response of the echographic system was assumed to yield a Gaussian shape of the envelope signal V. The ACVF calculated using equation (B27) for the range of powers $1/4 \leq n \leq 4$ is shown in figure 5a. The curves display a maximum width of the ACVF at $n = 2$ and a Gaussian shape for $n = 1$ and $n = 2$ (rigorously for $n = 2$).

A further step is to compare these curves with the ACVF obtained from simulations and experiments. A set of ten images of both kinds was processed and the average ACVF was estimated after the various gray level transforms using the unbiased estimate. The results for the simulated images are shown in figure 5b, after normalization of the ACVF to the value at zero lag distance. It is clear that the curves do cross the zero line, which is due to the random character of the speckle in B-mode images, the discrete processing and the finite record length (of rf lines). The effect of the various powers can be summarized as follows: the widest ACVF occurs for $n = 2$ and lower and higher powers produce curves which become gradually narrower. In the lateral direction similar curves were obtained, which is not shown here. The ACVF's obtained after log compression and power law continuously become narrower when the power goes down from $n = 8$ to $n = 1/8$, as can be seen in figure 5c.

To quantify these results, we estimated the area under the ACVF until the first zero crossing as a representation for the average speckle cell size. This was done both for the simulated and experimental images and now also in the lateral direction. The results obtained for the simulated images are shown in figures 6a and 6b. The standard error of the mean is indicated by the vertical bars. Apart from a factor of four difference, the axial and lateral size of the ACVF's display a quite similar dependence on the power. The sigmoid compression produces a width of the ACVF which is almost identical to the one for $n = 4$.

The area under the axial ACVF's, calculated using equation (9) and displayed in figure 5a, was estimated by integrating over a large range of the lag. The results are shown as the triangles in figure 6a. Since these ACVF's have a larger width and a smooth tail towards higher lags the areas are larger than of the simulated (Figs. 5b and 5c) and experimental data. As can be seen in figure 6a, the differences are almost constant and the maximum for the triangles is also found at $n = 2$.
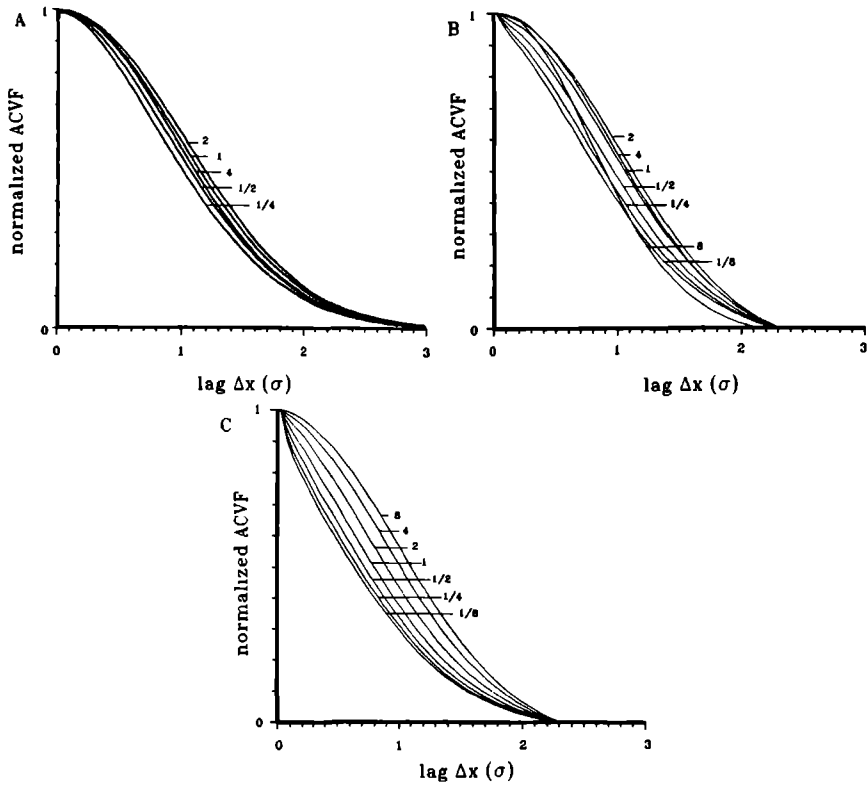
Figure 5: *Autocovariance function (ACVF) of B-mode texture speckle (axial direction) vs. lag as a function of the power of the transform. a) Results of analytical calculations ($1/4 \leq n \leq 2$). b) Results calculated from simulated images (linear). c) Results calculated from log-compressed images as in b).*

The area of the normalized axial and lateral ACVF's calculated for the experiments are shown in figures 7a and 7b. The main difference with the simulated data is the steep decrease of the area for the power law transform at $n = 4$ and $n = 8$. However, the maximum is still obtained at $n = 2$. The values calculated from the power law transform of log compressed data show again the continuous increase with increasing power, and the sigmoid compression (LSC) again produces a result which is almost equal to that at $n = 4$.

3.3   Lesion signal-to-noise ratio

The ingredients to estimate the lesion signal-to-noise ratio (SNR_ℓ) have been discussed now. With reference to equation (6), the procedure was as follows:

a. Estimation of the lesion contrast, C_ℓ. The demodulated B-mode images (both simulated and measured) were split in two series of ten images. The A-lines of one series
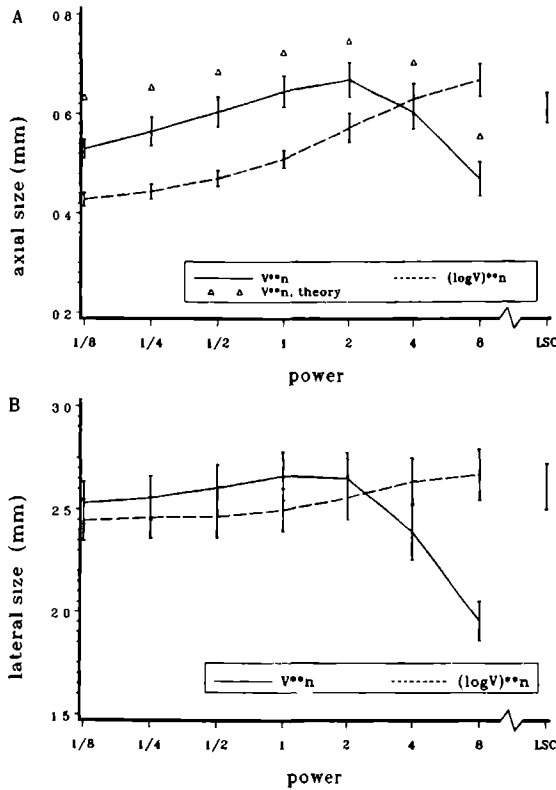
Figure 6: *Speckle size, estimated by the area under the ACVF of the simulated B-mode echograms versus magnitude of the power of the transform. a) Axial direction; triangles indicate values calculated using equation (B27). b) Lateral direction.*

were then multiplied by a factor of 1.3, which will be discussed as the small contrast case, and by a factor of 3, which is called the large contrast case. This rescaling of speckle data is allowed and meaningfull because for Rayleigh statistics mean and standard deviation are proportional. Therefore rescaling is equivalent to simulating or measuring a tissue with a different reflectivity. These images served as the "lesion". By using the definition given with equation (6) the lesion contrast C_l will then on the average be 0.26 and 1.0, respectively, for $n = 1$.

b. Estimation of the large contrast point signal-to-noise ratio, SNR_p^*. The procedure to estimate SNR_p^* has been described in the foregoing, and the results are shown in figure 4.

c. Estimation of the effective number of speckles, M. According to the definition as given in Appendix A (Eq. (A18)) the value of M equals the ratio of the lesion area A_l and the speckle size A_c. Following Wagner et al. [5], the size is taken as the geometric
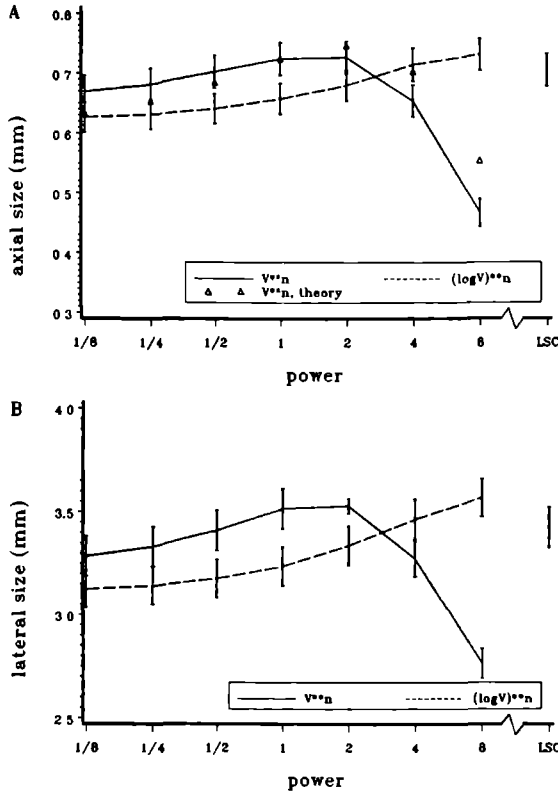
Figure 7: *Same as in figure 6, but now for data measured from tissue-mimicking phantom.*

mean of the areas under the normalized ACVF in the axial and lateral directions (cf. Figs. 6 and 7 for simulated and measured echograms, respectively).

The results of this procedure when applied to the simulated data in the low contrast case are shown in figure 8. Due to the accumulation of estimation errors the vertical bars, displaying the standard error of the mean values, are rather large. The trend of the mean values for the power law transforms, however, still indicates a maximum of the SNR_ℓ at $n = 2$. The results of the log-compressed data are less consistent, although a tendency exists for a continuous increase with increasing powers. It may also be obvious that the sigmoid compression does not differ significantly from the SNR_ℓ values of the log compression followed by a power law.

The results obtained by using the same simulated images, but now with the large contrast, are shown in figure 9. The solid line corresponds again to the power law transform and displays a dependency of SNR_ℓ on the power which is rather different from the previous figure. The maximum SNR_ℓ is found at $n = 1/2$. The log-compressed data in figure 9 also show the tendency to decrease at larger powers. The maximum
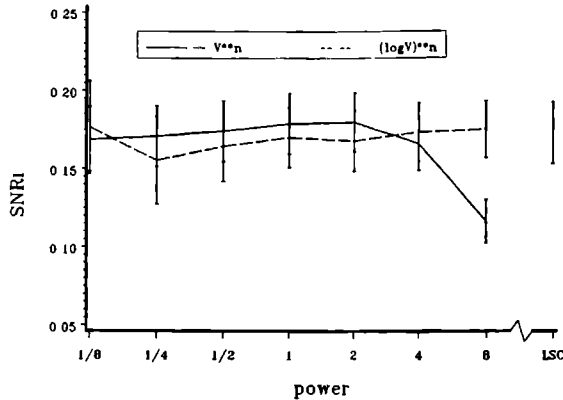
Figure 8: *Lesion signal-to-noise ratio vs. magnitude of power law transform of simulated echograms, small contrast case ($C_\ell = 0.26$).*

SNR_ℓ is, however, found at $n = 1$, which implies that a simple logarithmic compression yields a lesion detectability that is similar to the $n = 1/4$ of the power law compression for the large contrast case. The sigmoid compression LSC also yields a SNR_ℓ of almost the same magnitude. Comparison of figures 8 and 9 allows for the conclusion that for contrasts between 0.26 and 1 (i.e., $V_2 = 1.3V_1$, and $V_2 = 3V_1$), the optimal power will be of the order of $n = 1/2$ to $n = 2$ and the optimal power after log compression of the order of $n = 2$.

The great difference between the power law compressed data in figure 9 as compared to those in figure 8 needs an explanation. For that purpose, we have to consider the
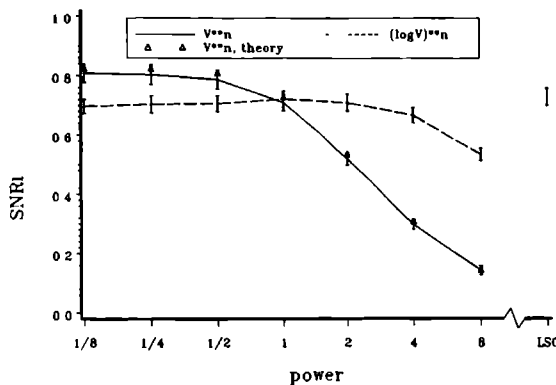
Figure 9: *Same as in figure 8, large contrast case ($C_\ell = 1$). Triangles indicate values calculated from the small contrast case using equation (11).*

definition of SNR_ℓ as given in equation (6), (see also Eq. (A16) of Appendix A):

$$SNR_\ell = \frac{\langle g(V_2)\rangle - \langle g(V_1)\rangle}{\sqrt{(\sigma_{2,p}^2 + \sigma_{1,p}^2)A_\ell^{-1}A_c}}. \tag{9}$$

Rewriting this equation for a power law in which $V_2 = cV_1$, yields:

$$SNR_\ell = \frac{(c^n - 1)\langle g(V_1)\rangle}{(c^{2n} + 1)\sigma_p^2 A_\ell^{-1}A_c}. \tag{10}$$

$$SNR_\ell = \frac{c^n - 1}{\sqrt{c^{2n} + 1}}SNR_p M^{\frac{1}{2}} \tag{11}$$

Therefore, the variation of SNR_ℓ with the power n can be described by a simple multiplicative factor. This factor was calculated as a function of n for both contrast values and the ratio of these factors was then employed to calculate the large contrast SNR_ℓ (Fig. 9) form the data at the low contrasts (Fig. 8). The SNR_ℓ values thus obtained are indicated in figure 9 by the triangles. It can be concluded that the strong decrease at $n = 2$ and $n = 4$ is fully explained.

3.4   Processing of images containing lesions

The effects of the nonlinear processing of the grey scale cannot easily be demonstrated in images. First of all, many nonlinear compression steps are involved in normal echographic equipment. This is partly avoided in the present paper because both the simulations and the experimental data were obtained after linear processing. The second problem is connected to the highly nonlinear gamma ($2 \leq \gamma \leq 3$) of TV monitors and the additional gamma of the photographic documentation. Finally, there is the problem of the enormous expansion of the dynamic range by the power law if $n > 2$. This latter problem was solved by clipping the transformed data at the median plus and minus two-times the standard deviation of the gray level histograms. The range thus obtained was expanded over the full 64 gray levels of the display system and lower and higher gray levels were clipped at zero and 63, respectively. The data were obtained by scanning various cones within the tissue phantom developed by Smith et al. [6] and are shown in figure 10 (power law) and figure 11 (log compression and power law). The contrasts of the four cones that are visible are given by the manufacturers as the reflectivity ratio (i.e., at $n = 1$), which ranges from: -7.0, -3.4, 3.6 to 7.1 dB. When comparing these images, the effects corresponding to the observation made in figure 9 for large contrasts are not at all obvious. The power law transformed images (Fig. 10) display an improvement of the detectability that is due to the clipping at low and at high gray levels ($n \geq 2$). The images after log compression are much more suited to a display over a limited dynamic range. The effects of clipping become involved only at $n = 8$. The log compressed images have a "familiar" appearance ($n \geq 2$), which confirms the involvement of these nonlinear processing cascades in echographic equipment. The sigmoid compression produces images which are in between $n = 2$ and $n = 4$ in figure 11. This observation is of course partly dependent on the actual parameters in the employed arctangent function (Eqs. (B22) and (B24)).
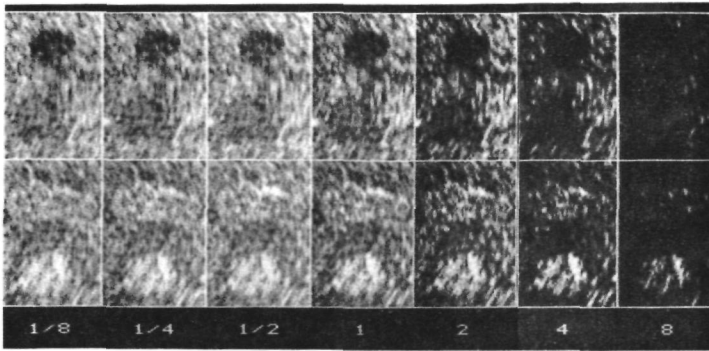
Figure 10: *Two rows of sector scans of tissue mimicking phantom containing cones of varying contrast (from top to botom: -7.0, -3.4, +3.6, +7.1 dB, respectively), power law transform of linear data, from left to right $1/8 \leq n \leq 8$.*

4   Discussion

The first order gray level statistics have been characterized by the histograms of simulated B-mode echograms and by the point signal-to-noise ratio SNR_p of simulations and phantom measurements. The histograms obtained from the phantoms did not differ much from those of the simulations as can be decided from the correspondence between figures 3b and 3a. The general conclusion can be drawn then that it has been proven that both for the power law transforms, and for the log-compressed power law trans-
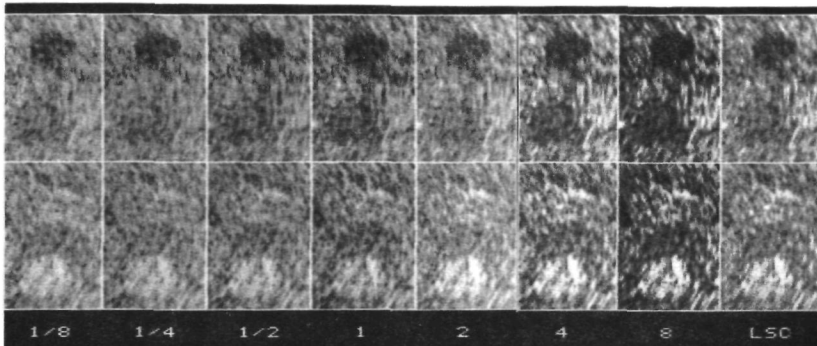
Figure 11: *Same as in figure 10 for power law transforms of log-compressed data.*

forms, the SNR_p decreases monotonically with increasing power over the whole range involved ($1/8 \leq n \leq 8$).

The decrease is linear on a log-log plot and the SNR_p of log compressed data is approximately a factor four higher over the whole range of powers. The speckle contrast, which is the inverse of the SNR_p, can be stated to increase similarly over the whole range. The effects of a high contrast on the SNR_p could be adequately predicted from the derived analytic formulas of the pdf's, although the approximation made for the log compressed data yielded a discrepancy at the extreme powers.

The enormous range of SNR_p values over the range of powers involved in this study (Figs. 3 and 4) is not reflected in the lesion signal-to-noise ratio SNR_l (Figs. 8 and 9). It should be stressed therefore, that the SNR_p is not an adequate measure of the speckle statistics to assess the dectectability of a lesion. The second order statistics have been characterized by the area under the ACVF over the range of lags from zero to the first zero-crossing of the curves. It should be emphasized that the axial ACVF of an echogram obtained with a Gaussian transmission pulse is also a Gaussian function. Therefore, theoretically, no zero crossings do occur (Fig. 5a). In practice, i.e., by analyzing either the simulations or experimental data, the ACVF has an oscillatory tail, which is caused by several reasons (see also Section 3.2): the random nature of speckle (interference), the discrete processing of the rf data and the finite length of the rf lines.

In other publications, another characteristic of the ACVF is often used to quantify the size, the full-width-at-half-maximum, FWHM. It was shown by Smith and Wagner [7] that the theoretical relation between the area and the FWHM was actually present in phantom measurements. We have found a similar result for the linearly processed data. Because of the considerable deformations of the shape of the ACVF by the highly nonlinear processing considered in this paper, we decided to employ an area measure. It appeared that the area until the first zero crossing produced the most consistent results.

The application of this latter measure to the lateral ACVF can be motivated by the same arguments as before. In addition, even with short duration pulses, the lateral beam profile of circular transducers displays some, albeit small, side lobes [18]. This diffraction effect, caused by the limited aperture of the transducer, enhances the oscillatory behavior of the lateral ACVF. The philosophy of employing two ACVF's to characterize the average speckle size is the observation that in the focal zone the wavefront is flat, to a fair approximation, and therefore the axial and lateral ACVF's are independent [5]. The power law transforms yielded a maximum size of both ACVF's at $n = 2$. This result implies that the effective number of speckles within a lesion (i.e., M in Eq. (11)) is minimum for $n = 2$. The log-compressed data, on the other hand, yielded a continuous increase of the ACVF in both axial and lateral directions until the highest power $n = 8$. These observations were made for the simulations as well as for the experiments (Figs. 6 and 7), but are not intuitively clear. Moreover, the log-compressed data yielded ACVF sizes significantly smaller than the power law data ($< 25\%$), which indicates an advantage of the former for obtaining a high SNR_l (Eq. (11)).

The lesion signal-to-noise ratio, SNR_l, for the power law transforms in the small contrast case (Fig. 8) could be shown to be maximum at $n = 2$, which is in accordance with theory [6]. The differences of the SNR_l's at the various powers are small compared to the differences of the SNR_l's in the high contrast case (Fig. 9). The explanation for this phenomenon, as given by equation (10), can also be extrapolated to even lower

contrasts than considered in the previous sections. The contrast factor of equation (11), $(c^n - 1)/\sqrt{c^{2n} + 1}$, can be shown to display almost a proportionality to the power n if c goes to one. Since the SNR_p is to a good approximation inversely proportional to the power n (Fig. 4), the SNR_ℓ tends to become independent of n for very low contrasts.

The speckle signal-to-noise ratio integrated with a finite aperture, in the case of log-compressed data and a power $n = 1$, was discussed in [23] and mentioned in Appendix B (Eq. (B28)). The value of M used by Arsenault and April was termed in [23] "the effective number of speckles in the integrating aperture". These authors considered the intensity rather than the envelope (or magnitude) V and took M to be independent of the log compression. We have shown that the ACVF changes by log compression with approximately 25 percent. Therefore, their signal-to-noise ratio is not equivalent to the lesion signal-to-noise ratio as defined in this paper. Apart from this slight but significant difference, our results confirm the additivity of the speckle noise in case of the simple log compression in [23].

The sigmoid compression following log compression (LSC) yielded a SNR_ℓ value in the range found for the other log compressions followed by a power law in the low contrast case (Fig. 8). For the high contrast case, the SNR_ℓ almost equaled those found for the log compression followed by a power of the order of 1 to 4. It can be concluded, therefore, that for lesion detection, this form of compression (i.e., lookup table) does not yield a significant advantage over a log compression followed by a power law. Nevertheless, the LSC might be preferred for keeping some distinction between the relatively strongly reflecting structures which outline the anatomy of the examined organs.

The findings at high contrast (Fig. 9) have to be discussed also while considering the so-called "gamma" of TV monitors. According to the CCIR standard [1], the gamma of monitors is 2.8 (PAL standard), and 2.2 (NTSC standard). Because the log compression followed by a power of the order of 2 yields the maximum SNR_ℓ (Fig. 9) it can be concluded that the log compression, a linear lookup table and a standard TV monitor represents the optimum sequence for lesion detection in a speckle image. This sequence appears to be implemented in echographic instruments for practical reasons (limited amplitude range of analog-to-digital converters). As an alternative also, the sigmoid lookup table can be recommended. Other, even "personal", lookup tables (post-processing curves) are not well suited for improving lesion detection in organs.

Appendix A

A Gray Level Statistics of Linearly Processed Echo Data

A.1 First order statistics

When considering the echographic signals as a random phasor, the distribution functions of the envelope and phase have been derived in a number of places [8,24-26]. The basic assumption is that the number of scatterers contributing to the rf echo signal $a(t)$ at every moment (i.e., depth) is large enough to obtain a normal (Gaussian) probability density function (pdf), which is circular for the analytic signal. The phase has a uniform pdf [25]. The pdf of the envelope $V = \sqrt{a_r^2 + a_i^2}$ is the well-known Rayleigh distribution:

$$f(V) = -\frac{V}{\sigma^2} \exp\left\{-\frac{V^2}{2\sigma^2}\right\}, \qquad (A1)$$

where σ^2 = variance of the Gaussian pdf.

The mean and standard deviation, i.e., the first two (central) moments of this distribution, are easily derived:

$$\mu_V = \sigma\sqrt{\frac{\pi}{2}}, \qquad (A2)$$

$$\sigma_V = \sigma\sqrt{\frac{2 - \pi}{2}}. \qquad (A3)$$

Hence, the signal to noise ratio (SNR) at any point in the image becomes:

$$\text{SNR}_p = \frac{\mu_V}{\sigma_V} = 1.91. \qquad (A4)$$

It may be mentioned that the complex rf amplitude $a(t)$ results from a convolution of the point spread function of the transducer and the scatterers in the medium. For a homogeneous and randomly distributed cloud of point scatterers, this convolution is simply a product of the reflectivity and the point spread function at the position of each scatterer [5].

A.2 Second order statistics

The second order statistics are characterized by the autocorrelation function (ACF), or the autocovariance function (ACVF, viz., the centralized ACF) [5,10,24].

$$E\{V(x)V(x'); \Delta x\} = \iint\limits_{-\infty}^{\infty} V(x)V(x')f_2(V(x), V(x'); \Delta x)dV(x)dV(x'), \qquad (A5)$$

where $\Delta x = x' - x$.

The analytic expression of the joint pdf is given by [24]:

$$f_2(V(x), V(x'); \Delta x) = \frac{V(x)V(x')}{\sigma^4(1 - k_0^2)} \exp\left(-\frac{V(x)^2 + V(x')^2}{2\sigma^2(1 - k_0^2)}\right) I_0\left(\frac{k_0 V(x)V(x')}{\sigma^2(1 - k_0^2)}\right), \qquad (A6)$$

where I_0 = modified Bessel function of zero order and first kind,
  k_0 = complex coherence factor = $\langle a(x)^* a(x')\rangle / 2\sigma^2$.

A.3   Lesion signal-to-noise ratio

An important concept in medical imaging is the lesion signal-to-noise ratio, SNR_ℓ, because it yields an objective and quantitative means to assess the quality of the imaging system [6,14]. The SNR_ℓ applies to the problem of detecting a lesion on a noisy background. For this reason both the mean value and the variance are summarizing statistical parameters of the lesion area. The lesion covers a circumscribed area and has a signal level S_2 that is on average different from that of the background S_1, where S_j is some function $g(V)$ of the echo amplitude V. In the following, this formulation, rather than the linear one is used for reasons of generality.

$$\text{SNR}_\ell = \frac{\langle S_2 \rangle - \langle S_1 \rangle}{\sqrt{\sigma_{2,\ell}^2 + \sigma_{1,\ell}^2}}, \tag{A7}$$

where $\sigma_{j,\ell}^2$ = variance over the lesion area in case of background (j=1) or of lesion (j=2).

For the low contrast case, this formula reduces to

$$\text{SNR}_\ell = \frac{\langle S_2 \rangle - \langle S_1 \rangle}{\sigma_\ell \sqrt{2}}, \tag{A8}$$

The approximation by σ_ℓ is strictly valid in case of additive noise, and therefore does apply to the present problem only in the low contrast case, because the speckle has a Rayleigh distribution [6].

The relation of the statistical (lesion) area parameters to the point statistics (i.e., first order gray level parameters) has to be derived now. The lesion can be characterized by a weighting function $\alpha(x,y)$ which can be uniform (e.g., equal to unity), or any other function (e.g., Gaussian [14]). The numerator in equation (A7) can now be written:

$$\langle S_2 \rangle - \langle S_1 \rangle = A_\ell^{-1} \iint_{\text{area}} dx\,dy\,[g(V_2) - g(V_1)]\,\alpha(x,y), \tag{A9}$$

where A_ℓ = lesion area,
   x, y = Cartesian coordinates in image plane,
   $g(V)$ = some function of signal magnitude V.

For a uniform weighting, equation (A9) can be written:

$$\langle S_2 \rangle - \langle S_1 \rangle = \langle g(V_2) \rangle - \langle g(V_1) \rangle. \tag{A10}$$

The variance in either of the two conditions, $j = 1$ or 2, is:

$$\sigma_{j,\ell}^2 = A_\ell^{-2} \iint_{\text{area}} dx\,dy \left[\iint_{\text{area}} dx'\,dy'\,\alpha(x,y)C_S(x - x', y - y')\alpha(x',y') \right], \tag{A11}$$

where $C_S(x - x') = \langle (S(x) - \langle S(x) \rangle)(S(x') - \langle S(x') \rangle) \rangle$ = autocovariance corresponding to either S_1 or S_2. In case equation (A6) applies the analytic expression for C_S in equation (A11) can be found in [24] (see also [5]).

For a lesion that is large compared to the correlation length and if the differences $(x - x')$ and $(y - y')$ can be replaced by Δx and Δy, equation (A11) becomes [6]:

$$\sigma_{j,\ell}^2 = A_\ell^{-2} \iint\limits_{\text{area}} dx\,dy\; \alpha(\Delta x, \Delta y)\alpha(-\Delta x, -\Delta y)$$

$$\left[\iint\limits_{\text{area}} d\Delta x\,d\Delta y. \frac{C_S(\Delta x, \Delta y)}{C_S(0,0)}\right] C_S(0,0), \tag{A12}$$

For uniform weighting, $\alpha = $ constant, this equation reduces to:

$$\sigma_{j,\ell}^2 = A_\ell^{-1} A_c C_S(0,0), \tag{A13}$$

where $A_c = $ area under the normalized ACVF [6] = "area" of speckle cell.

Since $C_S(0,0) = \sigma_{j,p}^2$, where p refers to point statistics (see section A.1), equation (A13) can be written:

$$\sigma_{j,\ell}^2 = A_\ell^{-1} A_c \sigma_{j,p}^2. \tag{A14}$$

The lesion signal-to-noise ratio SNR_ℓ then follows from equations (A7), (A10) and (A14):

$$\text{SNR}_\ell = \frac{\langle g(V_2)\rangle - \langle g(V_1)\rangle}{\sqrt{(\sigma_{2,p}^2 + \sigma_{1,p}^2)A_\ell^{-1} A_c}}. \tag{A15}$$

which can be simplified to:

$$\text{SNR}_\ell = C_\ell\, \text{SNR}_p^*\, M^{\frac{1}{2}}, \tag{A16}$$

where

$$C_\ell = 2\frac{\langle g(V_2)\rangle - \langle g(V_1)\rangle}{\langle g(V_2)\rangle + \langle g(V_1)\rangle},$$

the lesion contrast,

$$\text{SNR}_p^* = \frac{1}{2}\frac{\langle g(V_2)\rangle + \langle g(V_1)\rangle}{\sqrt{\sigma_{1,p}^2 + \sigma_{1,p}^2}}, \tag{A17}$$

the "point signal-to-noise ratio" in the large contrast case,

$$M = A_\ell A_c^{-1}, \tag{A18}$$

the number of speckle correlation cells within the lesion area [6,8,26].

The area under the ACVF was analytically derived in [5]. The following equations specify the axial and lateral areas, respectively:

$$A_{cz} = \frac{0.685}{\Delta f} = 1.82\sigma_f \;(\text{mm}), \qquad \_ \tag{A19}$$

where $\Delta f = $ -6 dB bandwidth of the transmitted sound pulse in MHz,

$\sigma_f = $ "standard deviation" of Gaussian envelope of sound pulse in mm,

$$A_{cx} = 0.87\frac{\lambda_c z_F}{D'} \;(\text{mm}) \tag{A20}$$

where $\lambda_c = $ wavelength at central frequency f,

$z_F = $ depth of focus,

$D' = D/1.08 = $ effective diameter of (circular) transducer.

Appendix B

B   Gray Level Statistics of Nonlinearly Processed Echo Data

B.1   First order statistics

The gray level transforms considered here were inspired by the so-called postprocessing curves that are generally implemented in echographic equipment. The question to be studied is whether a gray level transform can be assessed that is optimal for lesion detection. The various transforms are shown graphically in figure 1.

The first step in the calculations is the estimation of the gray level histograms after applying a transform. The probability density function of a continuous function g of a random variable V is obtained from the original pdf $f(V)$ by:

$$f(V') = f(V)\left|\frac{dV'}{dV}\right|^{-1}.$$
(B1)

In the following, it is assumed that the envelope signal possesses a Rayleigh pdf.

B.1.1   Power law: $g(V) = V^n = V'$

$$f(V') = f(V)(nV^{n-1})^{-1}.$$
(B2)

Inserting the Rayleigh pdf (Eq. (A1)) yields:

$$f(V') = \frac{V^{2-n}}{n\sigma^2}\exp\left\{-\frac{V^2}{2\sigma^2}\right\}$$
(B3)

or,

$$f(V') = \frac{V'^{\frac{2-n}{n}}}{n\sigma^2}\exp\left\{\frac{-V'^{\frac{2}{n}}}{2\sigma^2}\right\}$$
(B4)

The mean and standard deviation can be calculated as well:

$$
\begin{aligned}
E\{V'\} &= \int_0^\infty dV\, g(V)f(V) = \int_0^\infty dV\frac{V^{n+1}}{\sigma^2}\exp\left\{-\frac{V^2}{2\sigma^2}\right\} \\
&= \Gamma(n/2+1)\,(2\sigma^2)^{\frac{n}{2}}.
\end{aligned}
$$
(B5)

Since $(V')^2 = V^{2n}$ it follows from the latter equation that:

$$E\{(V')^2\} = \Gamma(n+1)\,(2\sigma^2)^n,$$
(B6)

so

$$
\begin{aligned}
\sigma_{V'} &= \sqrt{E\{(V')^2\} - E^2\{V'\}} \\
&= (2\sigma^2)^{\frac{n}{2}}\sqrt{\Gamma(n+1) - \Gamma^2(n/2+1)}.
\end{aligned}
$$
(B7)

Therefore,

$$\mathrm{SNR}_p = \frac{\Gamma(n/2+1)}{\sqrt{\Gamma(n+1) - \Gamma^2(n/2+1)}},$$
(B8)

which is a constant, given the value of n.

Likewise, it follows for the large contrast case (Eq. (A17)) that:

$$\text{SNR}_p^* = \frac{\Gamma(n/2+1)\left[(2\sigma_2^2)^{\frac{3}{2}} + (2\sigma_1^2)^{\frac{3}{2}}\right]}{\sqrt{\left[\Gamma(n+1) - \Gamma(n/2+1)\right]\left[(2\sigma_2^2)^n + (2\sigma_1^2)^n\right]}} \tag{B9}$$

B.1.2   General logarithmic law: $g(V) = \{\ln(1+V)\}^n = V'$

The general logarithmic law (i.e., n is a real number), is considered because the postprocessing of echographic data most often is performed on the logarithmically compressed and digitally stored echographic data. The natural logarithm rather than the ten-base logarithm is employed because of convenience when exponential functions are involved. This choice has no consequences for any of the defined signal-to-noise ratios.

As above for section B.1:

$$\frac{dV'}{dV} = \frac{n\{\ln(1+V)\}^{n-1}}{1+V} \tag{B10}$$

Insertion of expression (B9) and the Rayleigh pdf in equation (B1) yields:

$$f(V') = \frac{V}{n\sigma^2} e^{-\frac{V^2}{2\sigma^2}} (1+V) \{\ln(1+V)\}^{1-n}. \tag{B11}$$

Taking $V \gg 1$ yields :

$$f(V') \approx \frac{V^2}{n\sigma^2} e^{-\frac{V^2}{2\sigma^2}} \{\ln(1+V)\}^{1-n} \text{ or,} \tag{B12}$$

$$f(V') \approx \frac{V'^{\frac{1-n}{n}}}{n\sigma^2} e^{-2V'^{\frac{1}{n}}} \exp\left\{\frac{-e^{2V'^{\frac{1}{n}}}}{2\sigma^2}\right\}, \tag{B13}$$

The point signal-to-noise ratio SNR_p will now be derived by using the approximation formulas for the mean and standard deviation which were given by Papoulis [25]:

$$\mu_{V'} \approx \left[g(V) + \frac{d^2 g(V)}{dV^2} \frac{\sigma_V^2}{2}\right]_{V=\mu_V} \tag{B14}$$

$$\sigma_{V'} \approx \sigma_V \left[\frac{dg(V)}{dV}\right]_{V=\mu_V} \tag{B15}$$

The expressions become for the general logarithmic law:

$$\mu_{V'} \approx [\ln(1+\mu_V)]^n + \frac{n\sigma_V^2[n-1-\ln(1+\mu_V)]}{2[\ln(1+\mu_V)]^{2-n}(1+\mu_V)^2} \tag{B16}$$

$$\sigma_{V'} \approx n\sigma_V \frac{[\ln(1+\mu_V)]^{n-1}}{1+\mu_V}, \tag{B17}$$

and

$$\text{SNR}_p \approx \frac{\mu_V}{\sigma_V} \frac{\ln(1+\mu_V)}{n} + \frac{\sigma_V}{2\mu_V}\left\{\frac{n-1}{\ln(1+\mu_V)} - 1\right\}. \tag{B18}$$

Insertion of equations (A2) and (A3) yields the SNR_p for a Rayleigh distribution,

$$\text{SNR}_p \approx \frac{\ln\left(\sigma^2\pi/2\right)}{2n\sqrt{4/\pi-1}} + \sqrt{4/\pi-1}\left\{\frac{n-1}{\ln\left(\sigma^2\pi/2\right)} - \frac{1}{2}\right\}. \tag{B19}$$

For the simple logarithmic law $(n = 1)$, this becomes

$$\text{SNR}_p \approx \frac{[\ln(\sigma^2\pi/2) - (4/\pi-1)]}{2\sqrt{4/\pi-1}}. \tag{B20}$$

Because in this latter case of $n = 1$ equation (B17) yields $\sigma_{V'} \approx \sqrt{4/\pi-1}$, which is a constant, it can be concluded that a simple logarithmic transformation results in additive noise.

B.1.3   Sigmoid law: $g(V) = \arctan\left[\ln(1 + V) - 1\right] + \pi/2 = V'$

Using equation (B1) yields for this case:

$$f(V') \approx \frac{V^2}{\sigma^2}\left[1 + \{\ln(1 + V) - 1\}^2\right] e^{-V^2/2\sigma^2}. \tag{B21}$$

The expression for $f(V')$ in which V is replaced by V' is rather lengthy and is omitted.

The SNR_p can again be obtained with equations (B14) and (B15):

$$\mu_{V'} \approx \arctan\{\ln(1 + \mu_V) - 1\} + \frac{\pi}{2} - \frac{\sigma_V^2\{\ln(1 + \mu_V) + 2\}^2}{2(1 + \mu_V)^2\{1 + (\ln(1 + \mu_V) - 1)^2\}^2}, \tag{B22}$$

$$\sigma_{V'} \approx \frac{\sigma_V}{(1 + \mu_V)\{1 + (\ln(1 + \mu_V) - 1)^2\}}. \tag{B23}$$

Assuming $\mu_V \gg 1$ and inserting μ_V and σ_V from equations (A2) and (A3):

$$\mu_{V'} \approx \arctan\{\tfrac{1}{2}\ln(\frac{\sigma^2\pi}{2}) - 1\} + \frac{\pi}{2} - \frac{\sigma^2(1 - \frac{\pi}{4})\{\tfrac{1}{2}\ln(\frac{\sigma^2\pi}{2}) + 2\}^2}{(1 + \sigma\sqrt{\frac{\pi}{2}})^2\{1 + (\tfrac{1}{2}\ln(\frac{\sigma^2\pi}{2}) - 1)^2\}^2}, \tag{B24}$$

$$\sigma_{V'} \approx \frac{\sigma\sqrt{2 - \frac{\pi}{2}}}{(1 + \sigma\sqrt{\frac{\pi}{2}})\{1 + (\tfrac{1}{2}\ln(\frac{\sigma^2\pi}{2}) - 1)^2\}}, \tag{B25}$$

and SNR_p follows from the ratio of these latter two expressions.

The SNR_p^* (i.e., large contrast case) for the latter two nonlinear transforms is not written down explicitly, but it can be obtained by inserting the results given by equations (B24) and (B25) into equation (A17).

B.2   Second order statistics

The autocorrelation function can be obtained from the second order pdf (viz., Eq. (A6)):

$$E\{g(V(x))g(V(x')); \Delta x\} = \iint\limits_{-\infty}^{\infty} g(V(x))g(V(x'))f_2(V(x), V(x'); \Delta x)dV(x)dV(x'), \tag{B26}$$

where $\Delta x = x' - x$.

B.2.1 Power law transform

For this case, the ACF can be calculated analytically [5,24]:

$$E\{V^n(x), V^n(x'); \Delta x\} = (2\sigma_V^2)^n \, \Gamma^2(\frac{n}{2} + 1) \, {}_2F_1(-\frac{n}{2}, -\frac{n}{2}; 1; |k_0|^2), \qquad \text{(B27)}$$

where $_2F_1$ = hypergeometric function
Γ = gamma function

B.2.2 Logarithmic and sigmoid transforms

We did not achieve the derivation of analytic expressions from equation (B26), so the ACVF had to be calculated numerically in these two cases.

B.3 Lesion signal-to-noise ratio

By using the lesion signal-to-noise ratio as defined by equation (A16), the expression for SNR_ℓ in case of power law transforms can be obtained by inserting equations (B9) and (B27).

In case of power law transforms of the log-compressed data, the SNR_ℓ can be obtained by substituting equations (B24) and (B25) and the calculated size of the ACVF (Figs. 5c, 6a, 6b) into equation (A16).

Arsenault and April [23] derived the speckle signal-to-noise ratio integrated with a finite aperture in the case of simple log-compressed data. They took the "effective number of speckles" M to be independent of the log compression and showed that

$$SNR_\ell \approx \langle \ln(V^2) \rangle \, M^{\frac{1}{2}} \quad (M > 5). \qquad \text{(B28)}$$

References

[1] CCIR Recommendation 470-1, report 624-1 (1982).

[2] Burckhardt, C.B., Speckle in ultrasound B-mode scans, *IEEE Trans. Son. Ultrason.* SU-25, 1-6 (1978).

[3] Abbott, J.G., and Thurstone, F.L., Acoustic speckle: theory and experimental analysis, *Ultrasonic Imaging 1*, 303-324 (1979).

[4] Bamber, J.C., and Dickinson, R.J., Ultrasonic B-scanning: a computer simulation, *Phys. Med. Biol. 25*, 463-479 (1980).

[5] Wagner, R.F., Smith, S.W., Sandrik, J.M., and Lopez, H., Statistics of speckle in ultrasound B-scans, *IEEE Trans. Son. Ultrason. SU-30*, 156-163 (1983).

[6] Smith, S.W., Wagner, R.F., Sandrik, J.M., and Lopez, H., Low contrast detectability and contrast/detail analysis in medical ultrasound, *IEEE Trans. Son. Ultrason.* SU-30, 156-163 (1983).

[7] Smith, S.W., and Wagner, R.F., Ultrasound speckle size and lesion signal to noise ratio: verification of theory, *Ultrasonic Imaging 6*, 174-180 (1984).

[8] Goodman, J.W., Statistical Properties of Laser Speckle Patterns, in *Laser Speckle and Related Phenomena*, J.C. Dainty, ed., pp. 9-75 (Springer, Berlin, 1975).

[9] Foster, D.E., Arditi, M., Foster, F.S., Patterson, M.S., and Hunt, J.W., Computer simulations of speckle in B-scan images, *Ultrasonic Imaging 5*, 308-330 (1983)

[10] Oosterveld, B.J., Thijssen, J.M., and Verhoef, W.A., Texture of B-mode echograms· 3-D simulations and experiments of the effects of diffraction and scatterer density, *Ultrasonic Imaging 7*, 142-160 (1985).

[11] Patterson, M.S., and Foster, F.S., The improvement and quantitative assessment of B-mode images produced by an annular array/cone hybrid, *Ultrasonic Imaging 5*, 195-213 (1983).

[12] Thijssen, J.M., and Oosterveld, B.J., Texture in B-mode Echograms: a Simulation Study of the Effects of Diffraction and of Scatterer Density on Gray Scale Statistics, in *Acoustical Imaging*, Vol. 14, A.J. Berkhout, J. Ridder, and L.F. van der Wal, eds., pp. 481-486 (Plenum, New York, 1985).

[13] Thijssen, J.M., and Oosterveld, B.J., Performance of Echographic Equipment and Potentials for Tissue Characterization, in *Proceedings NATO Advanced Study Institute on Mathematics and Computer Science in Medical Imaging*, M.A. Viergever, and A. Todd-Prokopek, eds., pp. 455-468 (Springer, Berlin, 1987).

[14] Wagner, R.F., and Brown, D.G., Unified SNR analysis of medical imaging systems, *Phys. Med. Biol. 30*, 489-518 (1985).

[15] Smith, S.W., Lopez, H., and Bodine, W.J., Frequency independent ultrasound contrast - detail analysis, *Ultrasound Med. Biol. 11*, 467-477 (1985).

[16] Smith, S.W., and Lopez, H., A contrast-detail analysis of diagnostic ultrasound imaging, *Med. Phys. 9*, 4-12 (1982).

[17] Thijssen, J.M., Oosterveld, B.J., and Wagner, R.F., Dependence of speckle statistics and lesion detection on nonlinear gray scale coding, *Ultrasonic Imaging 9*, 58 (1987) (abstract).

[18] Verhoef, W.A., Cloostermans, M.J.T.M., and Thijssen, J.M., The impulse response of a focussed source with an arbitrary axisymmetric surface velocity distribution, *J. Acoust. Soc. Amer. 75*, 1716-1721 (1984).

[19] Verhoef, W.A., Cloostermans, M.J.T.M., and Thijssen, J.M., Diffraction and dispersion effects on the estimation of ultrasound attenuation and velocity in biological tissues, *IEEE Trans. Biomed. Eng. BME-32*, 521-529 (1985).

[20] Kruimer, W.H., Lammers, J.H.E., and Thijssen, J.M., Ultrasonic Biopsy Apparatus, in *Acoustical Imaging*, Vol. 14, A.J. Berkhout, J. Ridder, and L.F. van der Wal, eds., pp. 665-668 (Plenum New York, 1985).

[21] Cloostermans, M.J.T.M., and Thijssen, J.M., A beam corrected estimation of the frequency dependent estimation of biological tissues from backscattered ultrasound, *Ultrasonic Imaging 5*, 136-147 (1983).

[22] Oosterveld, B.J., Thijssen, J.M., Hartman, P.C., and Rosenbusch, G.J.E., Preprocessing and Texture Analysis of In-vivo B-mode Echograms, in *Ultrasonic Tissue Characterization and Echographic Imaging*, Vol. 6, J.M. Thijssen and G. Berger, eds., pp. 43-50 (Office for Official Publ. European Comm., Luxembourg, 1987).

[23] Arsenault, H.H., and April, G., Properties of speckle integrated with a finite aperture and logarithmically transformed, *J. Opt. Soc. Am. 66*, 1160-1163 (1976).

[24] Middleton, D., *An Introduction to Statistical Communication Theory* (McGraw-Hill, New York, 1960).

[25] Papoulis, A., *Probability, Random Variables and Stochastic Processes* (McGraw-Hill, New York, 1965).

[26] Goodman, J.W., *Statistical Optics* (Wiley, New York, 1985).

VII

Ultrasound Attenuation and B-mode Texture Analysis of Diffuse Liver Disease: Methods and Preliminary Results

B.J.Oosterveld   J.M.Thijssen   P.C.Hartman   R.L.Romijn
G.J.E.Rosenbusch

A study was performed to find and test quantitative methods of analysis of echographic signals for the differentiation of diffuse liver diseases. An on-line data acquisition system was used to acquire radiofrequency echo signals from volunteers and patients. Several methods to estimate the frequency dependent attenuation coefficient were evaluated, in which a correction for the frequency and depth dependent diffraction and focussing effects caused by the sound beam was applied. Using the estimated value of the attenuation coefficient the rf signals themselves were corrected to remove the depth dependencies caused by the sound beam and by the frequency dependent attenuation. After this preprocessing the envelope of the corrected rf signals was calculated and B-mode images were reconstructed. The texture of the B-mode images was analyzed by first and second order statistical methods.
The accuracy and precision of the attenuation methods were assessed by using computer simulated rf signals and rf data obtained from a tissue-mimicking phantom. The phantom measurements were also used to test the performance of the methods to correct for the depth dependencies. The echograms of 163 persons, both volunteers and patients suffering from a diffuse liver disease (cirrhosis, hepatitis, haemochromatosis), were recorded. We studied the reproducibility over a 5 day period and the influence of the biological diurnal rhythm on the evaluated ultrasound parameters. The mutual correlations between the estimated parameters were used to preselect parameters contributing independent information and which could subsequently be used in a discriminant analysis to differentiate between the various diseased conditions.

Key words: acoustic speckle, attenuation, cirrhosis, diffraction correction, diffuse liver disease, texture analysis, ultrasound.

1   Introduction

Based on the experience from in-vitro experiments with liver specimens [1,2] and from extensive computer simulations using realistic three dimensional tissue and transducer models [3,4], we have performed a clinical study on the characterization of the liver by quantitative analysis of radiofrequency ultrasound signals. Since the methods were not designed for the detection of focal lesions we have confined ourselves to diffuse liver diseases, in which it was assumed that changes had affected the whole organ.

Other investigators have reported on the results of their clinical studies concerning diffuse liver disease, using attenuation measurements [5,8,6,7], as well as the analysis of the B-mode texture [9,10,11,12]. Most procedures for the estimation of the attenuation coefficient employ some corrections for the depth dependent properties of the sound beam, which would otherwise influence the estimation [2,3,13,14].

The sound beam, however, also causes a depth dependence of the B-mode image texture. Correction of the image [15], or correction of the parameters from texture analysis [12] for this influence, has only been attempted in a simple way. Usually however, the analysis is confined to a region of interest (ROI) that has a fixed distance to the transducer [9,10]. In this way the influence of the sound beam is reduced, but the flexibility in the choice of the ROI also. Furthermore, this method does not reduce the influence that the attenuation has on the texture [4], and finally, the results obtained can not easily be generalized.

The texture analysis methods range from well known methods designed primarily for optical images [9,10,12], to methods which are based on realistic models of the liver tissue and a deeper theoretical insight in the acoustical interactions between the tissue and the interrogating sound pulses [11,16].

We have designed a method to produce B-mode scans from the rf signals, which are first corrected for the diffraction and focussing effects and for the depth dependencies caused by attenuation. To investigate the potentials of our method we have performed a retrospective clinical study. We have scanned a group of patients with a variety of liver pathologies, among which biopsy proven liver cirrhosis, and a group of volunteers who had a normal liver. We used a measurement setup that enabled us to digitize and store the rf signals corresponding to a region of interest, obtained in vivo. Several methods to estimate the attenuation coefficient were employed. From the corrected envelope of the rf signals texture parameters were estimated. The discriminating power of the obtained echographic parameters was investigated by applying a Student t-test.

2 Analysis of the Echo Signals

2.1 Diffraction Correction: Theoretical Background

The echoes received by the transducer are the result of the linear accumulation of backscatterings from inhomogeneities in the tissue. The signal as it is observed depends on the transducer geometry and the properties of the interrogated medium. This can be described by various complex transfer functions, of which the following can be distinguished:

- $P(f)$ the electroacoustic round-trip transfer function of the piezoelectric material of the transducer, which is involved in the conversion of electric energy to acoustic energy and vice versa,

- $S(f)$ the average backscattering coefficient of the tissue inhomogeneities, which is assumed to be constant in the region of interest (homogeneous and isotropic),

- $H'_t(f, \vec{r}), H'_r(f, \vec{r})$ the transfer functions associated with the impulse response function of the transducer at position $\vec{r}$ (Fig. 1), in transmission and reception, respectively.
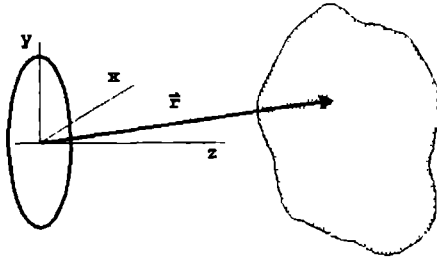
Figure 1: *Transducer and tissue in a in cartesian coordinate system*

These latter transfer functions depend on the transducer geometry (focussing and aperture diffraction) and the propagation characteristics of the medium. If the point $\vec{r}$ is approximately equidistant to all points of the transducer aperture (i.e., far field approximation), these transfer functions may be separated into a tissue transfer function A and a diffraction transfer function H:

$$H'_t(f,\vec{r}) = H_t(f,\vec{r})A(f,r) \tag{1}$$

$$H'_r(f,\vec{r}) = H_r(f,\vec{r})A(f,r) \tag{2}$$

The functions $H_t(f,\vec{r})$ and $H_r(f,\vec{r})$ relate to the impulse response functions in a lossless medium and are identical due to the validity of reciprocity in the pulse-echo mode. Therefore, the subscripts can be omitted.

A general description of the tissue transfer function is given by

$$A(f,r) = \exp[-\alpha(f)r] \tag{3}$$

For biological tissues the attenuation coefficient $\alpha(f)$ is usually approximated to be linear with frequency

$$\alpha(f) = \beta f \tag{4}$$

Using the described transfer functions the spectrum of the echo signal due to one scatterer at position $\vec{r}$ can be described by

$$\begin{aligned} E(f) &= P(f)H'_t(f,\vec{r})S(f)H'_r(f,\vec{r}) \\ &= P(f)H^2(f,\vec{r})A^2(f,r)S(f) \end{aligned} \tag{5}$$

Written as a function of time we have

$$e(t) = p(t) * h(t,\vec{r}) * a(t,r) * s(t) * a(t,r) * h(t,\vec{r}) \tag{6}$$

where $*$ denotes a convolution. If there is more than one inhomogeneity present in the tissue the resulting echo signal is the linear summation of the individual echoes

$$e(t) = \sum_j e_j(t), \tag{7}$$

where j is the index of the scatterer at position $\vec{r}_j$. In the frequency domain this results in

$$E(f) = \sum_j E_j(f)$$

$$\begin{aligned}
&= P(f)S(f)\sum_j H^2(f,\vec{r}_j)A^2(f,r_j) \\
&= P(f)S(f)\sum_j H^2(f,\vec{r}_j)\exp[-2\alpha(f)r_j] \qquad (8)
\end{aligned}$$

provided that the backscattering function $S(f)$ is the same for all inhomogeneities. If only a small time portion of the echo signal is considered the individual echoes $e_j(t)$ will arise at inhomogeneities in a small volume (isochronous volume) at an axial distance z from the transducer, which is corresponding to the product of sound velocity c and half of the travel time t. The distances r_j are approximately equal to this depth z and therefore the attenuation factor can be approximated by $\exp[-2\alpha(f)z]$. Also the diffraction transfer function can be approximated by an average transfer function dependent on depth, $H(f,z)$. The echo signal from an isochronous volume at depth z can now be written as

$$E(f,z) = P(f)S(f)H^2(f,z)\exp[-2\alpha(f)z] \qquad (9)$$

From this equation it is clear that a depth independent estimation of the attenuation is only possible if the average transfer function due to diffraction and focussing $H^2(f,z)$ is known.

Also the texture of the envelope image shows a depth dependence which is not only caused by the sound beam but by the attenuation as well [4]. In the lateral direction the speckle size is inversely proportional to the centre frequency of the propagating pulse, which decreases with depth, due to attenuation. If the pulse has a Gaussian shaped envelope the speckle size in the axial direction is not influenced by attenuation. The reason for this is that the axial speckle size is dependent on the bandwidth of the propagating pulse only, which is preserved in this special case of a linear-with-frequency attenuation coeffient. If, however, the pulse shape is not approximately Gaussian, a correction for the attenuation has to be carried out as well for the axial envelope characteristics to become depth independent.

The diffraction transfer function can be estimated by recording rf signals from a tissue mimicking phantom placed in a watertank. If the method outlined in section 3.2 is used, the spectra of the rf signals corresponding to a number of depth segments Δz at distances z_i, for $i = 1,\ldots,n$, from the transducer are obtained such that the depth segments overlap by 50 percent ($z_i = z_{i-1} + \frac{1}{2}\Delta z$). The resulting amplitude spectrogram is the average diffraction filter multiplied by the transfer function $S_{ph}(f)$ of the scatterers within the phantom and by the electroacoustic transfer function $P(f)$ of the transducer

$$E_{ph}(f,z_i) = P(f)\,S_{ph}(f)\,H^2(f,z_i), \qquad (10)$$

where $i = 1,\ldots,n$.

If the spectrogram given by equation (10) is normalized with respect to the spectrum obtained in the focal zone ($z_i = F$) this results in

$$\begin{aligned}
H_c^2(f,z_i) &= \frac{E_{ph}(f,z_i)}{E_{ph}(f,F)} \\
&= \frac{P(f)\,S_{ph}(f)\,H^2(f,z_i)}{P(f)\,S_{ph}(f)\,H^2(f,F)} \\
&= \frac{H^2(f,z_i)}{H^2(f,F)}, \qquad (11)
\end{aligned}$$

the diffraction transfer function normalized with respect to the focal zone. The normalization thus removes the properties of the tissue phantom. This normalized diffraction transfer filter $H_c^2(f, z_i)$ represents the change of the spectral content of the rf echo signals due to the depth dependence caused by diffraction and focussing. Correction of a depth segment of a rf signal, e.g. obtained in-vivo, is performed by dividing its spectrum by the normalized spectrum of the filter corresponding to the same depth.

2.2 Estimation of the Attenuation

Amplitude spectra were calculated using the depth segments of each rf line corresponding to the same distances to the transducer as mentioned above. Prior to the Fourier transformations the segments were multiplied by a Hanning window [17]. The spectrogram was obtained by ensemble averaging the amplitude spectra at each depth over the rf lines of the ROI (cf. Eq. (9)):

$$E(f, z_i) = P(f)S(f)H^2(f, z_i) \exp[-2\alpha(f)z_i], \tag{12}$$

where $i = 1, \ldots, n$ with n the number of 50 percent overlapping depth segments in the ROI. Correction of this spectrogram with the correction filter of equation (11) yielded

$$
\begin{aligned}
E_c(f, z_i) &= E(f, z_i)/H_c^2(f, z_i) \\
&= P(f)\, S(f)\, H^2(f, F)\, \exp[-2\alpha(f)z_i].
\end{aligned}
\tag{13}
$$

Since $P(f)\,S(f)\,H^2(f, F)$ is independent of depth, equation (13) can be used to find $\alpha(f)$ once $E_c(f, z_i)$ is known for a range of depth segments in the tissue.

Several approaches were used to estimate the attenuation coefficient from the corrected spectrogram of equation (13). All these methods are based on the assumption that the interrogated medium is homogeneous. In the multi-narrowband (MNB) approach [1] a two step linear fit method is employed. To the logarithmic spectral values at each frequency f_k, $(k = 1, \ldots, K)$ in the usable bandwidth, straight lines are fitted versus depth z_i. This yields the attenuation coefficient as a function of frequency $\alpha(f_k)$, $(k = 1, \ldots, K)$. Fits were applied to these values versus frequency, corresponding to three models for the frequency dependence of $\alpha(f)$:

- $\alpha(f) = \alpha_0 + \alpha_1 f$, a linear fit (MNB),

- $\alpha(f) = \beta f$, a linear fit, forced to have zero intercept (MNB$_0$),

- $\alpha(f) = \alpha_p f^n$, a linear fit through the logarithm of the attenuation coefficient values (MNB$_p$), yielding α_p as the value at 1 MHz and n as the slope of this fit.

The multi-narrowband method is similar to the spectral-difference method [18], but provides a more efficient use of the echodata.

If the attenuation is assumed to be linear with frequency, $\alpha(f) = \beta f$, the centroid frequency shift (CFS) method (or: spectral shift method) [19,20,21,22] can be applied by estimating the central frequency f_c (i.e., the first order spectral moment) versus depth from the corrected spectrogram. The attenuation coefficient β then follows from the slope of a linear fit to these values versus depth,

$$\beta = -\frac{1}{2\sigma_f^2} \frac{\triangle f_c}{\triangle z}, \tag{14}$$

where σ_f is the standard deviation of the Gaussian amplitude spectra averaged over
        all depths,

$\triangle f_c / \triangle z$ is the slope of the fitted line.

For the log-power decay (LPD) method (or: quasi-narrow band method) [5,2] the amplitude spectra versus depth were squared and integrated over the frequency to yield the zeroth-order power spectral moments (M_0), after which the logarithm was taken. The attenuation coefficient was then estimated using

$$\beta = -\frac{1}{4\overline{f}_c}\frac{d \log M_0(z)}{dz}, \tag{15}$$

where $\overline{f}_c$ = the average central frequency in the ROI. A straight line was fitted through the log power values versus depth and the slope of this line divided by the central frequency, averaged over all depths, resulted in another estimate of the attenuation coefficient β. For the MNB and MNB$_p$ methods less strict assumptions are made, and therefore, more general information may be extracted about the tissue.

If a homogeneous medium is considered and the spectral amplitude at each frequency is assumed to be Rayleigh distributed, then the variance of the estimate of the attenuation coefficient can be derived [23,25]:

$$\sigma_\beta^2 = \frac{18 c \sigma_r^2}{(1-o)^2 (W L_w)^3 n^3 (1 - \frac{1}{n^2}) N} \tag{16}$$

where c = speed of sound,

σ_r^2 = relative variance of the spectral amplitude = 5.61 dB,

W = usable bandwidth,

L_w= window length,

o = window overlap expressed as a fraction of the window length,

n = number of windows,

N = number of independent scan lines.

2.3   Calculation of the envelope of the corrected rf signals

The most rigorous way to remove all the influences of the applied transducer from the rf signals would be by inverse filtering for its depth dependent point spread function. This would involve two dimensional deconvolutions in a number of depth segments of the image. The result of performing such an operation on a rf sector scan would be an image of the scattering inhomogeneities not obscured by speckle. Jeurens et al. [26] investigated this procedure and concluded that it would only produce satisfying results if the data would meet certain high quality requirements. Since the data recorded with our equipment (see section 3.1) did not meet these demands we restricted ourselves to correcting the rf signals for those influences that cause a depth dependence of the B-mode lines in the depth direction only. That is, we compensated for depth dependent diffraction and focussing effects, as well as for the attenuation, in the frequency domain (cf. Eq. (11)).

Having found the value of the attenuation coefficient the envelope of the rf signals, corrected for the diffraction effects and for the attenuation, was calculated. We proceeded line by line in the same way as with the calculation of the spectrogram, that was

used for the estimation of the attenuation, by using 50 percent overlapping depth segments. Each segment was multiplied by a Hanning window and then the amplitude and phase spectra were calculated by using FFT. These were corrected for the diffraction (cf. Eq. (11)) and the attenuation. This preprocessing was comprised in a compound complex transfer function:

$$E_c(f, z_i) = |E_c(f, z_i)| \exp[i\phi_c(f, z_i)], \tag{17}$$

where

$$|E_c(f, z_i)| = |E(f, z_i)| \frac{\exp[\beta f(z_i - z_0)]}{|H_c^2(f, z_i)|} \tag{18}$$

$$\phi_c(f) = \phi(f) - \frac{2\beta f(z_i - z_0)}{\pi}\{\ln(2\pi f) - \tau_m\}, \tag{19}$$

and depth z_0 corresponds to a specific distance from the transducer, for example corresponding to the boundary of the liver. The correction applied to the phase spectrum (Eq. (19)) was obtained using the causal attenuation model derived by Gurumurthy and Arthur [27]. As proposed by these authors we have taken the minimum-phase delay factor τ_m equal to 20.0. Complex demodulation was performed in the frequency domain. The spectrum of the complex preenvelope was calculated by multiplying the positive frequency part of equation (18) by two and making the negative frequency part equal to zero [28]. The resulting spectra were then transfered back to the time domain (preenvelope) which, after taking the absolute value, yielded the envelope of the segment. Interpolation between the consecutive overlapping segments was neatly performed by the Hanning data window that was applied prior to the calculation of the spectra. Therefore, the resulting envelope segments could simply be added, taking into account the appropriate time delays. By using this approach only a correction in the axial direction was accomplished. In other words, the speckles still showed depth dependence in the lateral direction, although some change of the texture was evident. For this reason the second order analysis of the image texture was confined to the axial direction only.

2.4   Analysis of the B-mode texture

First and second order texture analysis methods were used, to extract quantitative information from the resulting B-mode images. The first order statistics characterize the histogram of the echo amplitudes. Two parameters were estimated from the histogram: the average echo amplitude (μ) and the average amplitude divided by the standard deviation (signal-to-noise ratio, SNR $= \mu/\sigma$). For a scattering medium that contains homogeneously distributed and randomly positioned scatterers with a high number density a value of 1.91 is expected for the SNR, which corresponds to a histogram that approximates a Rayleigh probability density function. Deviations from this limiting situation are expected if the density of scatterers is low (sub-Rayleigh) [4] or if a part of the scatterers is regularly spaced (i.e., structure is present) [29]. The average amplitude (μ) depends on the strength of the scatterers and on the square root of the number density of the scatterers [4].

The second order statistics were confined to the axial autocovariance function and its Fourier transform, viz. the power spectrum, of the echo intensity. The full width at
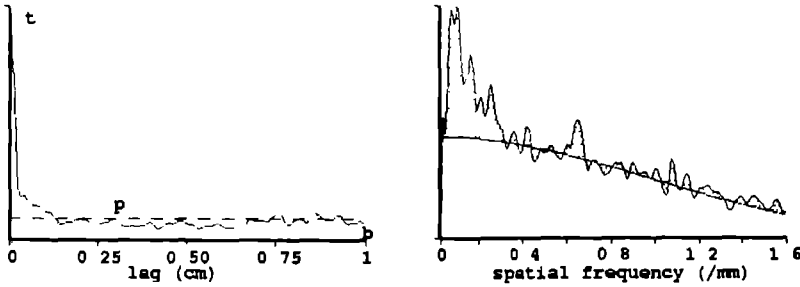
Figure 2: *Autocorrelation function (a) and corresponding noise power spectrum (b). The absissa are in arbitrary units. (t, p, and b: see text).*

half maximum (FWHM) of the autocovariance function was used as an estimate of the average size of the speckles in the axial direction.

In some biological tissues two kinds of scatterers may be distinguished in addition to reflecting boundaries of organs and blood vessels. The first kind are randomly positioned scatterers with a high number density, which cannot be resolved by the transducer. The second kind are scatterers which are positioned in a more or less regular order with average spacing $\bar{d}$. These scatterers, therefore, are structured and the periodicity may or may not be resolved by the transducer. As an example the liver can be considered. The liver cells are organized in lobules, cylindrical structures with a diameter of approximately 1 mm. Because the cells and capillaries are randomly positioned within the lobules they cause random scattering. The spaces between the lobules (triads of Kiernan) are collagen rich, and constitute a more or less regular hexagonal structure. Since collagen is a strongly scattering medium this structure may cause "structural scattering".

Following the unified approach of Wagner and Insana [11,16] the intensity contributions due to structure (I_s) and due to random (or diffuse) scattering (I_d) were estimated. The intensity due to structure is subdivided into a constant part $(\bar{I}_s)$ representing the unresolvable part of the structure and a variable part $(\sigma(I_s))$ representing the resolvable part. $\bar{I}_s$, $\sigma(I_s)$ and I_d were estimated from the autocorrelation function of the intensity and from its Fourier transform, the power spectrum. Refering to figure 2 and using the notation of these authors, the following parameters of the autocorrelation function, $R_I(\Delta z)$, were distinguished

$$t \;=\; R_I(0) = \overline{I^2} = 2I_d^2 + 4I_d\bar{I}_s + \overline{I_s^2} = 2\sigma_R^2 + \overline{I_s^2} \tag{20}$$

$$p \;=\; R_I(nd) = I_d^2 + 2I_d\bar{I}_s + \overline{I_s^2} = \sigma_R^2 + \overline{I_s^2} \tag{21}$$

$$b \;=\; R_I(\infty) = \overline{I}^2 = I_d^2 + 2I_d\bar{I}_s + \overline{I}_s^2 = \sigma_R^2 + \overline{I}_s^2 \tag{22}$$

where $\sigma_R^2 = I_d^2 + 2I_d\bar{I}_s$ is the Rician variance, and p is the value of maximum structured correlation.

From equations (20) and (22) and the definition of the variance of the intensity due to structure, $\sigma^2(I_s) = \overline{I_s^2} - \overline{I}_s^2$, it follows that

$$\sigma^2(I) = \overline{I^2} - \overline{I}^2 = \sigma_R^2 + \sigma^2(I_s) \tag{23}$$

Using equations (22) and (23) we find

$$\overline{I}_s = \sqrt{\overline{I}^2 - \sigma_R^2} = \sqrt{2\overline{I}^2 - \overline{I^2} + \sigma^2(I_s)} \tag{24}$$

In practice, the values of $\overline{I}^2$ and $\overline{I^2}$ are obtained from the first order statistics of the intensity. To find the value of $\sigma^2(I_s)$ the power spectrum is partitioned. The Rician variance σ_R^2 is estimated as the area under the Gaussian fit to the minima of the spectrum. Since the total area under the power spectrum is equal to $\sigma^2(I)$, $\sigma^2(I_s)$ can be estimated using equation (23). I_d then follows from $I_d = \overline{I} - \overline{I}_s$.

The following tissue characterizing parameters were used: the average intensity due to structure normalized to the intensity due to diffuse scattering ($\overline{I}_s/I_d$), and the variable component of the intensity due to structure normalized to the intensity due to diffuse scattering ($\sigma(I_s)/I_d$).

Pronounced peaks in the power spectrum, corresponding to the distance d between the regularly spaced scatterers (viz. the structured scattering), were located. Only periodicities larger than the resolution of the transducer and smaller than 3 mm were considered. The distances corresponding to the peaks were averaged [11] with weighting factors equal to the difference between the spectral peak value and the value of the Gaussian fit at that frequency.

3   Methods

3.1   Data acquisition equipment

To be able to record the rf signals in-vivo a conventional echo scanner was interfaced to a transient recorder and a microcomputer. A preliminary version of the equipment that was used was described in detail before [30]. The system was controlled by a personal computer (PRO380, Digital Equipment Inc.) which was also used for the storage of the recorded rf signals. As the ultrasonic front-end a mechanical sector scanner (Sonoline 3000, Siemens Inc.) was used, equipped with a transducer with a fixed focal distance (F=7.5 cm, f_c=3.0 MHz, $\triangle f_{1/2}$=0.94 MHz). On the screen of the scanner a region-of-interest (ROI), with variable position and size, was made visible for the selection of homogeneous portions of the tissue. After the operator pressed a switch, the rf signals corresponding to the selected ROI were recorded during a single scanning motion of the transducer. The recorded rf signals were digitized and intermediately stored by a transient recorder (BE256, Bakker Electronics), which operated at 12 MHz sampling rate and had a resolution of 8 bits. The rf signals were amplified by the TGC (Time dependent Gain Control) amplifier of the scanner, but were not logarithmically compressed.

During the data acquisition the quality of the recorded rf data was assessed on-line by performing an initial analysis using an array processor (VAP64B, DSP Inc.). If the number of segments where the rf signal caused overflow in the transient recorder was
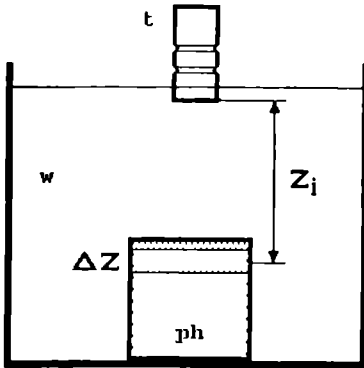
Figure 3: *Experimental set up used to measure the depth dependent properties of the sound beam. (t=transducer, ph=phantom, w=water).*

higher than 25 percent, the operator was automatically alerted to either change the setting of the TGC or to avoid strong reflectors. After each recording session the data were transferred to a PDP 11/34 computer (Digital Equipment Inc.) on which further analysis was performed off-line.

Before any analysis of the data was performed the depth dependent amplification was removed from the signals. For this purpose the steering voltage of the TGC amplifier, which corresponds to a certain amplification factor, was also digitized and stored in addition to the rf signals. The relationship between the steering voltage and the amplification was measured by recording the rf echo signals of a tissue phantom at a number of steering voltage levels. The spectra of these echoes were calculated and normalized with respect to the spectrum corresponding to one of the steering voltage levels (1 Volt), thus yielding the relative amplification factor as a function of frequency and of steering voltage. No significant frequency dependence of the amplification was observed. The relationship between steering voltage and amplification, however, appeared to be depth dependent (i.e., depending on time with respect to the transmission pulse). Therefore, this dynamic relationship was established in 13 successive nonoverlapping zones, each 8 mm in depth, thus yielding 13 look-up tables. Correction was carried out by dividing the sampled amplitudes of the rf lines by the amplification factor corresponding to the steering voltage value recorded for that sample in the current depth zone.

3.2   Measurement of the diffraction spectrogram

The average transfer function $D^2(f, z)$ due to diffraction and focussing was measured by estimating the spectra of the echo signals from a tissue-mimicking phantom at a range of depths. The phantom consisted of degassed water in which 5 percent gelatin was solved at 60°C. A powder consisting of fine carbon particles was stirred through the gelatin solution after which it was allowed to congeal during continuous slow rotation for 6 hours. The density of scatterers was approximately $10^5/cm^3$, and the attenuation coefficient was (0.15 ± 0.02) dB/cm.MHz.

The phantom was placed in a tank filled with degassed water at room temperature, and for every depth the transducer was repositioned in such a way that the recorded echo signals came from the same volume in the phantom, just below the top surface
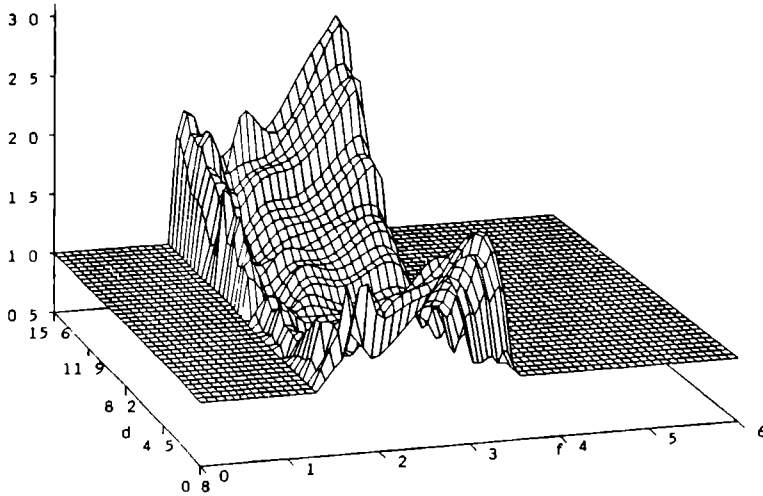
Figure 4: *The inverse of the diffraction amplitude spectrogram relative to the spectrum at the focal distance, which is used for the correction for the depth dependent sound beam properties. d = distance to the transducer in cm, f = frequency in MHz.*

(figure 3). To prevent disturbances caused by multiple reflections in the water tank the electronics of the scanner was modified so that only one pulse was transmitted during each sector scanning motion of the transducer. The direction of propagation of the sound pulse was perpendicular to the top surface of the phantom.

For each depth 100 independent rf lines were recorded by moving the transducer in a plane parallel to the top surface of the phantom. This procedure was repeated 38 times each time increasing the distance between the transducer and the sampling volume in the phantom by 4 mm.

From the recorded rf signals a time-gated segment of 128 samples, corresponding to 8 mm of depth, was selected just beyond the surface reflection of the phantom for each of the depth ranges at which measurements were taken. In this way the time-gated segments of consecutive depths overlapped by 50 percent. The amplitude spectra of the segments were calculated after multiplication with a Hanning window [17]. The 100 spectra corresponding to the 100 transducer positions were then ensemble averaged for each of the 38 depths. This yielded the spectrogram corresponding to equation (10). The spectra were then normalized with respect to the spectrum obtained for the focal zone, resulting in the correction spectrogram of equation (11), the inverse of which is shown in figure 4. Outside the usable bandwidth the filter values were made equal to 1. Correction of a 128-sample depth segment of a rf signal was performed by dividing its spectrum by the normalized spectrum of the filter corresponding to the same depth as explained in section 2.1. The influence on the sound beam caused by the water standoff (cf. fig. 3) was neglected. The attenuation at the acoustic path length within

the phantom, being the same for all distances z_i, was also neglected. In figure 4 the change in spectral shape with depth is clearly visible.

3.3   Computer Simulations

Computer simulated echograms were obtained by using the simulation program described in its preliminary form by Cloostermans [31] and in its definite form by Romijn et al. [32]. In the simulation program a tissue model was employed consisting of randomly positioned point scatterers in a homogeneously attenuating medium. The attenuation was modeled to be linear with frequency ($\alpha(f) = \beta f$) using the causal attenuation transfer function derived by Gurumurthy and Arthur [27], which was also applied for the correction for attenuation (see section 2.3). For the present application the scattering process was assumed to be frequency independent. The model was one-dimensional and sound beam effects of the transducer were not included. The transmitted pulse was modeled as having a Gaussian envelope. The centre frequency of the pulse was 3 MHz and the standard deviation of the (also) Gaussian amplitude spectrum of the pulse was 0.4 MHz. The simulated echograms each consisted of 50 completely independent rf lines, corresponding to a depth of 4 cm at a sound velocity of 1550 m/s. Simulations were performed with ten values of the attenuation coefficient inserted, ranging from 0.1 to 1.0 dB/cm.MHz. For each value of the attenuation coefficient 6 realizations were obtained, which sums up to a total of 60 simulated scans consisting of 50 independent rf lines each.

3.4   Phantom measurements

Using our data acquisition equipment, rf scans were recorded of a RMI tissue-mimicking phantom (Nuclear Associates). Several scans were taken at a number of depths of the region of interest and at a number of adjustments of the TGC. The manufacturer specified the attenuation coefficient of the phantom as 0.5 dB/cm.MHz. The phantom contained wires and holes, but these were carefully avoided, so that only rf data corresponding to homogeneous parts of the phantom were acquired.

3.5   Clinical Study

In this study we have examined patients as well as volunteers. The volunteers (group I, N=74, age: 30 ± 8), who were partly recruited from the personnel of our departments, were examined to obtain normal values of the parameters. Because the majority of these volunteers was between 17 and 33 years of age we additionally scanned a group of patients (group II, N=48, age: 46 ± 16), most of which were older than 33. The patients in this group were in general referred to the Radiology Department for an echographic examination of their kidneys, on suspicion of kidney stones or dilatation of the pelvic system. Both the volunteers and the patients in these groups did not have a history of liver disease, had only minimal intake of alcohol and there were no clinical signs of liver disease. All these volunteers and patients had an echographic liver examination following standard procedures, during which no liver pathology was assessed.

A third group consisted of patients having a liver pathology (group III, N=39, age: 50 ± 14). Several kinds of cirrhosis proved by biopsy were included in this group such as cirrhosis caused by alcoholic abuse, cirrhosis on basis of chronic hepatitis and primary

biliary cirrhosis. Also patients suffering from storage diseases, Wilson's disease and haemochromatosis, were included.

With our measurement equipment at least 8 independent ROI's from each patient, or volunteer, were selected and recorded. The scanning was usually done subcostally and the ROI's were chosen in the right lobe of the liver. During the selection of the ROI's care was taken to choose only homogeneous parts of the liver and to avoid strong reflections, caused by for example large blood vessels, as well as possible. The size of the ROI could be changed if neccessary, but in general the largest scans possible were taken. After positive visual assessment of the frozen image and when no substantial overflow was detected, the rf signals were stored in the computer.

3.6   Processing of the rf signals

The analysis of every recorded rf scan was started with the detection of segments where the signals caused overflow of the transient recorder, and segments where the signals were to weak to be properly analyzed. This detection was performed in 128-sample depth segments that overlapped by 50 percent. Remaining relatively strong reflections and relatively low echo areas were detected by comparing the signal power in every depth segment of each rf line with the power in that depth segment ensemble averaged over all the rf lines in the ROI. During the calculation of the ensemble averaged power, the segments containing overflow and the segments with a signal that was too weak were omitted. Segments with a signal power larger than 1.75 times and lower than 0.25 times the average power at the same depth were detected. These factors were experimentally established by visually comparing the marked regions with the reconstructed B-mode image for 200 scans of the liver. All the segments that were marked were left out of the analysis. If more than 20 percent of the segments was marked the ROI was not further analyzed.

After the rf signals were corrected for the TGC the estimates of the attenuation coefficient were obtained using the methods described in section 2.2. Then the envelope was calculated after the depth dependencies caused by attenuation and the properties of the sound beam were corrected for. The value of the attenuation coefficient estimated with the log-power decay method was used for the correction. The attenuation coefficient of the intervening liver tissue was assumed to be the same as that of the interrogated tissue. Correction for the attenuation in the intervening liver tissue was only performed for the distance beyond 5 cm from the transducer (z_0 in equations (18) and (19)). The intervening skin, subcutaneous fat and muscle tissues were assumed to fill a fixed range of 5 cm just beyond the transducer in all patients. It was assumed that the influences of these tissues on the echo signals were the same in all patients. They were not corrected for.

To prevent disturbance by system noise we additionally applied a band limiting spectral window function which smoothly caused the spectra to approach zero at 0.4 MHz and at 3.8 MHz. Finally, any remaining long-range trends in the echo amplitude due to inhomogeneity of the tissue were removed by correcting the envelope detected scan lines with a smoothed version of the ensemble averaged envelope. This detrending did not change the (global) average amplitude of the ROI.

4   Results

4.1   Simulations: Comparison Of Attenuation Estimation Methods

The five methods to estimate the frequency dependent attenuation coefficient that
were described in section 2.2 were tested and compared using the simulated rf data
described in section 3.3. Because beam properties were not included in the simulated
model, the diffraction correction was omitted in this case. For each simulated rf scan
consisting of 50 independent lines the attenuation coefficient was estimated. The results
are shown in figure 5 in which the average value of the estimated attenuation coefficient
minus the value inserted in the simulations is displayed as a function of the inserted
value. The error bars represent one standard deviation calculated from 6 realizations.
These figures show that the accuracy with which the attenuation coefficient was esti-
mated does not depend on its absolute value. This result is in accordance with equation
(16).

In table 1 the properties of the estimation methods are summarized. It shows the
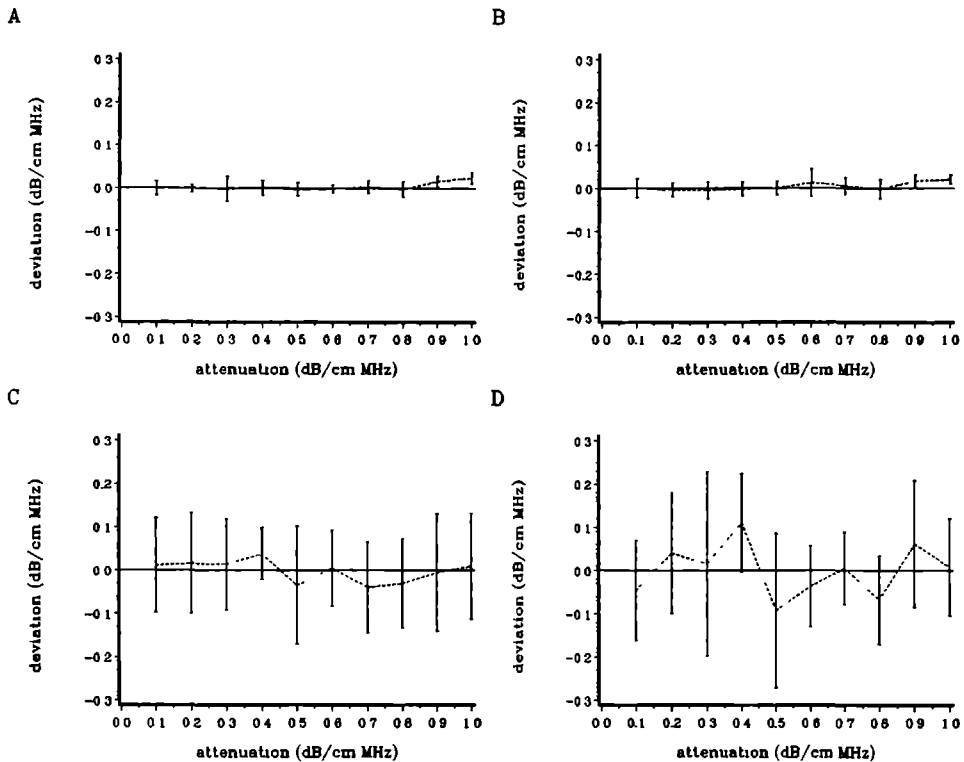

Figure 5: *The difference between estimated and true (i.e., simulated) attenua-
tion coefficient for estimation methods: a) LPD, b) MNB_0, c) CFS, d) $MNB\text{-}\alpha_1$
(section 2.2). Bars indicate $\pm$ one standard deviation.*

method	parameter	est$-$true	s	$\bar{s}$	$\bar{s}_t$
LPD	β	0.003	0.017	0.036	0.011
CFS	β	-0.002	0.104	0.23	0.07
MNB$_0$	β	0.004	0.020	0.009	0.015
MNB	α_0	0.03	0.41	0.21	0.17
	α_1	-0.01	0.15	0.08	0.07
	$\alpha(\overline{f})/\overline{f}$	0.004	0.023		
MNB$_p$	α_p	0.09	0.27	0.08	0.06
	n	-0.11	0.53		$0.166/\alpha(\overline{f})$
	$\alpha(\overline{f})/\overline{f}$	0.01	0.02		

Table 1: *The average difference between the estimated and true attenuation parameters, the standard deviation of this difference (s), and average standard deviation (s̄) of the estimate obtained from the fitting procedure using one scan (precision). Averging was performed over 60 simulated scans. In the last column the theoretical value of the precision is given.*

average values of the differences between the estimated and the true value of the attenuation coefficient ($\alpha_{est} - \alpha_{true}$) and the standard deviation of this difference. Also shown is the standard deviation obtained per scan from the fitting procedure, using the 50 rf lines each scan consists of, averaged over all 60 simulations ($\bar{s}$).

The log-power decay (LPD) method as well as the multi-narrowband method using a frequency fit with zero intercept (MNB$_0$) yielded accurate estimates of the true value of the attenuation coefficient. The bias, estimated by the average deviation from the true value, was small 0.003 $\pm$ 0.020 dB/cm.MHz for both methods. The standard deviation per scan (using the 50 independent rf lines per scan) was also small, 0.036 and 0.009 dB/cm.MHz respectively.

The centroid frequency shift (CFS) method yielded a smaller overall bias but the accuracy and precision of a single estimation were bad. A larger number of scans is needed to obtain a reliable average value of the attenuation coefficient. The standard deviation of the difference between estimated and true value was a factor five larger than with the MNB$_0$ and LPD methods.

The remaining two multi-narrowband methods, the first using the frequency fit without the intercept forced to zero (MNB) and the second using the exponential fit (MNB$_p$), are less accurate methods because two parameters are to be found from the fitting procedures. For the MNB method the average deviation of the intercept α_0 from zero, which was inserted in the simulation, was 0.03 $\pm$ 0.41 dB/cm. The average difference between the estimated and the true value of the slope of the attenuation coefficient was equal to -0.01 ± 0.15. The precision per scan was not high: $\bar{s}_{\alpha_0} = 0.21$ and $\bar{s}_{\alpha_1} = 0.08$. For the MNB$_p$ method the coefficient α_p was estimated with a bias of 0.09 $\pm$ 0.27 dB/cm.MHz and the exponent was on average underestimated $n = 0.90 \pm 0.53$. The precision using only one scan was low: $\bar{s}_\alpha = 0.08$ and $\bar{s}_n$ was dependent on the attenuation at the central frequency and ranged from 0.78 (theory: 0.66) at 0.1 dB/cm.MHz true attenuation to 0.08 (theory: 0.07) at 1.0 dB/cm.MHz true attenuation. When the inserted value of the attenuation coefficient was below 0.3 dB/cm.MHz the errors in α_p and n became

method		CFS	MNB$_0$	MNB			MNB$_p$		
				α_0	α_1	$\alpha(\bar{f})/\bar{f}$	α_p	n	$\alpha(\bar{f})/\bar{f}$
LPD	β	*	0.74	-0.36	0.46	0.44	-0.25	0.29	0.40
CFS	β		-0.35	*	*	-0.37	*	*	-0.32
MNB$_0$	β			*	*	0.86	*	*	0.81
MNB	α_0				-0.99	0.61	0.79	-0.73	0.91
	α_1					-0.51	-0.78	0.72	-0.51
	$\alpha(\bar{f})/\bar{f}$						0.51	-0.43	0.95
MNB$_p$	α_p							-0.91	0.55
	n								-0.48

Table 2: *Correlations of the attenuation coefficients estimated using 5 different methods ($p < 0.05$). An asterisk indicates that the correlation was not significant.*

very large. Although both methods allow more general information about the tissue to be obtained, more data are needed to reduce the variability of the results.

The latter two multi-narrowband methods both allow the estimation of a summary parameter. For the MNB method this summary parameter is $\alpha_{f_c} = (\alpha_0 + \alpha_1 f_c)/f_c$ and for the MNB$_p$ method it is $\alpha_{f_c} = (\alpha_p f_c^n)/f_c$. This latter parameter was also employed by Parker et al. [7]. These parameters which are also included in table 1 yielded accuracies and precisions which are comparable with the MNB$_0$ and LPD methods.

To find out whether the methods yielded independent estimates of the attenuation coefficient the correlation coefficients between the estimates of the methods was evaluated (Table 2). For this purpose we again first subtracted the true attenuation coefficient from the estimated value.

The most striking result is that the estimates of the CFS method, which is exclusively based on frequency information, was not highly correlated with those estimated with the other methods. Also the estimates of the LPD method, which uses amplitude information only, showed only a low correlation with the other methods except for the MNB$_0$ method (0.74). Of course, the coupled parameters α_0 and α_1 of the MNB method and α_p and n of the MNB$_p$ method showed high mutual correlations (-0.99 and -0.91, respectively). However, these parameters did not show high correlation with the estimates of the LPD, CFS and MNB$_0$ methods. The summary parameters of the MNB and MNB$_p$ methods introduced above and the estimate of the MNB$_0$ method also showed a high correlation. Since also the averages and standard deviations (Table 1) were the same these parameters are equivivalent. All three MNB methods utilize both amplitude and frequency information.

4.2   Performance Of Diffraction Correction Procedure

To test the methods used to correct for diffraction effects, attenuation and TGC, the rf data obtained from the RMI tissue-mimicking phantom (section 3.4) were used. The attenuation coefficient was estimated using the methods described in section 2.2. Figure 6 shows the estimated attenuation coefficient as a function of the distance of
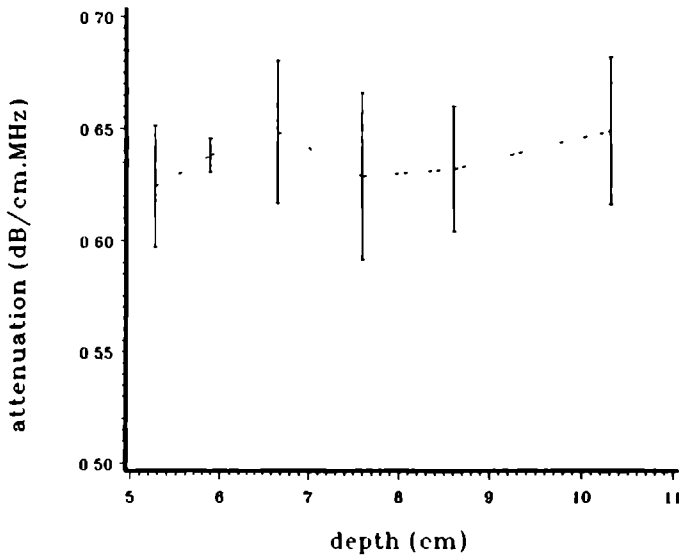
Figure 6: *The attenuation coefficient as a function of the depth of the ROI in the phantom. ROI size was 40 rf lines of 4 cm length. Bars indicate ± one standard error of the mean.*

the ROI to the transducer. An inadequate correction for the TGC or for the diffraction and focussing would have caused a depth dependence of the estimated attenuation coefficient. Since the estimated value showed no trend, and assuming that the tissue mimicking phantom was homogeneous, we may conclude from these measurements that the correction procedures yield satisfying results. The overall average of the estimated attenation coefficient is 0.63 dB/cm.MHz, which is higher than the value of 0.5 dB/cm.MHz specified by the manufacturer. This difference may be caused by aging of the phantom.

Figure 7 shows the full width at half maximum (FWHM) of the autocovariance function (section 2.4) in the axial direction for 4 situations: no corrections applied, correction for diffraction and attenuation, correction for diffraction only and correction for attenuation only. When no corrections were performed the FWHM increased until the focal zone and decreased beyond. When only diffraction correction was employed the FWHM in front of the focal zone was increased to the level at the focal distance, but beyond this distance a decrease was still present. When diffraction correction was omitted and only frequency dependent correction for the attenuation was applied the reverse holded. If both diffraction effects and the attenuation were corrected for an almost depth independent estimation of the FWHM was achieved. Since the deviations from the average value were smaller than the standard deviation of the estimate at each depth we may conclude that the corrections adequately remove the depth dependencies.

A

B

C

D
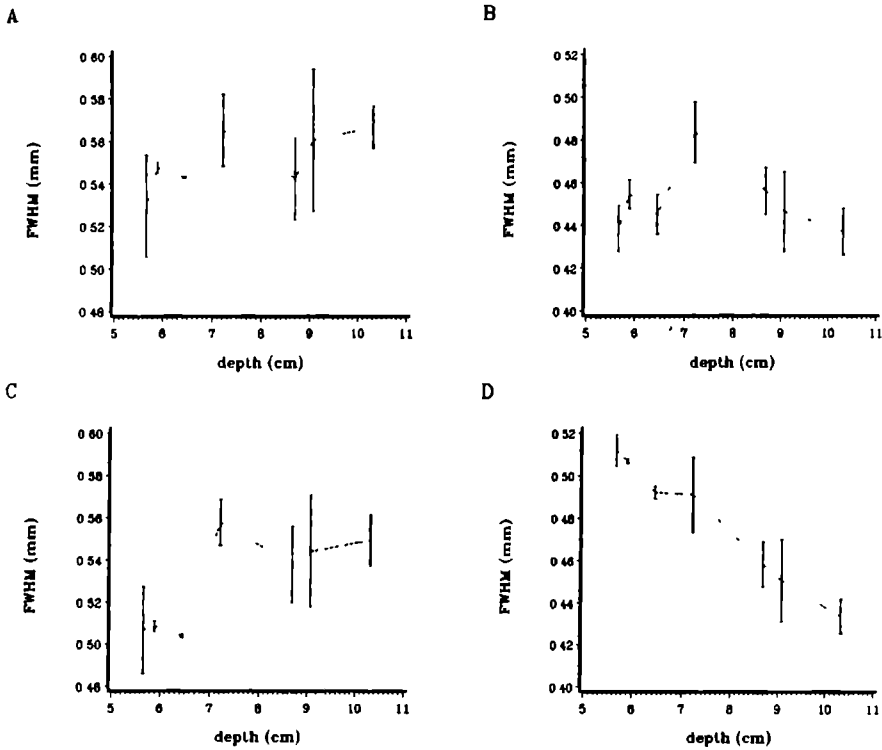
Figure 7: *The FWHM of the autocovariance function estimated from the enve-lope of the rf signals obtained from a tissue mimicking phantom. a) corrections for attenuation and diffraction effects, b) no corrections, c) correction for at-tenuation only, d) correction for diffraction only. Bars indicate $\pm$ one standard error of the mean.*

4.3   Reproducibility Of Clinical Measurements

4.3.1   Day rhythm variations

The influence of the biological diurnal rhythm on the measured parameters was inves-tigated. For this purpose we recorded the rf data of six volunteers during a number of sessions throughout one day:

- 8.30 In sober conditions, before breakfast

- 10.30 One hour after breakfast

- 12.00 One hour after coffee break

- 14.00 One and a half hour after lunch
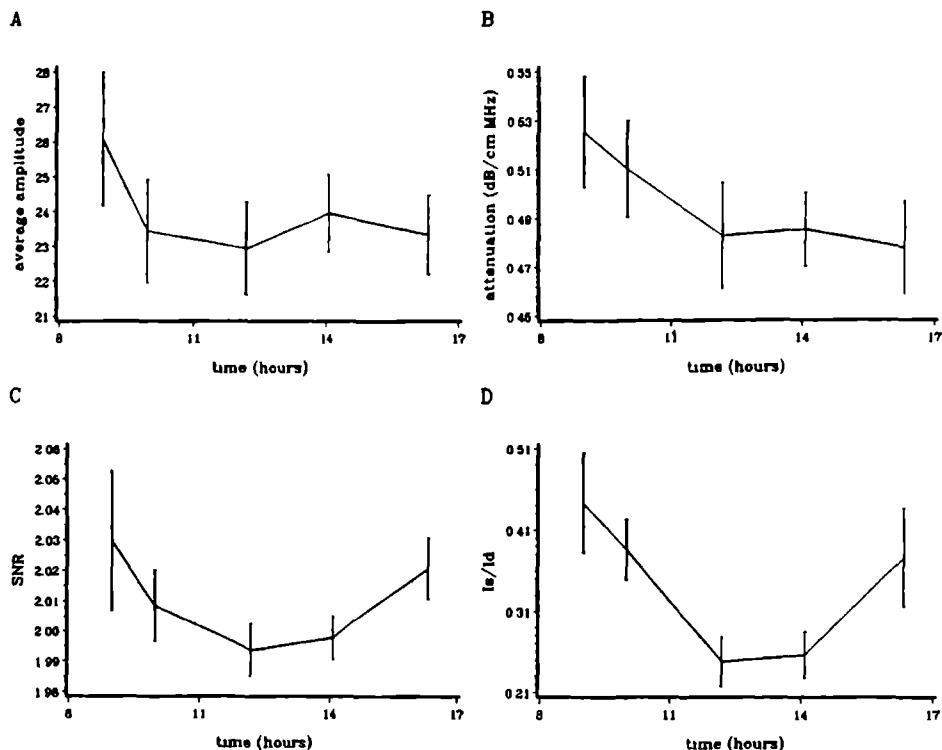
Figure 8: *The influence of the biological day rhythm on the value of the parameters. a) average amplitude, b) LPD-estimate of the attenuation coefficient, c) SNR, d) $\overline{I}_s/I_d$. The error bars indicate the interindividual variability ($\pm$ one standard error of the mean).*

- 16.00 Just after tea break

At least five regions-of-interest (ROI's) were recorded from the liver of every volunteer during each recording session. The ROI's taken were all kept at the same size and each time care was taken to record the ROI's at the same depth, to prevent influences of any remaining depth dependencies and influences caused by the inhomogeneity of the liver. The resulting parameters of each set of 5 ROI's were averaged.

Figure 8 shows four of these parameters as a function of the time during the day, averaged over the volunteers. It appeared that all parameters were influenced by the biological rhythm. The trends were approximately the same for every subject. The general trend was that the mean amplitude (Fig. 8a) decreased for one hour after breakfast and remained constant through the rest of the day. The attenuation coefficient (Fig. 8b) decreased till noon, after which it remained constant. The SNR (Fig. 8c) also decreased but rised again after lunch time. The same trend but more pronounced was found for $\overline{I}_s/I_d$ (Fig. 8d) and for $\sigma(I_s)/I_d$. As compared to the standard deviations, the changes
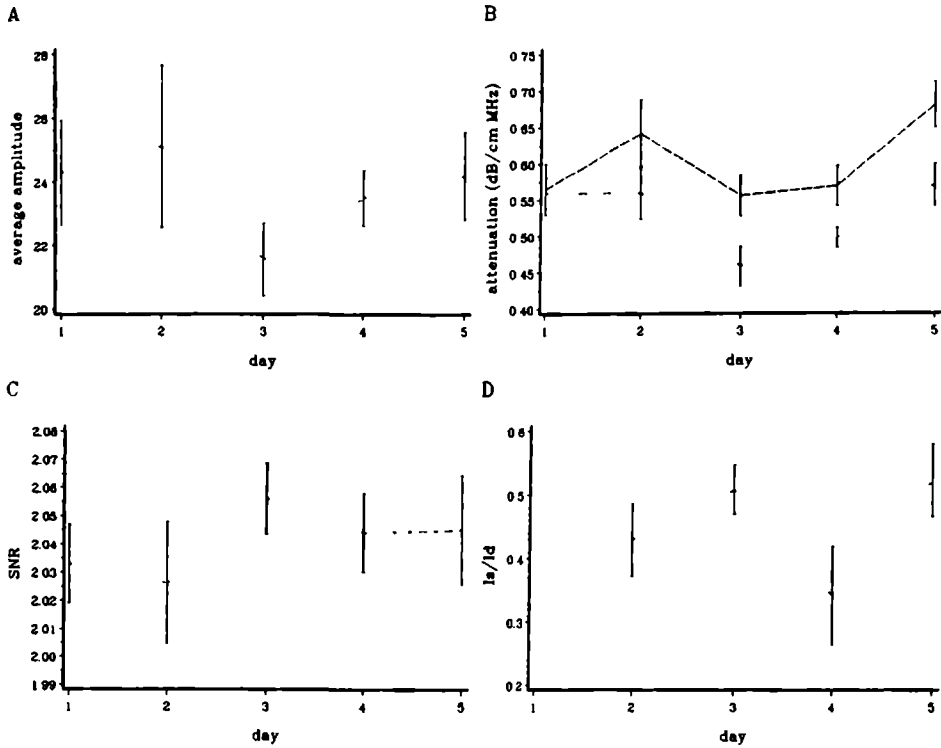
Figure 9: *The reproducability of the measurements over a 5 day period for a representative human subject a) average amplitude, b) attenuation coefficient (- - - = CFS, .. = LPD), c) SNR, d) $\bar{I}_s/I_d$. The error bars indicate ± one standard error of the mean.*

in the attenuation coefficient and the mean amplitude were small, but the variations in the SNR, $\bar{I}_s/I_d$ and $\sigma(I_s)/I_d$ were relatively large.

4.3.2 Day-to-day variations

For this experiment 4 volunteers were followed over a 5 day period. At each day liver scans were recorded in the same way as described in the previous section. There was one recording session each day at 16.00 hours, during which 6 scans were taken from each subject. Figure 9 presents the average values of four of the estimated parameters for a representative subject The error bars indicate one standard error. For most parameters differences between the mean values obtained at seperate days occurred which were larger than the standard error This means that there is a measurable variation in the state of the healthy liver tissue. Apart from the differences due to the inter-individual variability also this intra-individual variation contributes considerably to the spread of values within a population

4.4   Average Results Of Clinical Measurements

4.4.1   Attenuation estimates

The results of the attenuation analysis obtained from these three groups of human subjects are presented in table 3. This table includes the number of subjects and the average age of the subjects within the groups. For all the parameters and estimates the population average and the population standard deviation are presented. In addition, the results of a t-test for comparison between the groups are given. The average attenuation coefficient value found for the volunteers with a normal liver is in agreement with values reported in the literature [5,8,6]. The LPD, MNB_0 and the MNB (α_1) methods yielded approximately the same values. For the normal volunteers (first group) the averages were 0.49 ± 0.07, 0.50 ± 0.05, and 0.51 ± 0.11 dB/cm.MHz respectively. The differences between these methods were very small, although the MNB-α_1 parameter showed a spread which was twice that of the MNB_0 estimate. When the centroid frequency shift (CFS) method was used we obtained a value which was larger: 0.53 ± 0.08 dB/cm.MHz. The second group of subjects with a normal liver (patients) showed attenuation estimates which were on average higher than in the first group: 0.53 ± 0.07 dB/cm.MHz. However, the value obtained with the CFS method was lower: 0.50 ± 0.11 dB/cm.MHz. The results of the various estimation methods obtained for the group of patients with a diffuse liver disease were very consistent: 0.55 dB/cm.MHz. The spread in this group was, however, a factor 2 to 3 higher than in the normal liver groups. This caused a considerable overlap of the three groups.

In all three groups the zero intercept (α_0) of the MNB method was approximately zero, although a large spread was found. Large population standard deviations were also found for the two parameters obtained with the MNB_p method using the power law fit. The power was approximately the same for the three groups, and equaled 1.0. The parameter α_p was the same for the second normal liver group and the liver pathology

method		Volunteers		liverpathology	t-test		
		normals (I)	patients (II)	group (III)	$p > |t|$		
					I-II	I-III	II-III
N		74	48	39			
age		30 ± 8	46 ± 16	50 ± 14			
LPD		0.49 ± 0.07	0.53 ± 0.08	0.55 ± 0.19	0.001	0.06	
CFS		0.53 ± 0.08	0.50 ± 0.11	0.55 ± 0.13			
MNB_0		0.50 ± 0.05	0.53 ± 0.07	0.55 ± 0.17	0.010	0.06	
MNB	α_0	-0.03 ± 0.29	0.04 ± 0.32	-0.01 ± 0.39			
	α_1	0.51 ± 0.11	0.52 ± 0.14	0.55 ± 0.15			
MNB_p	α_p	0.52 ± 0.15	0.59 ± 0.14	0.59 ± 0.29	0.009		
	n	1.03 ± 0.22	0.96 ± 0.25	1.03 ± 0.26			

Table 3: *Averages of the attenuation parameters in each of the groups. The standard deviation of the parameter within the group is also given. The rightmost columns show the results of a t-test for comparison between the groups. Only values of p less then 0.10 have been reproduced.*

method		CFS	MNB$_0$	MNB		MNB$_p$	
				α_0	α_1	α_p	n
LPD		0.44	0.98	0.39	0.36	0.82	-0.32
CFS			0.61	-0.39	0.78	$*$	0.43
MNB$_0$				0.23	0.53	0.71	$*$
MNB	α_0				-0.71	0.82	-0.96
	α_1					-0.20	0.72
MNB$_p$	α_p						-0.76

Table 4: *Correlations of the attenuation parameters obtained using 5 different estimation methods ($p < 0.025$). An asterisk indicates that the correlation was not significant.*

group, but was lower in the first normal liver group. To reduce the large spread of the estimates of α_p and n, which was also found for the simulations, averaging the results of more independent scans would be needed for every patient. The cause of this large spread must be found in the attenuation model, with which more detailed information can be obtained at the cost of less precision, and in the relatively small bandwidth available.

The attenuation coefficient only showed a limited capability to discriminate the different clinical groups (table 3: t-test results). Using the LPD and MNB$_0$ estimates it was possible to significantly differentiate ($p < 0.06$) group I from group III. Using the same estimation methods also a significant difference ($p < 0.01$) was found between the two normal groups (I and II). It was however not possible to significantly differentiate group II from group III.

When comparing the estimation methods also the correlation coefficients should be considered. These were calculated for the pooled data, that is, for all three groups treated as a single group, and are presented in table 4. The results presented here confirm to a large extent the results of the simulations. Unlike the result found for the simulations a high correlation was found between the LPD estimate and the MNB$_p$-α_p parameter. Here also the CFS estimate correlated with the MNB-α_1 parameter.

It should be remarked that the correlation coefficients found for the simulations more accurately display the mutual dependence of the estimation methods, because the true attenuation coefficient was subtracted. In the in-vivo situation this was of course not possible since the true attenuation coefficient was not known. In this situation the correlation coefficients yielded higher values, although the estimation methods still may be independent to some extent.

4.4.2   Texture parameters

In table 5 the population averages and standard deviations of the parameters calculated from the corrected envelope signals (A-mode lines) are summarized. Also the t-test results for comparison between the groups are presented. All four parameters from the first order statistics appear to supply information about the condition of the interrogated tissues. The mean amplitude found in the group of liver patients was on average a factor

| method | Volunteers | | liver pathology | $p > |t|$ | | |
	normals (I)	patients (II)	group (III)	I-II	I-III	II-III
μ	25 ± 5	30 ± 9	55 ± 62	0.006	0.006	0.015
SNR	2.00 ± 0.05	$2\,02 \pm 0.06$	2.04 ± 0.06	0.002	0.03	
$\overline{I}_s/I_d$	0.37 ± 0.14	$0\,47 \pm 0.16$	0.55 ± 0.21	0.0001	0.0002	0.08
$\sigma(I_s)/I_d$	0.45 ± 0.06	0.50 ± 0.05	0.51 ± 0.06	0.0001	0.0001	
FWHM	0.45 ± 0.01	$0\,44 \pm 0.02$	0.44 ± 0.02			
$\overline{d}$	1.46 ± 0.36	$1\,45 \pm 0.38$	1.52 ± 0.38			

Table 5: *Averages of the texture parameters in each of the groups. The standard deviation of the parameter within the group is also given. The rightmost columns show the results of a t-test for comparison between the groups. Only values of p less then 0.10 have been reproduced.*

two higher (t-test: $p < 0.02$) than in the normal groups. The large spread, however, indicates the heterogenity of this group, probably caused by including several kinds of pathology. Also, the SNR values show considerable overlap, which resulted in less significant differences between the groups.

The parameters $\overline{I}_s/I_d$ and $\sigma(I_s)/I_d$, which characterize the properties of the structural and diffuse components of the scattered intensity showed on average significant differences (t-test: $p < 0.0002$) between groups I and II and between groups I and III. A wide overlap existed, however, between the liver pathology group (III) and the second normal liver group and to less extent the first normal liver group.

The second order texture parameters do not appear to represent information that can be usefull for the discrimination between the groups. The axial speckle size, characterized by the full width at half maximum (FWHM) of the axial autocovariance function yielded, on average, the same value in all three groups and showed only a small spread. The spread in the parameter $\overline{d}$, which characterized the distance between structured scatterers, was so large that the differences between the averages in the normal group and the liver pathology group appeared to be insignificant (t-test).

In table 6 the mutual correlations between the texture parameters are presented. The parameter $\overline{I}_s/I_d$ showed a high positive correlation with the SNR (0.83), which confirms the observations of Tuthill et al. [33] based on a simulation study. Mutually the two parameters representing structure, $\overline{I}_s/I_d$ and $\sigma(I_s)/I_d$, were also highly correlated (0.84).

	SNR	$\overline{I}_s/I_d$	$\sigma(I_s)/I_d$	FWHM
μ	*	*	*	*
SNR		0.83	0.53	-0.27
$\overline{I}_s/I_d$			0.84	*
$\sigma(I_s)/I_d$				0.21

Table 6: *Correlations of the texture parameters ($p < 0.025$). An asterisk indicates that the correlation was not significant.*

The other correlation coefficients were very small, indicating that the parameters are mutually independent.

To obtain the parameters $\overline{I}_s/I_d$ and $\sigma(I_s)/I_d$ the square root in equation (24) (section 2.4) had to be evaluated. The estimate of the argument of the square root was, however, sometimes negative, in which case no real solution exists. The number of recorded rf scans for which the square root could be evaluated expressed as a percentage of the total number of scans recorded for a patient is denoted by p_I. p_I was on average only 55 percent in the first normal liver group which means that for 45 percent of the scans the parameters $\overline{I}_s/I_d$ and $\sigma(I_s)/I_d$ could not be evaluated. In the other two groups p_I was larger: 72 percent in the second normal liver group and 79 percent in the liver patient group.

The number p_I correlated with the SNR (0.85) and with $\overline{I}_s/I_d$ (0.64), which means that, keeping in mind the results of Tuthill et al. [33], the chance of obtaining an estimation of the parameters $\overline{I}_s/I_d$ and $\sigma(I_s)/I_d$ increases if the strength of the structural component increases.

In only approximately 70 percent of the power spectra of the intensity obtained per patient significant peaks could be detected, which are supposed to indicate the distance between regularly spaced scatterers. This might be caused by the poor resolution of the echographic transmission pulse (0.75 mm). Another plausible explanation is that the structure was too irregular to be detected as such. Furthermore, the hexagonal cylindrical liver lobules are mostly not irradiated perpendicularly to the cylinder axes, which causes a large spread in distances between the structural scatterers as they are observed in the scan plane. The contribution of the structure is then distributed over more spatial frequencies and the peaks in the spectrum become too small to be detected.

4.4.3 Correlation between texture and attenuation parameters

Interaction processes between the ultrasound and the tissue exist, which influence both attenuation and texture properties. If the strength of the scattering, which is the most important process, increases, the mean amplitude and the attenuation coefficient are increased as well. This was observed, for example by Garra et al. [6], in livers with steatosis (bright liver). Therefore, the attenuation coefficient and the mean amplitude correlate although the envelope signals were corrected for the (frequency dependent) attenuation. Table 7 shows the correlation coefficients (> 0.15) between the attenuation estimates and the first and second order texture parameters. Indeed the mean amplitude showed positive correlation to the estimates of the attenuation coefficient based on amplitude information (LPD) and to a less extent to the estimates based on mixed frequency-amplitude information, obtained with the MNB methods. The estimates

method	LPD	CFS	MNB_0	MNB		MNB_p
				α_0	α_1	α_p
μ	0.68	0.36	0.66	0.25	0.25	0.57
FWHM	-0.40	-0.33	-0.44	-0.16	-0.18	0.33

Table 7: *Mutual correlations (> 0.15) between texture and attenuation parameters ($p < 0.025$).*

obtained from the CFS method showed only a low correlation with the mean amplitude.

The second order texture parameter FWHM showed a small negative correlation with the attenuation estimates, which must be attributed to insufficiencies in the correction methods.

All correlation coefficients not shown in table 7 were smaller than 0.15.

5   Discussion

It has been well established that in order to obtain a depth independent estimate of the attenuation and scattering parameters corrections have to be carried out for the ultrasonic beam properties. It was investigated to which extent these beam properties influenced the texture of the B-mode images [4]. In an attempt to correct the images by a deconvolution with the two dimensional rf point spread function it was found to be only feasible if certain system requirements are fulfilled [26]. In practice these requirements are usually not met and, therefore, several other methods have been tried which are less complicated. For example, Morris et al. [12] carried out corrections on the estimated parameters using a look-up table for each parameter which was established using the parameters of the whole population averaged at each depth. Zuna et al. [15] corrected the images themselves, but when using their method only the mean amplitude becomes depth independent, provided the appropriate TGC correction was applied. The problem with these methods is that in order to obtain a depth independent texture also the influence of the attenuation has to be taken into account. Although the TGC of the ultrasound scanner was used to correct the amplitude decay, the influences on the second order statistical properties of the texture were not corrected for in the latter two papers.

Using the method presented in section 2.3 we were able to correct to a great extent the depth dependencies of the B-mode texture, with respect to the first order and axial second order statistical properties. The obtained estimates of the texture parameters are, however, not device independent because the transmission pulse properties were not removed by deconvolution, but only a correction was applied relative to the focal zone to yield depth independece. The method can be further refined if the distance z_0 (cf. Eqs. (18) and (19)) is specified for each seperate scan and a correction is carried out for the attenuation in the intervening muscle and skin tissues. Correction for the influence of the sound beam and the attenuation on the lateral texture properties is still a subject of further investigations [34].

We have tested several attenuation estimation methods and several models for the frequency dependence of the attenuation coefficient. Nonlinearity of this dependence has been shown before to play a role only at higher ultrasound frequencies and when using a broadband transmission pulse [35]. We found that, using our equipment with its low central frequency transmission pulse and its relatively small bandwidth, it was practically impossible to significantly distinguish the frequency dependence of the attenuation coefficient from the linear $\alpha(f) = \beta f$ model. Three estimation methods (LPD, MNB_0 and CFS) were used which are based on the linear model. The estimates obtained with the CFS method, which is exlusively based on frequency information, were found to be independent of the estimates obtained using methods based on amplitude information (LPD and MNB_0). This result was also found by Tsao et al. [36] and Romijn

et al. [37]. All the methods are unbiased although averaging over independent scans is needed to obtain sufficient precision. In the simulation study the CFS method yielded a population standard deviation which was five times larger than for the LPD and MNB_0 methods. This difference was not found in the clinical study.

Although the methods were designed to estimate the attenuation coefficient, the estimation results may be influenced by other properties of the interrogated tissue than the attenuation. The extent to which this happens, however, is dependent on the estimation method. The CFS method, for example, is influenced by the frequency dependence of scattering [32]. The allowance of a nonzero intercept for the frequency dependence of the attenuation coefficient (MNB method) has been indicated to take the presence of specular scatterers and reflectors into account [38]. It should therefore be remarked that the testing of the methods using simulated rf data with a linear frequency dependence of the attenuation coefficient does not exclude any method from being usefull for the in-vivo situation.

The attenuation coefficient showed a limited capability to discriminate the different clinical groups. Only by using the LPD and MNB_0 estimates it was possible to significantly differentiate the normal livers of a relatively young group of healthy volunteers (group I) from pathologic livers (group III). Using the same estimation methods also a significant difference was found between group I and an older group of patients who were assumed to have a healthy liver (group II). It was however not possible to significantly differentiate group II from group III. The estimates of both methods show a high mutual correlation, so that it is not advisable to use more than one of these methods in a discriminant analysis. The CFS method did not yield estimates of the attenuation which could significantly differentiate the clinical groups mentioned above. The large standard deviations obtained for the liver pathology group (III) may be attributed to the inclusion of several kinds of pathology. The discriminating power might be improved by a subclassification of this group.

In this study we have limited ourselves to only a few statistical texture parameters that can be related to physical properties of the examined tissues, such as the scattering strength (μ), the density of scatterers $(\mu$, SNR, FWHM) [4] and the relative strength of the structural and random scattering $(\overline{I}_s/I_d, \sigma(I_s)/I_d, $ SNR) [16,29,33] and the average distance between structured scatterers [11]. Other (ad hoc) statistical measures which may also yield discriminating power [9,10,12] can be estimated from the texture, but were not used in this study. We have only found significant discriminating power $(p < 0.05)$ for the first order statistical texture parameters $(\mu$, SNR, $\overline{I}_s/I_d, \sigma(I_s)/I_d)$. The mean amplitude (μ) was approximately a factor two higher in pathologic livers as compared to healthy livers. The spread in values found in group III was, again, very large due to the heterogeneity of this group. When using the SNR, $\overline{I}_s/I_d$, and $\sigma(I_s)/I_d$ significant differences were found between groups I and II and between groups I and III. These parameters, however, showed a relatively high mutual correlation. All three parameters were increased in case of liver pathology, which would mean that an increase in structural scattering is present. The dependence of the SNR on structural scattering was investigated by Tuthill et al. [33]. These authors found a large increase of the SNR if the echoes from the structured scatterers positively interfered $(\overline{d} = n\lambda,$ with $n = 1, 2, \ldots$ and λ the wavelength).

The estimated average scatterer spacing $(\overline{d})$ is on average larger in the case of liver

pathology, but the spread in the values found in the three groups is so large that this parameter does not contribute any significant discriminating power. The only second order statistical parameter included in this study, was the axial speckle size characterized by the full width at half maximum of the axial autocovariance function (FWHM). This parameter was shown to be sensitive to changes in the density of scatterers [4] as long as the density remained below the Rayleigh limit set by the ultrasonic equipment. Since this parameter yielded approximately the same value in all three groups, the conclusion may be drawn that the density of scatterers was in general above the Rayleigh limit.

The spread in the estimated values was, next to the expected interindividual variability, shown to be caused by intraindividual variability. The estimates changed during the day due to the diurnal biological rhythm. Also estimates obtained on seperate days but at the same time of the day showed a variability. Nevertheless, the results presented in tables 3 and 5 indicate that a discrimination between normal livers and pathologic livers may well be possible. The results may improve if the heterogeneous liver pathology group can be subclassified based on biopsy results and other clinical findings. The differences found between groups I and II, both including human subjects with a healthy liver, may be attributed to the difference in average age. A further study on these subjects is performed at present. The inability to differentiate group II from group III, which is caused by the wide overlap in parameter values between the groups forces us to be reserved in drawing definite conclusions with respect to the applicability of these techniques prospectively in clinical routine.

References

[1] Cloostermans, M.J.T.M., and Thijssen, J.M., A beam corrected estimation of the frequency dependent attenuation of biological tissues from backscattered ultrasound, *Ultrasonic Imaging 5*, 136-147 (1983).

[2] Cloostermans, M.J.T.M., Mol, H., Verhoef, W.A., and Thijssen, J.M., In vitro estimation of acoustic parameters of the liver and correlations with histology, *Ultrasound in Med. and Biol. 12*, 39-51 (1986).

[3] Verhoef, W.A., Cloostermans, M.J.T.M., and Thijssen, J.M., Diffraction and dispersion effects on the estimation of ultrasound attenuation and velocity in biological tissues, *IEEE Trans. Biomed. Eng. 32*, 521-529 (1985).

[4] Oosterveld, B.J., Thijssen, J.M., and Verhoef, W.A., Texture of B-mode echograms: 3-D simulations and experiments of the effects of diffraction and scatterer density, *Ultrasonic Imaging 7*, 142-160 (1985).

[5] Taylor, K.J., Riely, C.A., Hammers, L., Flax, S., Weltin, G., Garcia-Tsao, G., Conn, H.O., Kuc, R., and Barwick, K.W., Quantitative US attenuation in normal liver and in patients with diffuse liver disease: Importance of fat, *Radiology 160*, 65-71 (1986).

[6] Garra, B.S., Insana, M.F., Shawker, T.H., and Russell, M.A., Quantitative estimation of liver estimation and echogenicity: normal state versus diffuse liver disease, *Radiology 162*, 61-67 (1987).

[7] Parker, K.J., Asztely, M.S., Lerner, R.M., Schenk, E.A., and Waag, R.C., In-vivo measurements of ultrasound attenuation in normal or diseased liver, *Ultrasound in Med. and Biol. 14*, 127-136 (1988).

[8] Garra, B.S., Shawker, T.S., Insana, M.F., and Wagner, R.F., In vivo attenuation measurement methods and clinical relevance, in *Ultrasonic Tissue Characterization and Echographic Imaging 6*, J.M.Thijssen and G.Berger, eds. (Commission of the EC, Luxembourg, 1987).

[9] Raeth, U., Schlaps, D., Limberg, B., Zuna, I., Lorenz, A., Van Kaick, G., Lorenz, W.J., and Kommerell, B.K., Diagnostic accuracy of computerized B-scan texture analysis and conventional ultrasonography in diffuse parenchymal and malignant liver disease, *J. Clinical Ultrasound 13*, 87-89 (1985).

[10] Nicholas, D., Nassiri, D.K., Garbutt, P., and Hill, C.R., Tissue characterization from ultrasound B-scan data, *Ultrasound in Med. and Biol. 12*, 135-143 (1986).

[11] Insana, M.F., Wagner, R.F., Garra, B.S., Brown, D.G., and Shawker, T.H., Analysis of ultrasound image texture via generalized Rician statistics, *Opt. Eng. 25*, 743-748 (1986).

[12] Morris, D.T., An evaluation of the use of texture measurements for the tissue characterization of ultrasonic images of in vivo human placentae, *Ultrasound in Med. and Biol. 14*, 387-395 (1988).

[13] Insana, M.F., Improvements in the spectral difference method for measuring ultrasonic attenuation, *Ultrasonic Imaging 5*, 331-345 (1983).

[14] Fink, M.A., and Cardoso, J.F., Diffraction effects in pulse-echo measurement, *IEEE Trans. Sonics Ultrason. SU-31*, 313-329 (1984).

[15] Zuna, I., Volk, J., Raeth, U., Schlaps, D., Naves, W., Lorenz, A., Lorenz, D., Van Kaick, G., and Lorenz, W.J., TC-System influence on the B-mode image features, in *Ultrasonic Tissue Characterization and Echographic Imaging 6*, J.M.Thijssen and G.Berger, eds. (Commission of the EC, Luxembourg, 1987).

[16] Wagner, R.F., Insana, M.F., and Brown, D.G., Unified approach to the detection and classification of speckle texture in diagnostic ultrasound, *Opt. Eng. 25*, 738-742 (1986).

[17] Oppenheim, A.V., and Schafer, R.W., *Digital Signal Processing* (Prentice-Hall, Englewood Cliffs, 1975).

[18] Kuc, R. and Schwartz, M., Estimating the acoustic attenuation coefficient slope for liver from reflected ultrasound signals, *IEEE Trans. Sonics Ultrason. SU-26*, 353-362 (1979).

[19] Kak, A., and Dines, K.A., Signal processing of broad band pulsed ultrasound: measurement of attenuation in soft biological tissues, *IEEE Trans Biomed. Eng. BME-25*, 321-344 (1978).

[20] Kuc, R., Schwartz, M., and Von Micsky, L., Parametric estimation of the acoustic attenuation coefficient slope for soft tissue, in *IEEE Ultrasonics Symposium Proceedings*, IEEE Cat. No. 76 CH11200-SSU, 44-47 (1976).

[21] Fink, M., Hottier, F., and Cardoso, J.F., Ultrasonic signal processing for in vitro attenuation measurement: short time Fourier analysis, *Ultrasonic Imaging 5*, 117-135 (1983).

[22] Shaffer, S., Pettibone, D.W., Havlice, J.F., and Nassi, M., Estimation of the slope of the acoustic attenuation coefficient, *Ultrasonic Imaging 6*, 126-138 (1984).

[23] Kuc, R., Bounds on estimating the acoustic attenuation of small tissue regions from reflected ultrasound, *Proc. IEEE 73*, 1159-1168 (1985).

[24] Parker, K.J., Attenuation measurement uncertainties caused by speckle statistics, *J. Acoust. Soc. Am. 80*, 727-734 (1986).

[25] Berger, G., Laugier, P., Fink, M., and Perrin, J., Optimal precision in ultrasound attenuation estimation and application to the detection of Duchenne muscular dystrophy carriers, *Ultrasonic Imaging 9*, 1-17 (1987).

[26] Jeurens, T.J.M., Somer, J.C., Smeets, F.A., and Hoeks, A.P.G., The practical significance of two-dimensional deconvolution in echography, *Ultrasonic Imaging 9*, 106-116 (1987).

[27] Gurumurthy, K.V., and Martin Arthur, R., A dispersive model for the propagation of ultrasound in soft tissue, *Ultrasonic Imaging 4*, 355-377 (1982).

[28] Whalen, A.D., *Detection of Signals in Noise* (Acad. Press, New York, 1971).

[29] Wagner, R.F., Insana, M.F., and Smith, S.W., Fundamental correlation lengths of coherent speckle in medical ultrasonic images, *IEEE Trans. Ultrason. Ferroel. Freq. Contr. UFFC-35*, 34-44 (1988).

[30] Kruimer, W.H., Lammers, J.H.E., and Thijssen, J.M., Ultrasonic Biopsy Apparatus, in *Acoustical Imaging 14*, A.J.Berkhout, J.Ridder and L.F.van der Wal, eds. (Plenum Press, New York, 1985).

[31] Cloostermans, M.J.T.M., A-scan simulation program, in *Ultrasonic Tissue Characterization and Echographic Imaging 3*, J.M. Thijssen and K. Irion, eds. (Faculty of Medicine Printing Office, Nijmegen, 1984).

[32] Romijn, R.L., Thijssen, J.M., and Van Beuningen, G.W.J., Estimation of scatterer size from backscattered ultrasound: a simulation study, *IEEE Trans. Ultrason. Ferroel. Freq. Contr. UFFC-36*, (in press).

[33] Tuthill, T.A., Sperry, R.H., and Parker, K.J., Deviations from Rayleigh statistics in ultrasonic speckle, *Ultrasonic Imaging 10*, 81-89 (1988).

[34] Thijssen, J.M., Oosterveld, B.J., and Fabel, R., Diffraction correction: the lateral point of view, *Ultrasonic Imaging 11*, 129-130 (1989).

[35] Lin, T., Ophir, J., and Potter, G., Frequency dependent ultrasonic differentiation of normal and diffusely diseased liver, *J. Acoust. Soc. Am. 82*, 1131-1138 (1987).

[36] Tsao, J.W., Morimura, S., Itoh, H., Itoh, I., and Konishi, T., Comparisons of images derived from amplitude, mean frequency and attenuation coefficient of pulse echo signals, *Jpn. J. Med. Ultrasonics 14*, 393-406 (1987).

[37] Romijn, R.L., *On the quantitative analysis of ultrasound signals and applications to intraocular melanomas*, Thesis, (University printing office, Nijmegen, 1989).

[38] Laugier, P., Berger, G., Fink, M., and Perrin, J., Specular reflector noise: effect and correction for in-vivo attenuation estimation, *Ultrasonic Imaging 7*, 277-295 (1985).

Appendix

Ultrasound Attenuation and B-mode Texture Analysis of Diffuse Liver Disease: Clinical Results

In section 4 of chapter VII each parameter was separately tested for its ability to discriminate between groups of healthy volunteers and a group of patients having a diffuse liver pathology. Some parameters yielded large standard deviations within the liver pathology group because several diseases were included in this group. In this appendix the preliminary results are presented of the use of combinations of the parameters to discriminate between the healthy livers and the different disease groups. The discrimination was performed by a discriminant analysis, based on a subset of the best parameters. This subset was established by a parameter selection procedure.

1 Discriminant analysis

For each patient and volunteer all the estimated parameters were averaged over the series of recorded scans. The n averaged parameters span an n-dimensional space, in which each subject takes a position defined by the parameter vector $\vec{p} = (p_1, ...p_n)$. If (some of) the parameters contain specific information about the condition of the liver, then this position will be dependent on that condition. The idea now is that the parameter vectors of livers with a similar condition will cluster in this space. It may then well be possible that these clusters can be separated in the n-dimensional parameter space, although they cannot be separated by considering the parameters individually.

To simplify the situation the n-dimensional problem is reduced to a one dimensional problem by projecting all vectors $\vec{p}$ on a line, reducing $\vec{p}$ to its projection y on that line. Fisher's linear discriminant analysis [1,2] is a procedure for finding the projection line on which the clusters are optimally separated. This projection line is called the "discriminant function". The histogram of y that belongs to cluster A then has the least overlap with the histogram of y that belongs to cluster B. The histograms are characterized by their means m_1 and m_2 and standard deviations σ_1 and σ_2, respectively. The discriminating power then may be expressed by the normalized distance between the means

$$d' = \frac{|m_1 - m_2|}{\sqrt{\sigma_1^2 + \sigma_2^2}}.$$ (1)

The classification rule which is based on the discriminant function is then to allocate each patient or volunteer to the group with the maximum posterior probability as estimated from the histograms of y:

choose A if $p(y|A) > p(y|B)$
choose B if $p(y|A) < p(y|B)$.

The probability of a correct classification was estimated by using the "Leaving-One-Out" method (also: "Round-Robin" method, "Jackknife" method) [3,2]. This method proceeds as follows. Take one subject out of the data base and apply the Fisher discriminant analysis to the remaining subjects. Then compute the projection y of the left out vector $\vec{p}$ on the found discriminant function and apply the classification rule. If the subject is correctly classified to the appropriate group, add 1 to the number of subjects correctly classified in this group. Repeat this procedure for all the subjects in the data base. The probability of correct classification can then be estimated from the fractions of correctly classified subjects in groups A (true positive fraction, sensitivity) and B (true negative fraction, specificity). From these values an overall probability for correct classification can be estimated, that corresponds to the area A under the ROC curve [4].

2   Parameter selection

If a number of parameters is available then some of these may be useless, i.e., they do not discriminate between the groups. Other parameters that are good discriminators may be highly correlated, in which case they contribute with the same information when they are combined in the discriminant analysis. Because the nondiscriminating parameters and the highly correlated parameters do not contribute to the discrimination, and even may introduce noise, it is better to leave these out.

To prevent substantial errors in estimating the performance of the discriminant analysis the number of parameters used in the analysis should not be larger than one third of the number of subjects in the smallest group. This rule is often refered to as the "Foley-criterion" [5] and provides another argument for selecting a subset of parameters for the discrimination task.

Parameter selection is a procedure to select those parameters that, when combined, yield the best discrimination. The method that was used to perform this selection is called the "stepwise parameter selection technique" [2]. This method selects the parameters one at a time, starting with the best one, until no significant improvement is obtained in the discriminating ability. First, the discriminating ability of each single parameter is estimated using the method described above. An F-test was used to measure the discriminating ability at a specified statistical significance level. The selection of the best set of parameters is started by choosing the best parameter. Then, from the remaining parameters, the second parameter is chosen as the one that yields the largest increase in discriminating ability, when combined with the first parameter. This procedure is repeated until no parameters can be added, such that the F-values exceed the statistical significance level. At each step, each already selected parameter is again tested for its contribution to the discrimination and if the significance level to keep the parameter is not reached, it is removed from the selection.

The selection of the parameters and the estimation of the probability of correct classification are based on the a priori knowledge of the group that each subject belongs to. Once, from a sufficiently large data base, a selection of parameters is made and

based on these a discriminant function is obtained, it is possible to use the classification rule prospectively.

3   Results

The liver pathology group was subdivided in a number of disease groups based on prior clinical findings and biopsy results. We investigated the performance of the discrimination task between the normal group and each disease group. Only the results of the groups consisting of more than 5 patients are presented in table 1. The following disease groups were established: hepatitis, cirrhosis, alcoholic cirrhosis and Wilson's disease. Furthermore we also show the results of groups of patients with steatosis and metastasis.

In addition to the parameters discussed in chapter VII several other parameters were available, which could be used as diagnostic parameters. These were: the average of the intensity, μ_I, the signal-to-noise ratio of the intensity: SNR_I and the number of significant peaks detected in the power spectrum of the intensity: n_d.

It appeared that the stepwise selection procedure produced subsets of parameters which were not the same for each task. Table 1 presents the selected parameters for each task and the discrimination results The statistical significance level for the F-test employed for the selection procedure was set to 0.15. The values of d' and A, the area under the ROC curve, were estimated from the sensitivities and specificities obtained for each task from the Leaving-One-Out procedure. Since the number of patients in each disease group is small the accuracy of the estimation of the performance of the discrimination may not be very high.

We also examined a group of 30 patients suffering from cystic fibrosis. Of these patients 7 had cirrhosis and 23 did not, based on prior clinical knowledge. With our analysis we could discriminate these two groups of cystic fibrosis patients with an accuracy of $A = 84.3$ ($d' = 1.42$).

task: normal vs.	N	parameters	d'	A
hepatitis	9	$\mu_I, \beta_{MNB_0}, \alpha_p$	2.24	94
cirrhosis	6	μ, n_d	1.75	89
alcoholic cirrhosis	10	μ_I, SNR_I, μ	1.23	81
Wilson's disease	5	μ_I, α_1, n_d	1.67	83
steatosis	9	$\mu_I, SNR_I, \beta_{CFS}$	2.98	98
metastasis	5	μ_I, β_{CFS}	1 90	91

Table 1: *Results of the discriminant analysis between healthy livers (N =88) and diseased livers. The number of patients in each of the disease groups is indicated by N. The parameters selected by the stepwise parameter selection technique are presented as well as the probability of correct classification as indicated by the area A under the ROC curve.*

4   Conclusions

For the differentiation of diffuse liver disease by using ultrasound, the radiologist uses parameters such as the size of the liver, the visibility and size of the major bloodvessels and a visual interpretation of the texture with which the organ is displayed in the B-mode scan. The results presented indicate that the quantitative analysis of echo signals may prove to be a usefull additional tool for the diagnosis of diffuse liver diseases. However, more independent parameters with a good diagnostic ability will be needed to be successful in the differentiation among the various diseases. The data of more patients within each of the disease groups will be needed to draw definite conclusions with respect to the prospective value of the discussed methods.

References

[1] O'Duda, R., and Hart, P.E., *Pattern Classification And Scene Analysis* (John Wiley, New York, 1973).

[2] Albert, A. and Harris, E.K., *Multivariate Interpretation of Clinical Laboratory Data* (Marcel Dekker, New York, 1987).

[3] Lachenbruch, P.A., An almost unbiased method for obtaining confidence intervals for the probability of misclassification in discriminant analysis, *Biometrics 23*, 639-645 (1967).

[4] Green, D.M., and Swets, J.A., *Signal Detection Theory and Psychophysics* (John Wiley, New York, 1966).

[5] Foley, D., Considerations of sample and feature size, *IEEE Trans. Inform. Theory 18*, 618-626 (1972).

Summary

During the last fifteen years much effort has been devoted to the quantitative analysis of echographic radiofrequency signals and echographic images. However, it was not until a deeper understanding of the physical phenomena of the sound propagation and the interaction of the ultrasound with the tissue was achieved, that some analysis methods yielded consistent results. An important problem that was addressed was the depth dependence of the estimation of the attenuation coefficient, which appeared to be caused by the diffraction and focussing of the sound beam. Methods were designed to correct the spectra corresponding to the radiofrequency signals for this influence, which greatly improved the reproducibility of the estimation. Another advantage was that the results became to great extent independent of the echographic equipment, which enabled the comparison of the results obtained by various research groups.

In this thesis the results are reported of a study to find and evaluate methods for the quantitative analysis of echographic signals for the differentiation of diffuse diseases and for the detection of focal lesions.

In the second chapter the influence of the diffraction and focussing effects on the texture of B-mode images corresponding to homogeneous tissues was investigated, using realistic computer simulations and measurements of a tissue-mimicking phantom. This texture is caused by interference at the surface of the transducer when receiving the echo signals and is called speckle. To characterize the speckle first and second order statistical texture analysis was used. We found that most of the estimated texture parameters were considerably depth dependent which was not only caused by the beam influence but also by the attenuation. Therefore, to obtain reliable and reproducible estimates of the texture characteristics, the rf signals that are underlying the images had to be corrected for these influences. In chapter VII a frequency dependent method is proposed and tested to correct the rf signals in such a way that depth independent estimates of the texture parameters are obtained. Only the axial direction was considered.

Another question that was addressed in chapter II was whether the speckle can reveal information about the tissue. This was investigated using computer simulated echograms of homogeneous scattering media having a varying number density of randomly positioned scatterers. It was found that all the estimated texture parameters were dependent on this density. However, in the limit of a high density of scatterers so-called "fully developed" speckle occurs in which case only the average echo amplitude remains dependent on the density of scatterers. The echo amplitude is then distributed according to a Rayleigh probability density function. In this limit of a high scatterer density the investigated second order texture parameters approached limit values set by the transducer characteristics.

In echographic equipment the phase information in the rf echo signals is discarded

when detecting the envelope of the rf signals prior to the production of the B-mode images. In chapters III through V we investigated the usefulness of the phase of the echo signals. The phase derivative, or instantaneous frequency, was used to produce a new kind of echographic images. Several methods were described to obtain a stabilized phase derivative (PD). The properties of the stabilized PD signals and the PD images which were characterized by first and second order statistical texture analysis, were found to depend on the stabilization method. This study was based on echo signals obtained from computer simulations and from experiments using a tissue-mimicking phantom as well as radiofrequency echograms obtained in vivo. In chapter V a theoretical derivation is presented of the first and second order texture parameters, taking into account the stabilization, and the subsequent rectification and low-pass filtering to produce the images. From the images obtained in simulations with a varying scatterer density it was found that the phase derivative did not at all provide any information about the scattering properties of the tissue in case of homogeneous and isotropic scattering. It may, however, be anticipated that the PD images may be used to assess the deviation from the scattering model when biological tissues are examined.

Several postprocessing curves to manipulate the grey levels of the B-mode images are made available in echographic equipment by the manufacturers. In chapter VI the question is addressed whether it is possible to improve the detection of focal lesions by using this facility. As a measure of the detectability of a lesion the so-called "lesion signal-to-noise ratio" was employed which measures the performance of an ideal observer. Mathematical derivations are presented of this measure for a range of grey level transforms. Also, the logarithmic compression of the echo signals, which is usually performed in echographic equipment, is taken into account. It was found that the intensity display (i.e., a power transform with a power $n=2$) is optimal for detecting a low contrast lesion. When the data are first logarithmically compressed the lesion SNR appeared to increase with increasing power ($1/8 \leq n \leq 8$). In the case of high lesion contrast, the sequence of logarithmic compression followed by a square law transform produced the optimal lesion SNR. This sequence is equivalent to the processing within echographic equipment, where the echo signals are logarithmically compressed, where the TV monitor has a gamma of the order of 2, and when a linear postprocessing curve is used.

Chapter VII presents a retrospective study which was performed to find and test methods that can be used for the differentiation of diffuse liver diseases based on quantitative analysis of ultrasound signals. An on-line data acquisition system was used to obtain radiofrequency echo signals from volunteers and patients. Several methods to estimate the frequency dependent attenuation coefficient were evaluated, whereby a correction for the frequency and depth dependent diffraction and focussing effects caused by the sound beam was applied. Using the estimated value of the attenuation coefficient the rf signals themselves were corrected to remove the depth dependencies caused by the sound beam and by the frequency dependent attenuation. After the correction, the envelope of the rf signals was calculated and the B-mode image was reconstructed. The texture of the B-mode images was analyzed by first and second order statistical methods, including methods to detect regularities in the scattering. The latter characteristic might reveal the structural characteristics of tissue.

The accuracy and precision of the attenuation methods were assessed by using com-

puter simulated rf signals. Phantom measurements were used to test the performance of the methods to correct for the depth dependencies. The echograms of volunteers and patients suffering from various diffuse liver diseases (cirrhosis, hepatitis, Wilson's disease) were recorded and analyzed. We studied the reproducibility of the measurements over a 5 day period and the influence of the biological diurnal rhythm on the evaluated ultrasound paramaters. The mutual correlations between the estimated parameters were used to preselect parameters contributing independent information and which could be used in a discriminant analysis to differentiate between the various diseased conditions.

A summary of the performance of the discrimination between the normal liver group and the various disease groups completes this thesis. For each task an optimal set of parameters was chosen by a stepwise parameter selection technique and the probability of a correct diagnosis was estimated by using the Leaving-One-Out procedure. In this retrospective analysis several disease groups could be differentiated from the normal group with a high precision. This indicates that the methods used in this study may be applicable in clinical routine, although, more independent parameters with good diagnostic ability will be needed to be successful in the differentiation among the various diseases.

Samenvatting

Tijdens de laatste vijftien jaar werd veel energie besteed aan de kwantitatieve analyse van echografische radiofrequente (rf) signalen en echografische beelden. Echter, pas nadat een dieper inzicht werd verworven in de fysische eigenschappen van de geluidsvoortplanting en de interaktie van het geluid met het weefsel, leverden een aantal methoden goede resultaten op. Een belangrijk probleem waar men zich mee bezig hield was de diepte afhankelijkheid van de schatting van de frequentie afhankelijke verzwakkingscoëfficiënt, die veroorzaakt bleek door de diffraktie en fokussering van de geluidsbundel. Er werd een methode ontwikkeld om de spectra die van de echosignalen worden berekend, voor deze invloed te korrigeren. Dit leverde een grote verbetering op van de reproduceerbaarheid van de schatting. Een ander voordeel was dat de resultaten hierdoor voor een groot deel onafhankelijk van de echoapparatuur werden, waardoor resultaten, verkregen door verschillende onderzoekers, vergeleken konden gaan worden.

Dit proefschrift bevat de resultaten van een onderzoek, waarbij gezocht werd naar methoden voor de kwantitatieve analyse van echosignalen ten behoeve van de differentiatie van diffuse ziekten en de detectie van fokale lesies.

In het tweede hoofdstuk werd de invloed van de diffraktie– en fokusseringseffekten op de textuur in B-mode beelden van een homogeen weefsel onderzocht. Dit onderzoek werd uitgevoerd met behulp van realistische computer simulaties en metingen aan een weefselfantoom. De textuur wordt veroorzaakt bij de ontvangst van de echo's door interferentie op het oppervlak van de transducer en wordt "speckle" genoemd. De speckle werd kwantitatief beschreven met behulp van eerste en tweede orde statistische textuuranalyse methoden. Het bleek dat de meeste van de geschatte textuurparameters diepte afhankelijk waren. Dit werd niet alleen veroorzaakt door de bundelinvloed maar ook door de frequentie afhankelijke verzwakking. Om een betrouwbare en reproduceerbare kwantitatieve beschrijving van de textuur te verkrijgen, moeten de rf signalen, die voor de produktie van de B-mode beelden gebruikt worden, gekorrigeerd worden voor deze invloeden. In hoofdstuk VII wordt een frequentie afhankelijke methode voorgesteld en uitgetest om de rf signalen op zodanige manier te korrigeren, dat diepte onafhankelijke schattingen van de textuurparameters verkregen worden. Daarbij werd echter alleen de axiale richting beschouwd.

Een ander onderwerp, dat in hoofdstuk II werd onderzocht, was de vraag of de speckle wel informatie over het weefsel bevat. Hierbij werd gebruik gemaakt van computer gesimuleerde echogrammen van homogeen verstrooiende media, bestaand uit "random" gepositioneerde verstrooiers met variërende dichtheid. Er werd gevonden dat alle onderzochte textuurparameters van deze dichtheid afhangen. Echter, in de limiet van een hoge verstrooierdichtheid ontstaat volledig ontwikkelde speckle, in welk geval slechts de gemiddelde echoamplitude nog afhangt van de dichtheid. Het histogram

van de echoamplitude komt dan overeen met een Rayleigh waarschijnlijkheidsverdeling. Bij een hoge verstrooierdichtheid naderen de onderzochte tweede orde textuurparameters tot limietwaarden, die uitsluitend bepaald worden door de eigenschappen van de transducer.

In echografische apparatuur wordt de omhullende van de rf echosignalen gebruikt voor de produktie van de echobeelden. Daarbij wordt alle fase-informatie weggegooid. In hoofdstukken III tot V werd de bruikbaarheid van de fase van de echosignalen onderzocht. De afgeleide van de fase, ofwel de instantane frequentie, werd gebruikt voor de produktie van een nieuw soort echobeelden. Verschillende methoden werden beschreven voor de stabilisatie van de fase afgeleide (PD). De eigenschappen van de gestabiliseerde PD signalen en de PD beelden, zoals beschreven door eerste en tweede orde statistische textuurparameters, bleken afhankelijk van de stabilisatie methode. Dit onderzoek was gebaseerd op echosignalen verkregen uit computer simulaties, uit experimenten met weefselfantomen en op in-vivo verkregen radiofrequente echogrammen. In hoofdstuk V wordt een theoretische afleiding gepresenteerd van de eerste en tweede orde textuurparameters, waarbij tevens de stabilisatie, en vervolgens de gelijkrichting en het laagdoorlaat filter, gebruikt voor de produktie van de beelden, in rekening worden gebracht. Uit de analyse van de PD beelden van gesimuleerde echosignalen bij variërende verstrooierdichtheden bleek, dat, in het geval van homogene en isotrope verstrooiing, de fase afgeleide geen informatie over de verstrooiingseigenschappen van het weefsel bevat. Het is echter wel mogelijk dat PD afbeeldingen gebruikt kunnen gaan worden om afwijkingen aan het verstrooiingsmodel te detekteren, wanneer biologische weefsels onderzocht gaan worden.

Door de fabrikanten werd in echoapparatuur een aantal postprocessing curven geïmplementeerd waarmee de grijsniveaus van de B-mode beelden gemanipuleerd kunnen worden. In hoofdstuk VI werd ingegaan op de vraag of het mogelijk is om de detektie van fokale lesies te verbeteren door van deze faciliteit gebruik te maken. Als maat voor de detekteerbaarheid van een lesie werd de zogenaamde "lesie signaal ruis verhouding" gehanteerd, waarmee de prestaties van de ideale waarnemer worden beschreven. Wiskundige afleidingen van deze maat werden gepresenteerd voor een reeks van grijsschaal transformaties. Bovendien werd de logarithmische kompressie, die gewoonlijk in echoapparaten wordt toegepast, in rekening gebracht. Het bleek dat de afbeelding van de intensiteit (een machtstransformatie met macht $n = 2$) optimaal was voor de detektie van lesies met een laag kontrast ten opzichte van de omgeving. Wanneer de echosignalen eerst logarithmisch werden gekomprimeerd en daarna aan een machtstransformatie onderworpen, dan nam de lesie signaal ruis verhouding toe als functie van de macht n ($1/8 \leq n \leq 8$). Bij een hoog lesie kontrast leverde de log kompressie gevolgd door een kwadratische transformatie de optimale lesie signaal ruis verhouding op. Dit komt overeen met de verwerking van echosignalen in echoapparatuur, waarbij de echosignalen logarithmisch worden gekomprimeerd, de TV monitor een gamma in de orde van 2 heeft en wanneer een lineaire postprocessing curve wordt gebruikt.

In hoofdstuk VII wordt een retrospektief onderzoek gepresenteerd, dat tot doel had om methoden te vinden en te evalueren, die gebruikt kunnen worden voor de differentiatie van diffuse leverziekten op basis van de kwantitative analyse van ultrageluidssignalen. Een on-line data acquisitie systeem werd gebruikt, waarmee de echosignalen van gezonde vrijwilligers en van patienten werden opgenomen. Er werd een aantal methoden,

waarmee de frequentie afhankelijke verzwakking kan worden geschat, met elkaar verge-
leken. Daarbij werd gekorrigeerd voor de frequentie– en diepte afhankelijke diffraktie-
en fokusseringseffecten veroorzaakt door de geluidsbundel. Met gebruikmaking van de
geschatte verzwakkingscoëfficiënt, werden de rf signalen zelf gekorrigeerd, om de diepte
afhankelijkheden veroorzaakt door de geluidsbundel en de verzwakking te verwijderen.
Na de korrektie werd de omhullende van de echosignalen berekend en werden de B-mode
afbeeldingen gerekonstrueerd. De textuur van deze afbeeldingen werd geanalyseerd met
behulp van eerste en tweede orde statistische textuuranalyse methoden. Tevens wer-
den methoden toegepast om regelmatigheden in de verstrooiing, veroorzaakt door een
regelmatige struktuur, te detekteren.

De nauwkeurigheid van de methoden voor de schatting van de verzwakkingscoëfficiënt
werd bepaald door gebruik te maken van computer gesimuleerde rf echosignalen. Phan-
toom metingen werden gebruikt om de methode, gebruikt voor de korrektie van de
diepte afhankelijkheden, uit te testen.

De echogrammen van vrijwilligers en van patienten leidend aan diverse diffuse lever-
ziekten (cirrhose, hepatitis, ziekte van Wilson) werden geanalyseerd. We onderzochten
de reproduceerbaarheid van de metingen over een periode van 5 dagen en de invloed
van het biologisch dagritme op de gebruikte ultrageluidsparameters. De onderlinge kor-
relaties tussen de geschatte parameters werden geschat om een voorselektie te kunnen
maken van parameters, die onafhankelijke informatie bijdragen en die gebruikt kunnen
gaan worden in een discriminant analyse waarmee de verschillende toestanden van de
lever gedifferentiëerd kunnen worden.

In een appendix bij hoofdstuk VII worden de prestaties gepresenteerd van de pa-
rameters, indien zij gezamenlijk werden gebruikt in een discriminant analyse voor de
differentiatie tussen normale en zieke levers. Voor elke taak werd een optimale set para-
meters geselekteerd met behulp van een "stapsgewijze parameter selektie techniek". De
waarschijnlijkheid van een korrekte diagnose werd bepaald met behulp van de "Leaving-
One-Out methode. In deze retrospectieve analyse konden verscheidene pathologieën met
grote nauwkeurigheid van de gezonde levers worden onderscheiden. Dit duidt erop dat
de methoden, die in dit onderzoek werden gebruikt, toepassing zouden kunnen gaan vin-
den in de klinische routine. Om een nauwkeurige differentiatie tussen de verschillende
pathologieën tot stand te brengen, zullen echter meerdere onafhankelijke parameters
met een goed diagnostisch vermogen nodig zijn.

Curriculum Vitae

Bernard Oosterveld werd geboren op 9 augustus 1955 te Arnhem. Vanaf 1967 volgde hij het middelbaar onderwijs aan het Katholiek Gelders Lyceum in Arnhem, alwaar hij in 1972 het HAVO diploma en in 1974 het Atheneum-B diploma behaalde. Vanaf 1974 studeerde hij Natuurkunde aan de Katholieke Universiteit van Nijmegen, waar hij als bijvakken Biofysica en Statistische Mechanica koos. De afstudeerstage werd onder auspicien van de afdeling Medische Fysica/Biofysica (Prof. Dr. J.J. Eggermont) verricht op het biofysisch laboratorium van de afdeling Oogheelkunde van het Academisch ziekenhuis in Nijmegen. Deze stage had als onderwerp de textuur analyse van echografische beelden en werd begeleid door Dr. Ir. J.M. Thijssen. In deze periode werd tevens de onderwijsbevoegdheid behaald. In november 1984 behaalde hij het doctoraal examen.

Van december 1984 tot augustus 1989 heeft hij als wetenschappelijk assistent het tijdens zijn afstudeerstage gestarte onderzoek voortgezet. Dit werk werd gesubsidieerd door de Stichting voor Technische Wetenschappen (STW), tegenwoordig Nederlandse Organisatie voor Wetenschappelijk Onderzoek (NWO). De resultaten zijn in dit proefschrift beschreven. Sinds 1 januari 1990 is hij werkzaam binnen het project "Front-end for echographic image processing" dat door de EG gesubsidieerd wordt in AIM verband. Daarin is hij betrokken bij de realisering van een (deels) real-time systeem, dat gekoppeld kan worden aan echoapparatuur, voor de toepassing van de methoden en technieken die zinvol bleken in het onderzoek dat hier is beschreven.